Chapter 1
Introduction

1.1 Introduction

This study evaluates the phase diagram of the Al-Pt-Ru ternary system. The study consists of two parts: an experimental part and a computational part.

This chapter gives a background to the development of platinum-based alloys and states the motivation of this work in the light of the current platinum market.

The phase diagrams pertaining to the Al-Pt-Ru system are reviewed in Chapter 2.

Chapters 3 and 4 cover the experimental work. Chapter 3 discusses the experimental methodology used in this study. The experimental results for the Al-Pt-Ru system are discussed, the results reported and a liquidus surface projection is proposed in Chapter 4.

In the computational part, an overview of computational thermodynamics and the principles of the CALPHAD method are presented in Chapter 5. Chapter 6 describes the calculation of the binary phase diagrams with the CALPHAD method, using the Thermo-Calc software, and the extrapolation of the ternary system from the binaries is discussed. A liquidus surface projection is predicted by calculation.

The experimental and calculated phase diagrams are compared in Chapter 7. Conclusions and recommendations are listed.

1.2 Background

Since World War II, Ni-based superalloys (NBSAs) have been developed to become highly successful, operating at high temperatures in the severe environmental conditions in turbine engines, while maintaining their strength. However, NBSAs are approaching the limit of their capabilities, despite advanced processing technologies like single-crystal technology and thermal barrier coatings.

There is a present and future need for a new ultra-high temperature alloy that will still maintain its mechanical properties at least 200 degrees above the maximum operating temperature of the current advanced NBSAs. A number of studies [2000Fai, 2001Hil1] have indicated the potential of platinum-based alloys as the future ultra-high structural alloy since platinum is similar to nickel in crystal structure and chemistry, but has a much higher melting point (2042 K for platinum and 1725 K for nickel) as well as improved corrosion resistance. Platinum forms phases similar to Ni_3Al (the principal strengthening precipitate in superalloys) with a number of elements (e.g. Al, Zr) and initial studies have shown that these alloys have an analogue microstructure of small, semi-coherent

precipitates in a softer matrix, with improved mechanical properties, strength and high-temperature corrosion resistance in comparison to Ni-based superalloys.

Although platinum-based alloys are unlikely to ever replace Ni-based superalloys on account of both higher price and higher density, it is likely that they can be used for the highest application temperature components, in static components in gas turbines and for rockets. Platinum is also extensively used in the protective environmental coatings on Ni-based superalloys, as platinum forms a very stable aluminide with better properties than nickel aluminides, thus shielding the underlying Ni-based superalloy bulk from the high temperatures and corrosive environment.

The development of the Ni-based superalloys spans more than sixty years. In the early years, research and development were based on experimental work alone. However, ways to predict phase diagrams were systematically developed and increasingly assisted alloy development during this period [1998Sau]. There were different ways of thinking, from first principle calculations to neural networks. As computational power became available, the development of these predictions accelerated. One of the successful methods is called the CALPHAD method, an acronym for 'CALculation of PHAse Diagrams', which was developed by Larry Kaufman and a number of co-workers [1970Kau]. This method has lead to the development of databases for many systems, and a number of them are specifically for Ni-based superalloys. The CALPHAD method is based on Gibbs energy functions for elements and phases and predicts equilibrium phase diagrams from thermodynamic principles. One of the major advantages of the CALPHAD method is that experimental work can be limited for a system where a database is available, thus saving time and costs.

A thorough experimental study of Pt-Al-X based alloys (X=Ru, Cr, Ni, Ti, Ta, Re) to identify a base alloy for further development to a potential Pt-based alloy superior to Ni-based alloys, reported that Pt-Al-Ru and Pt-Al-Cr alloys had the best potential properties for high temperature applications [2001Hil1]. Further to that work, the quaternary alloy Pt_{84}:Al_{11}:Ru_2:Cr_3 was identified to be a two phase alloy of fine precipitates in a platinum matrix, with good oxidation resistance and a high hardness [2000Süs]. Thus to facilitate the further development of these Pt-based alloys, a thermodynamic database will be developed, initially covering the Pt-Al-Cr-Ru quaternary system [2002Cor].

In order to understand a multi-component alloy system, one first should understand the binary and ternary phase diagrams that are part of the multi-component system. Not all the binaries in this suggested quaternary Pt-base system are well defined, and for the Pt-based ternaries relevant to the quaternary, no data are available.

In this study, the Al-Pt-Ru ternary alloy system was studied experimentally and the microstructure was characterised over the complete composition ranges. Although the platinum-rich corner is the important area for Pt-based superalloys, all three of the elements play a significant role in the coating technology of Ni-based superalloys since both platinum and ruthenium form stable aluminides. These are still not well characterised in the coating technology, prompting the full ternary to be determined.

1.3 Motivation

The Platinum Development Initiative (PDI) is supporting a drive to investigate new applications for platinum. A Mintek – Department of Science and Technology (DS&T) (previously the Department of Arts, Culture, Science and Technology – DACST) Lead Fund project to identify Pt-base alloy compositions for further investigation lead to a second DS&T Lead Fund project, with the aim to develop a thermodynamic database to facilitate Pt-based alloy design in future. This work is the first contribution to the Pt-database.

As one of the most frequent questions posed when 'platinum-based alloys' are mentioned is 'Cost!!!!', an overview of the platinum market and platinum applications is presented here to give the reader some background and understanding of the market, as well as to place this study in perspective with the bigger platinum picture.

Platinum is an expensive precious metal, and very few people really understand the dynamics of supply and demand in the platinum market. The platinum market is dynamic and vibrant, with some new applications emerging while many other applications decline as substitute materials are found to reduce costs. Furthermore, significant expansion of the South African platinum mining sector might bring changes in the always-complicated balance between supply and demand.

South Africa is the major platinum producer in the world; in 2002 more than 70% of the total world production (5860 million oz = 182.3 tons) was produced, well ahead of Russia which supplies 22% of the total world platinum [2002Joh]. With the current and planned mining expansions in South Africa, a supply of 10 000 million oz are predicted for 2010. In 2000, Pt also took over from gold as the 'forex roost' of South African exports. While gold is continuing a long-term trend of declining production, the platinum industry seems to be forging ahead. It is not expected that supply will balance demand before 2005. The world supply and demand figures for platinum are summarised in Table 1.1.

The PGM applications fall broadly into the following categories:

- Automotive
- Jewellery
- Processing/Production
- Electronics
- Petroleum refining
- Dental/Medical
- Investment

The automotive sector is the largest consumer of platinum, with catalytic converters and the possibility of fuel cells in the near future, immediately coming to mind. Platinum is, with palladium and rhodium, an active element in catalytic converters that convert unburned hydrocarbons into carbon dioxide and water vapour in fossil fuelled automotives. The amount of palladium in the catalytic converters was increased a few

years ago, but it is inevitable that the platinum and rhodium content will have to be raised again to meet the ever-increasing stricter emission control requirements. Diesel powered automotives, a market which increased sharply over the last few years, can use only platinum as a catalyst. On the other side of the coin, automakers are aggressively researching ways to eliminate the expensive platinum group metals (PGM) based emission control components, especially with new 'lean-burn' technologies that will reduce or even eliminate the need for PGM catalytic converters.

Table 1.1. Platinum demand and supply [2002Joh]

Platinum supply and demand										
'000 oz	**1992**	**1993**	**1994**	**1995**	**1996**	**1997**	**1998**	**1999**	**2000**	**2001**
Supply										
South Africa	2,750	3,360	3,160	3,370	3,390	3,700	3,680	3,900	3,800	4,100
Russia	750	680	1,010	1,280	1,220	900	1,300	540	1,100	1,300
North America	200	220	220	240	240	240	285	270	285	350
Others	120	130	140	100	130	120	135	160	105	110
Total Supply	**3,820**	**4,390**	**4,530**	**4,990**	**4,980**	**4,960**	**5,400**	**4,870**	**5,290**	**5,860**
Demand by application										
Auto catalyst: Gross	1,550	1,685	1,870	1,850	1,880	1,830	1,800	1,610	1,890	2,520
Recovery	-230	-255	-290	320	-350	-370	-405	-420	-470	-520
Chemical	215	180	190	215	230	235	280	320	295	290
Electrical	165	165	185	240	275	305	300	370	455	385
Glass	80	80	160	225	255	265	220	200	255	285
Investment: small	145	125	155	75	110	180	210	90	-100	30
Large	110	180	240	270	130	60	**105**	90	-100	30
Jewellery	1,510	1,615	1,740	1,810	1,990	2,160	2,430	2,880	2,830	2,550
Petroleum	120	105	90	120	185	170	125	115	110	125
Other	150	165	190	225	255	295	305	335	375	435
	3,815	4,045	4,530	4,710	4,960	5,130	5,370	5,590	5,680	6,150
Western sales to China*	0	20	50	130						
Total demand	**3,815**	**4,065**	**4,580**	**4,840**	**4,960**	**5,130**	**5,370**	**5,590**	**5,680**	**6,150**
Movements in stocks	5	325	-50	150	20	-170	30	-720	-390	-290
	3,820	4,390	4,530	4,990	4,980	4,960	5,400	4,870	5,290	5,860
Demand by region										
Europe	860	895	935	880	840	875	910	995	1,150	1,490
Japan	1,870	1,975	2,145	2,215	2,005	1,885	1,795	1,820	1,410	1,250
North America	705	760	940	1,015	1,180	1,250	1,325	1,080	1,225	1,285
Rest of the world	380	415	510	600	935	1,120	1,340	1,695	1,895	2,125
	3,815	**4,045**	**4,530**	**4,710**	**4,960**	**5,130**	**5,370**	**5,590**	**5,680**	**6,150**
Western sales to China *	0	20	50	130						
Total demand	3,815	4,065	4,580	4,840	4,960	5,130	5,370	5,590	5,660	6,150
**Before 1993, estimates include Eastern Europe; for 1993 and subsequent years, demand in this region is included in the European figures. From 1996, demand in China is incorporated in our Rest of the World estimates*										

The use of fuel cell technology to replace fossil fuel in the automotive industry is a strong likelihood, as international emission and fuel-efficiency mandates are becoming more challenging. Prototypes of this new generation of automobiles have been released by some of the major automotive manufacturers. Catalysts are the only way to increase the efficiency of proton exchange membrane fuel cells (PEMFC), the most suitable fuel cell for automotive applications. While platinum was initially the main catalyst in PEMFC technology, which could have resulted in a complete world shortage of platinum, recent developments have shrunk the amount of platinum from 26 mg/cm^2 to only 0.2 mg/cm^2 [2001Wil] as Pt is replaced by a Pt-FeO_x compound.

Other automotive applications include PGMs used in oxygen and ozone sensors for anti-pollution subsystems. Both platinum and ruthenium are also used in life-long spark plugs.

The demand for platinum jewellery increased sharply in the mid-nineties mainly due to consumers in the eastern markets switching from gold to platinum. However, since 2000 there has been a 13% decline in this demand, as the Japanese economy is in recession. On the other hand, China is still a growing market for platinum jewellery as gold trade is strictly controlled in China. This is a market driven by Asian and other ethnic groups feeling that platinum has a more pleasing contrast with their skin colour than other metals. Jewellery is an extremely fickle market, and specifically in platinum based jewellery, the market share is directly proportional to the marketing effort, whereas gold and diamond sales are not related to marketing input.

It is estimated that platinum is used as a catalyst in about 20 % of products purchased by modern consumers. Platinum is a catalytic agent in the processing of nitric acid, fertilizers, synthetic fibres and a number of other materials. Although platinum is essential in these processes and there are few satisfactory substitutes, it is not consumed in the process and can be recycled for future use.

The glass industry uses platinum dies extensively. Platinum is also used in fibreglass production. While the initial amount of platinum needed for bushings and claddings is high, these components only need a ~1% refurbishing per year.

Various kinds of PGM alloy combinations are used in thermocouple devices to measure temperature with high accuracies, while a platinum silicide is used in thin film optical and temperature sensing systems. Platinum is used in the semi-conductor industry for wire and electrical contacts in corrosive or high-voltage environments, as well as for magnetic coatings for high-density hard disk drives and optical storage systems. Hewlett Packard recently announced a new memory storage device, based on rotaxane molecules, where they plant these molecules between tiny platinum and titanium layers. This could revolutionise memory storage as it has at least 10 times the memory density of the best DRAM (silicon based memory). HP will partly disclose their results to 'seed their own competition', thus the use of platinum in the semiconductor industry can increase significantly over the next few years [2002Eco].

Platinum and palladium catalysis is an environmentally-friendly way to perform crude oil separation. While a significant amount of platinum is needed for the fine meshed nets used in this industry, the platinum is not consumed by the separation process and only needs a refurbishment after the initial capital outlay to procure the nets.

Investment demand for platinum is unpredictable. Investment is usually related to the platinum price. When the price falls, the interest in platinum investment products is high. During the first six months of 2001, demand for the US Mint's platinum Eagle series of proof and bullion coins fell as the platinum price hovered around $600 per oz and only increased as the platinum price began to fall.

Platinum use in medicine is a growing market. In the USA, the annual revenue from platinum used in medicine was $1billion, and the market is growing at ~15% per year. Most of these drugs are used in the treatment of cancer. Due to the complexity in identifying an active unit, these drugs will remain a platinum domain as all research on substituting the platinum in the active unit has failed to date.

Other application demands increased steadily from 4% in 1992 to 7% in 2001. One of the growing applications in this field is the use of Pt in environmentally protective coatings especially on the Ni-based superalloys to enhance their properties, as Pt additions to the aluminide coatings significantly increase the oxide scale adherence at high temperatures [2000Hay].

The platinum supply is further boosted by an 11% increase in 2001 in the platinum recovered from autocatalysts. This figure is likely to keep on increasing in the future as a new smelter plant in South Africa is planned, dedicated to the recovery of platinum, and in Europe legislation will require that at least 85 % of a car's weight is recycled.

It is thus clear that, as the South African platinum industries are increasing their mining operations and world research is focused on reducing platinum to reduce cost, efforts must be maintained to search for future applications for platinum to avoid an over-supply on the market. It is, therefore, to the advantage of the South African platinum market that studies such as this are conducted, as they might open up other opportunities for platinum demand along the way.

So what is the future of platinum in high temperature applications? As previously mentioned, platinum already plays an important role in environmentally protective coatings on Ni-based superalloys. The extreme high-temperature components in a turbine (e.g. blades, vanes and airfoils) are typically coated with a 2-10 μm thick layer of platinum by electrolysis or PVD. An aluminide coating is then grown by a diffusion treatment as platinum promotes the formation of a slow growth, very adherent and stable Al_2O_3 layer on the surface. With roughly 600-700 new commercial aircraft per year, a current fleet of about 12 000 commercial aircraft and 12 000 business aircraft, at 2-4 engines per aircraft, it amounts to about 60 000 engines. Blades are recoated every 10 000 - 150 000 hours. The current military fleet is estimated to about 15 000 aircraft, with 5 000 new aircraft planned for the next 10 years. At 2-3 engines per aircraft, another at

least 32 000 engines, which have shorter lifespans due to the higher demands placed on them. At roughly 50g of platinum per aircraft engine, the aerospace industry uses at least 4500 kg platinum per year. It is nearly impossible to account for industrial gas turbines on land. These typically have a $15m^2$ blade surface area per turbine and it has been estimated that the land turbine industry could use 10 000 kg of platinum per year [2001Hil1].

Looking at a platinum-based superalloy, and not a Ni-based superalloy coated with a few microns of platinum, the picture is different. No detailed study has yet been done on the feasibility of such an option, but platinum-based superalloys are not an impossibility. There will be advantages of a higher operating temperature, which will increase the efficiency of the turbines dramatically and reduce the thrust fuel cost. However, platinum is very dense (21.5 g/cm^3 against ~8 g/cm^3 for NBSAs) and the cost of platinum as base material will significantly change the cost-breakdown for turbine engines. The raw material cost is currently 2% of the total turbine cost for NBSAs, while nearly 45% of the cost is due to the highly specialised casting, machining and coating costs, as well as another 25% for quality management, which is critical as the coatings must be fail-proof. Platinum-based turbine blades might not need these specialized coating technologies. The use of platinum based alloys as high temperature alloys in turbines will be limited to only the components exposed to the highest temperatures: first stage blades and vanes, combustors, transitions and shrouds.

This might just be what South African platinum production needs to increase the demand and justify the current expansions to increase the platinum supply, especially since there are platinum reserves for the next 500 years. It is thus important that opportunities for new applications for platinum are explored and investigated beyond the present limits, to ensure the future of this white metal as South Africa's main foreign currency commodity.

Chapter 2
Literature review - The Phase Diagrams

The Al-Pt-Ru ternary phase diagram is virtually unstudied, as only one partial isothermal section at 1350°C for the high-platinum corner has been reported [2001Big1,2001Big2, 2001Hil1].

In order to evaluate a ternary system accurately and completely, the binary systems making up the ternary diagram must be well defined, as they are the 'building blocks' of the system. Discrepancies must be addressed and assumptions well identified. As both the Al-Pt and Al-Ru phase diagrams published in the Binary Alloy Phase Diagrams series of Massalski *et al.* [1990Mas] show some discrepancies with later results published in the literature, this chapter gives a detailed overview of the phases found in the Al-Pt, Al-Ru and Pt-Ru binary phase diagrams and the data used in this determination of the Al-Pt-Ru phase diagram.

2.1 The Elements: Al, Pt and Ru

Aluminium is a soft, lightweight silvery-white metal, the third most abundant metal in the earth's crust, mostly occurring in the form of Al_2O_3. Too soft in its pure form, it is alloyed with other metals to harden and strengthen it. Aluminium alloys are used for many purposes from airplanes to beverage cans. Bonded to the transition metals, highly ordered aluminides, such as MAl, MAl_3 and M_3Al (M=Ni, Fe, Ti, etc), can form. These intermetallic phases possess many remarkable properties. Their high temperature strength is often very attractive (some aluminide intermetallic phases get stronger as the temperature increases over certain temperature ranges), and they frequently exhibit very good resistance to high temperature corrosion, due to the formation of stable Al_2O_3 rich oxide films. However, an inherent brittleness at room temperature has hampered their fabrication to date.

Platinum and ruthenium belong to the so-called platinum group metals (PGMs), the six metal group of platinum, palladium, rhodium, iridium, ruthenium and osmium. Platinum is soft, ductile, and resistant to oxidation and high temperature corrosion. Platinum is one of the densest known metals. Ruthenium is hard, brittle, shows poor oxidation resistance at high temperatures and is almost unworkable in the metallic state. Alloys of the PGMs are used for their exceptional catalytic properties. Other distinctive properties include resistance to chemical attack, excellent high-temperature characteristics, and stable electrical properties. The properties of Al, Pt and Ru are given in Table 2.1.

Table 2.1. Properties of the pure elements [1985Vil, 2001ICDD].

	Aluminium	**Platinum**	**Ruthenium**
Chemical symbol	Al	Pt	Ru
Crystal structure	fcc-Al	fcc-A1	hcp-A3
Space Group	Fm-3m	Fm-3m	$P6_3/mmc$
Lattice parameter [nm]	0.40496	0.39239	0.27057
Melting point [K]	933.5	2 042	2 583
Density [g/cm^3]	2.698	21.45	12.45

2.2 The Al-Pt Binary System

2.2.1 Phase Diagram Data

The Al-Pt phase diagram is complex, with nine intermetallic phases present in the equilibrium diagram, of which two phases have transformations to polymorphic phases at lower temperatures. The diagram is shown in Figure 2.1 and the stable intermetallic phases are listed in Table 2.2. Six metastable phases have been reported (Table 2.3).

While certain features in the system had been determined reliably, other aspects of this diagram, especially at the Pt-rich end, remain problematic. McAlister and Kahan reviewed the Pt-Al system in 1986 for the Bulletin of Alloy Phase Diagrams [1986McA]. The transformation temperatures for the formation of the low temperature polymorphs of the Pt_3Al and Pt_2Al phases are uncertain, and the presence of the β phase had not been confirmed. Oya, Mishima and Suzuki [1987Oya] proposed a revised phase diagram for the platinum rich area (Figure 2.2).

Huch and Klemm [1964Huc] reported platinum to be practically insoluble in (Al). They reported an eutectic reaction L → (Al) + Pt_5Al_{21} at 700 K. Extrapolation of this reaction by McAlister [1986McA] places the eutectic composition at 0.44 at. % Pt, which is in agreement with experimental unidirectional solidification work by Piatti and Pellegrini [1980Pia].

Pt_5Al_{21} forms by a peritectic reaction L + Pt_8Al_{21} → Pt_5Al_{21} at 1079 K. Pt_5Al_{21} is a complex cubic stoichiometric phase. Huch and Klemm [1964Huc] reported a cubic '$PtAl_4$' with ~20 at. % Pt. They suggested the phase might rather be of the form Pt_5Al_{21}. Guex [1976Gue] also reported a complex cubic phase of either $PtAl_4$ or Pt_5Al_{21}structure.

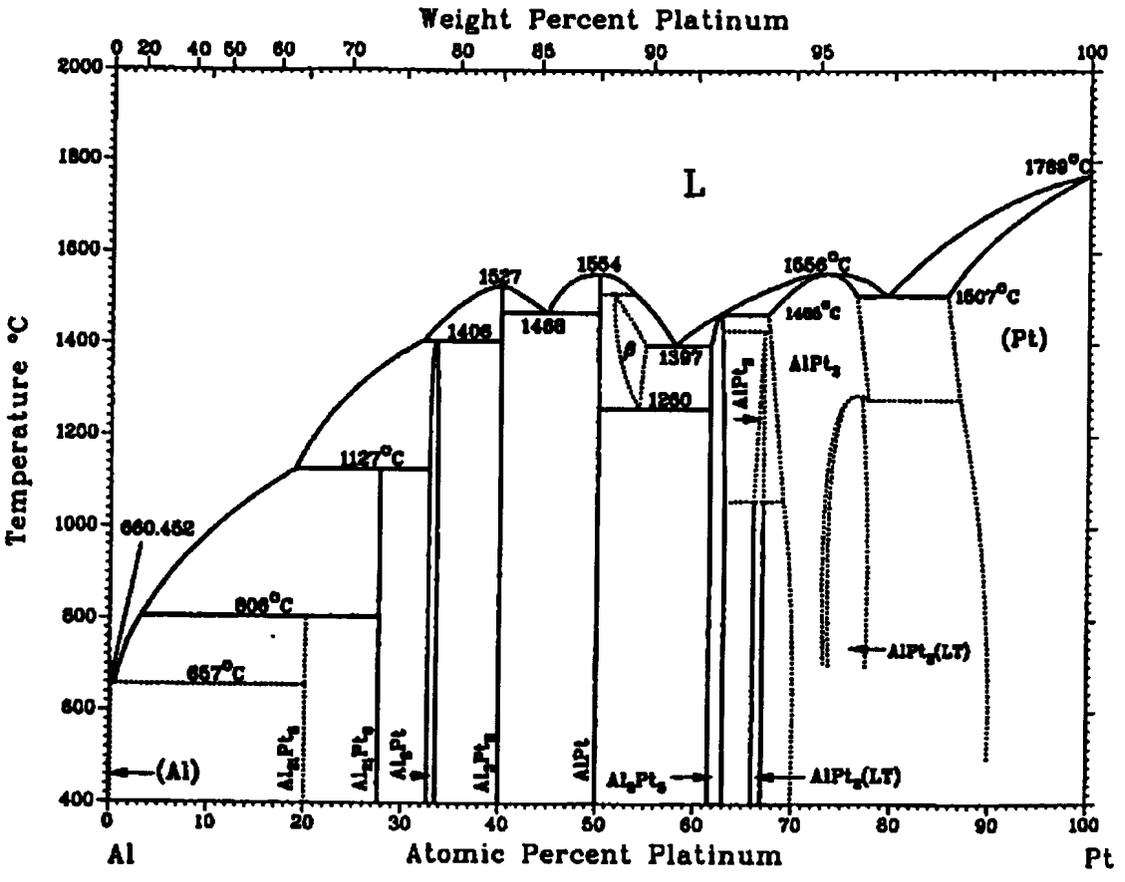

Figure 2.1. The Al-Pt phase diagram from Massalski [1990Mas].

Schaller [1979Sch] reported, without experimental detail, a hexagonal Pt_5Al_{21} phase while Ellner, Kattner and Predel [1982Ell] confirmed the hexagonal structure of the phase and suggested it to be a $PtAl_4$ phase. Piatti and Pellegrini [1980Pia] also reported a hexagonal phase in this composition range, which they suggested to be Pt_6Al_{21}, but also noted a transformation from hexagonal to cubic phases after treatment at 473 K for several hours. Careful analysis of thermal arrest data reported by Huch and Klemm [1964Huc] confirmed the phase as Pt_5Al_{21} [1986McA]. $PtAl_4$ has thus been suggested as a metastable phase in the Pt-Al system. A crystal structure of Pt_5Al_{21} has not been published.

The stoichiometric Pt_8Al_{21} phase at 27.5 at. % Pt has been confirmed by Edshammer [1965Eds] and Ellner *et al.* [1982Ell] after earlier reports of a $PtAl_3$-like phase by Huch [1964Huc] and Guex [1976Gue]. Pt_8Al_{21} forms by the peritectic reaction L+ $PtAl_2$ → Pt_8Al_{21} at 1400 K.

Huch and Klemm [1964Huc], Guex [1976] and Ellner *et al.* [1982Ell] reported the $PtAl_2$ phase which forms through a peritectic reaction L + Pt_2Al_3 → $PtAl_2$ at 1952 K. The $PtAl_2$ phase is of the cubic CaF_2 type. It has been reported as a stoichiometric compound by Guex [1976Gue], while the other workers reported a ~1 at. % phase range up to 1123 K.

Table 2.2. Crystal structure data for the stable phases in the Al-Pt binary system.

Phase	Composition range (at. %Pt)		Pearson symbol	Space Group	Struktur-bericht	Prototype	Reference
(Al)	0		*cF*4	Fm3m	A1	Cu	
Pt_5Al_{21}	19.2		*c***				[1964Huc] [1980Pia]
Pt_8Al_{21}	27		*tI*116	$I4_{1\alpha}$			[1968Eds] [1982Ell]
$PtAl_2$	31.5	33.5	*cF*12	Fm3m	C1	CaF_2	[1937Zin] [1963Fer] [1982Ell]
Pt_2Al_3	40		*hP*5	P3m1			[1978Bah]
PtAl	50		*cP*8	$P2_13$	B20	FeSi	[1957Sch] [1963Fer]
β	52	56	*cP*2	Pm3m	B2	CsCl	[1975Cha1] [1978Bha]
Pt_5Al_3	61.5	63	*oP*16	Pbam		Ge_3Rh_5	[1964Huc]
Pt_2Al	66	67	*oP*12	Pnma	C23	$PbCl_2$	[1975Cha1]
Pt_2Al (LT)	66	67	*oP*24	Pmma		$GaPt_2$ (LT)	[1976Cha]
Pt_3Al	67.3	77.7	*cP*4	Pm3m	$L1_2$	$AuCu_3$	[1962Bro] [1964Huc] [1963Mag]
Pt_3Al (LT)	73.5	100	*tP*16	P4/mbm	DO_c'	$GaPt_3$ (LT)	[1975Cha1]
(Pt)	83.8	100	*cF*4	Fm3m	A1	Cu	

(LT – Low Temperature, HT – High Temperature)

Table 2.3 Crystal structure data for the metastable phases in the Al-Pt binary system.

Phase	Composition (at. % Pt)	Pearson symbol	Space Group	Struktur-bericht	Prototype	Reference
α'		*cF*4	Fm3m	A1	Cu	[1964Com]
$PtAl_4$	20	*hP**				[1978Sch] [1980Pia] [1982Ell]
$PtAl_5$		*P4*				[2001Lab]
$PtAl_6$	14	*o***				[1975Ton] [1979Cha]
ε'		*c***				[1979Cha]
λ'	10-25					[1982Ell]

Pt_2Al_3 forms congruently L ↔ Pt_2Al_3 at 1800 K and 40 at. % Pt. Huch and Klemm [1964Huc], Guex [1976Gue] and Ellner *et al.* [1982Ell] reported that Pt_2Al_3 has a structure related to, but not isotypic with, hexagonal Ni_2Al_3 and essentially has no solubility range.

PtAl is a stoichiometric intermetallic phase and has a cubic FeSi structure. It forms congruently from the liquid at 1827 K and 50 at. % Pt by the reaction L ↔ PtAl.

Experimental evidence of a β-phase existing between 1533 - 1733 K, with a composition range from 51 - 56 at. % Pt, has been reported by Chattopadhyay and Schubert [1975Cha1], as well as by Bhan and Kudielka [1978Bha]. McAlister and Kahan [1986McA] included these observations in their assessment of the Pt-Al system and proposed a peritectic reaction PtAl + L → β. No temperature was reported for this reaction. The eutectoid decomposition β ↔ PtAl + Pt_5Al_3 has also been proposed by McAlister and Kahan [1986McA] to correspond with a thermal arrest reported by Huch and Klemm [1964Huc].

A Pt_3Al_2 phase was reported by Huch and Klemm [1964Huc] after observing a thermal arrest at 1533 K between 50 to 60 at. % Pt. Guex [1976Gue] also reported this phase, but it was referenced to the work of Huch and Klemm [1964Huc] and not an experimental observation. Subsequent studies have failed to confirm the existence of this phase and it has been suggested by McAlister and Kahan [1986McA] that Huch and Klemm most likely misinterpreted the solubility range of Pt_5Al_3, and that what they observed was the eutectoid decomposition of the β phase.

Pt_5Al_3 is rhombohedral of the Rh_5Ge_3 type and forms by peritectically L + $PtAl_3$ → Pt_5Al_3 at 1738 K. McAlister's version of the phase diagram [1986McA] shows Pt_5Al_3 having a solubility range 61.5 to 63 at. % Pt, as reported by Ellner *et al.* [1982Ell] and Oya *et al.* [1987Oya].

A peritectoid reaction $PtAl_3$ + Pt_5Al_3 → Pt_2Al occurs at about 1703 K and 67.5 at. % Pt, forming Pt_2Al with a phase range of ~ 2 at. %. Two crystal variants of the Pt_2Al phase have been reported, a high temperature (HT) form similar to the $PbCl_2$ type and a low temperature (LT) form relating to the $GaPt_2$ (LT) type. While the nature of the reaction is still unknown, it is accepted that the reaction occurs at ~ 1333 K [1986McA,1987Oya]. Biggs [2001Big2] suggested a martensitic-type reaction.

The highest Pt-containing intermetallic phase is Pt_3Al. Pt_3Al forms congruently L → Pt_3Al at 1829 K at 73.2 at. % Pt. A phase width of ~ 4-6 at. % has been reported for Pt_3Al. A martensitic type transformation has been reported where the cubic $L1_2$ structure of Pt_3Al, transforms to a tetragonal DO'_c Pt_3Al during cooling. There are many discrepancies, and to further complicate matters, the temperature of the transformation is composition dependent. It has been reported as either a congruent transformation at 1563 K or an eutectic reaction at 1553 K, depending on the composition. Oya *et al.* [1987Oya] reported an intermediate phase between the HT and LT Pt_3Al phases (Figure 2.2). The intermediate phase forms at ~ 613 K and the low temperature phase at ~ 400 K. The DO_c

phase was reported to be extremely unstable. Biggs [2001Big2] reported the $L1_2$ to DO'_c transformation at between 623 to 673 K.

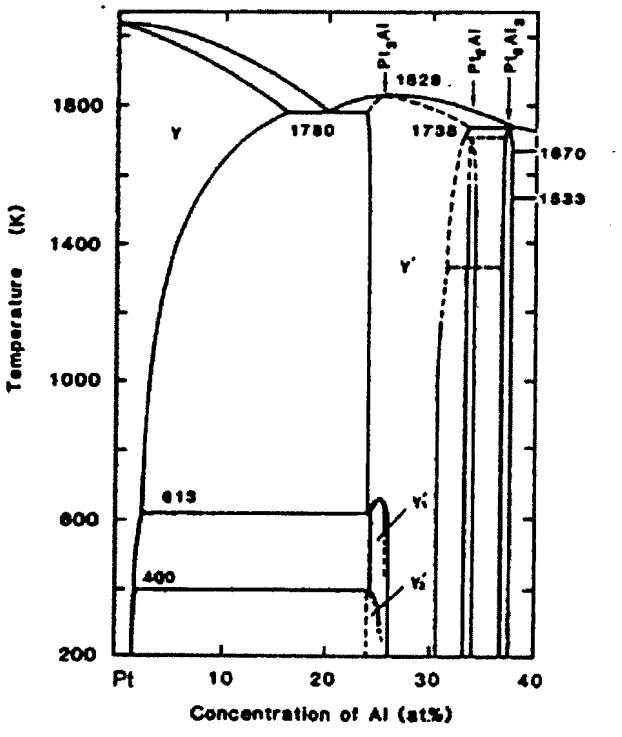

Figure 2.2. Revised Pt-rich portion of the Al-Pt phase diagram [1987Oya].

An eutectic reaction $L \rightarrow (Pt) + Pt_3Al$, reported by Huch and Klemm [1964Huc] and confirmed by Darling. Selman and Rushforth [1970Dar], occurs at 1780 K and 79.5 at. % Pt.

From the combined data of Huch and Klemm [1964Huc] and Darling *et al.* [1970Dar], (Pt) dissolves about 14 at.% Al at 1783 K. Darling *et al.* [1970Dar] suggested a lower solubility of Al in (Pt) at lower temperatures, confirmed as 10 at. % Pt at 1473 K by Bronger and Klemm [1962Bro] and 10 and 5 at. % Pt at 1273 K and 573 K respectively by Schaller [1979Sch].

Wu and Jin [2000Wu] calculated the Al-Pt phase diagram with the CALPHAD technique (Figure 2.3). The calculation did not include the β and the Pt_2Al phases. The Pt_3Al phase was not described as an ordered phase and the order/disorder transformation had not been included. The low temperature Pt_3Al phases have not been included either. Both $PtAl_2$ and Pt_5Al_3 have been modelled as stoichiometric compounds, making no provision for the composition ranges reported above.

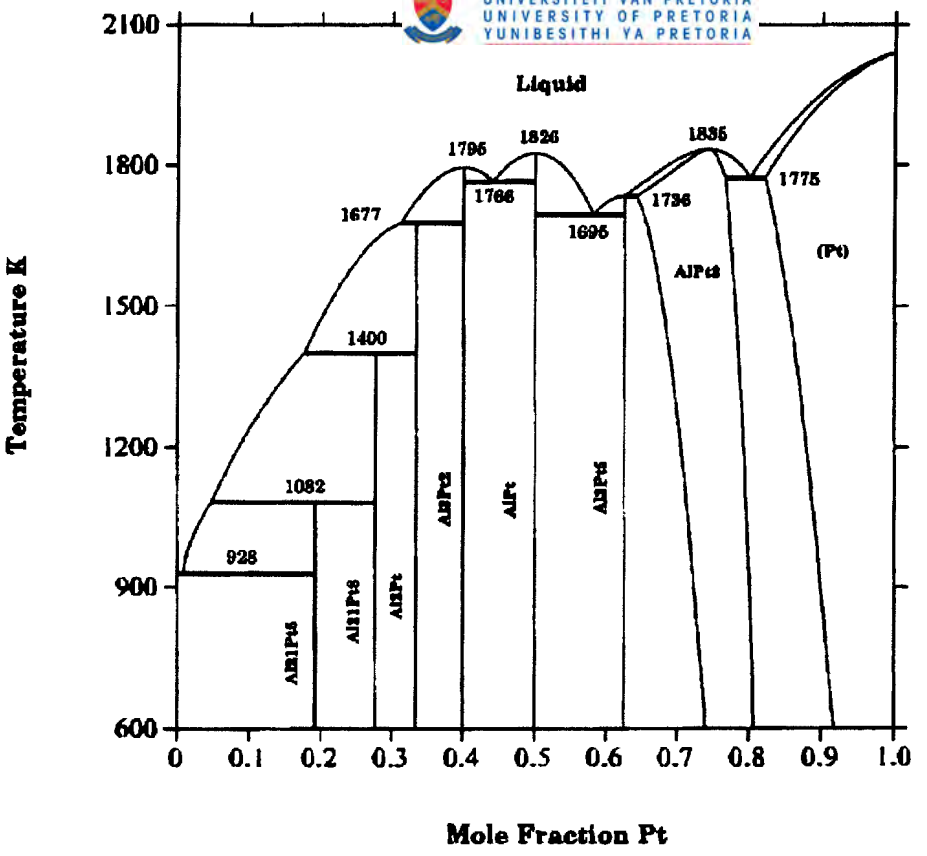

Figure 2.3. The calculated Al-Pt phase diagram by Wu and Jin [2000Wu].

2.2.2 Thermodynamic data

Ferro *et al.* [1968Fer] determined the heat of formation (ΔH_f) for alloys in the Al-Pt system experimentally by solute solvent drop calorimetry. Worrel and Ramanarayanan [1981Wor] determined the Gibbs energy of mixing (ΔG_m) for the 75 at. % Pt composition by an electrochemical cell technique. Lee and Sommer [1985Lee] determined the partial enthalpies of mixing (ΔH_m) of liquid aluminium-rich Pt alloys at ~1200 K using solution calorimetry. Jung and Kleppa [1991Jun] determined the enthalpy of formation for PtAl by direct synthesis calorimetry at 1473 ± 2 K. Meschel and Kleppa [1993Mes] determined the enthalpies of formation for Pt_2Al_3 and Pt_3Al in the same way.

Miedema's semi-empirical model has been used to estimate enthalpies of formation for some of the phases [1988deB].

Ab initio techniques have also been applied to predict the enthalpies of formation. Ngoepe [2002Ngo] used a pseudo-potential total energy package (CASTEP) approach to calculate heats of formation for PtAl and Pt_3Al.

The thermodynamic data for the Al-Pt system are listed in Table 2.4.

Table 2.4.Enthalpies of formation for the stable phases in the Al-Pt system.

Phase	ΔH_f [kJ/mole atoms]	Method	Reference
Pt_5Al_{21}	-57.320	Solute solvent drop calorimetry	[1968Fer]
Pt_8Al_{21}	-71.130	Solute solvent drop calorimetry	[1968Fer]
$PtAl_2$	-100.420	Solute solvent drop calorimetry	[1968Fer]
Pt_2Al_3	-94.980 -79.000 -96.500	Solute solvent drop calorimetry Miedema semi-empirical method Direct Synthesis Calorimetry	[1968Fer] [1988deB] [1993Mes]
PtAl	-100.420 -100.000 -82.000 -67.440	Solute solvent drop calorimetry Direct Synthesis Calorimetry Miedema semi-empirical method *Ab initio*	[1968Fer] [1991Jun] [1988deB] [2002Ngo]
β			
Pt_5Al_3	-90.730	Miedema semi-empirical method	[1998Wol]
Pt_2Al	-88.280	Miedema semi-empirical method	[1998Wol]
Pt_2Al (LT)			
Pt_3Al	-69.870 -63.600 -50.990 -76.000* -74.380	Solution Calorimetry Direct Synthesis Calorimetry Miedema semi-empirical method Electrochemical *Ab initio*	[1968Fer] [1993Mes] [1988deB] [1981Wor] [2002Ngo]
Pt_3Al (LT)**	-79.100	*Ab initio*	[2002Ngo]

* Gibbs energy of mixing: -76 460 + 7.48*T [1981Wor], which gives an estimated enthalpy of formation of −76 000 J/mol of atoms

** DO_c structure

2.3 The Al-Ru Binary System

2.3.1 Phase Diagram Data

The Al-Ru phase diagram from the Binary Alloy Phase Diagrams series [1990Mas] includes five stable intermetallic phases as shown in Figure 2.4. However, the phase boundaries are in dashed lines, indicating that uncertainties are associated with the phases and their homogeneity ranges. Most of the invariant reaction temperatures are also not well determined. Subsequent work by Anlage [1988Anl] and Boniface and Cornish [1996Bon1, 1996Bon2] clarified some of these uncertainties. Boniface and Cornish [1996Bon2] proposed a revised phase diagram, incorporating the results from Anlage [1988Anl] (Figure 2.5). Okamoto [1997Oka] reviewed the Al-Ru system and reported the diagram proposed by Boniface and Cornish to be the more acceptable phase diagram. However, the liquidus surface on the cascade of peritectic reactions did not obey all phase diagram rules and a modification was suggested by Prins and Cornish [2000Pri].

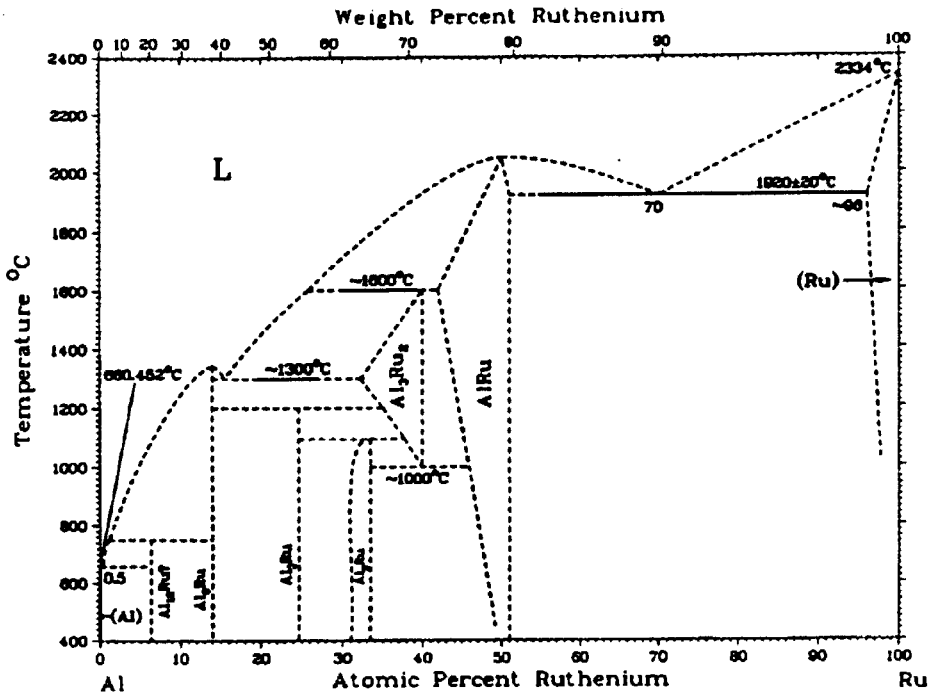

Figure 2.4 The Al-Ru phase diagram after Massalski [1990Mas].

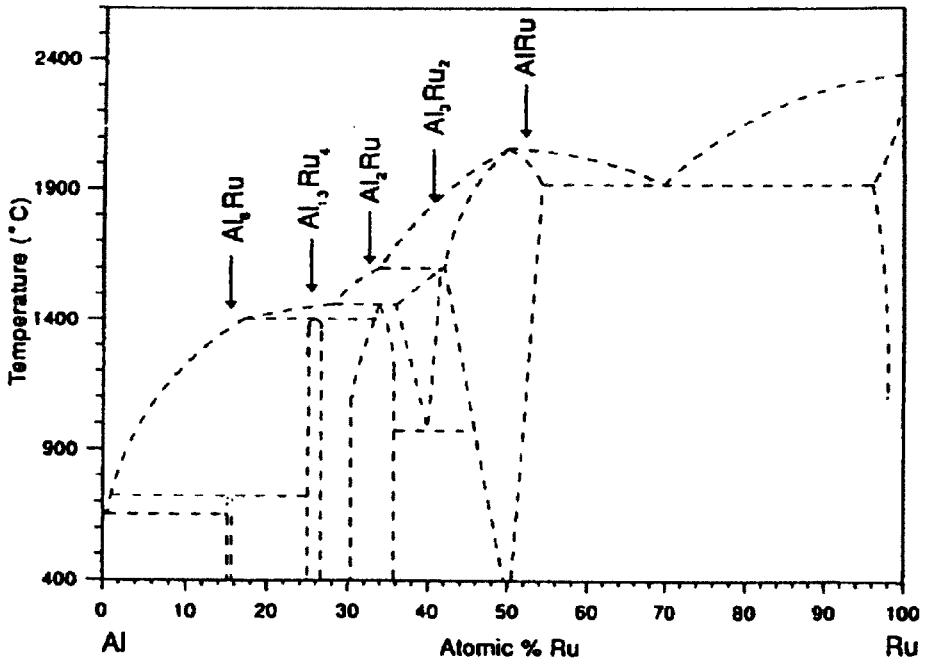

Figure 2.5. The modified Al-Ru phase diagram after Boniface and Cornish [1996Bon2].

The peritectic formation temperatures of the $RuAl_2$ and Ru_2Al_3 phases were raised to 1873K and 1973 K respectively, to agree with reaction temperatures reported by Obrowski [1860Obr]. The crystal structure data for the stable intermetallic phases are listed in Table 2.5. Only one metastable phase, $RuAl_{\sim 2.5}$, has been reported for the Al-Ru system [1968Eds].

Obrowski [1960Obr] reported the first phase diagram for the Al-Ru system and this was based on microscopic, X-ray and thermoanalytical observations. Six intermetallic phases were reported: $RuAl_{12}$ (although some uncertainty existed of the exact composition), $RuAl_6$, $RuAl_3$, $RuAl_2$, Ru_2Al_3 and RuAl, taking part in eight invariant reactions. The Ru-rich solid solution was reported to comprise ~ 4 at. % Al at the eutectic temperature. No solubility of Ru in (Al) was detected and it was also concluded that all the Al-rich intermetallic compounds were stoichiometric line compounds. The RuAl phase was observed to melt at 2333 ± 20 K and the eutectic reaction between RuAl + (Ru) at 2193 ± 20 K. Reactions were observed at 1573 and 1873 K and these were assigned to eutectic and peritectic r eactions respectively. However, it was concluded that some uncertainty existed of the solid-state reactions between 20 and 40 at. % Ru. Apart from Obrowski, no subsequent workers have reported the existence of $RuAl_{12}$. Other reactions reported by Obrowski, but not found by other workers are:

$L \rightarrow RuAl_6$

$L \rightarrow RuAl_6 + Ru_2Al_3$

$RuAl_6 + Ru_2Al_3 \rightarrow RuAl_3$

$RuAl_3 + Ru_2Al_3 \rightarrow RuAl_2$.

Table 2.5. The compositions and crystal data for the elements and compounds in the Al-Ru system.

Phase	Composition (at. % Ru)		Pearson symbol	Space Group	Struktur-bericht	Prototype	Reference
Al			*cF*4	*Fm*3-*m*	A1	Cu	
$RuAl_6$	14.3	14.3	*oC*28				[1968Eds]
						$MnAl_6$	[1982Cha]
	15.1±1	15.7±1					[1996Bon2]
Ru_4Al_{13}			*mC*102	C2/*m*		Fe_4Al_{13}	[1965Eds]
	23.6	23.6					[1988Anl]
	25.0±1.5	26.6±1.5					[1996Bon2]
$RuAl_2$	30.35	33	*tI*6	I4/*mmm*	$C11_\alpha$	CaC_2	[1960Obr]
			*oF*24	*Fddd*	C54	$TiSi_2$	[1966Eds]
	30.4±1	35.8±1					[1996Bon2]
Ru_2Al_3			*hP*5	P3-*m*1	$D5_{13}$	Ni_2Al_3	[1960Obr]
			*tI*10	I4/*mmm*		Os_2Al_3	[1966Eds]
RuAl			*cP*2	*Pm*3-*m*	B2	CsCl	[1960Obr]
Ru			*hP*2	*Fm*3-*m*	A3	Mg	

Schwomma [1963Sch] undertook X-ray work on a 33.3 at. % Ru sample, and found $RuAl_2$ and RuAl. Uncertainty through the contamination of the samples by silicon and oxygen was, however, raised as a possible problem by the author.

Edshammar determined the crystal structure for Ru_4Al_{13} [1965Eds] (Obrowski's $RuAl_3$ [1960Obr]), and noted the similarity with Fe_4Al_{13} because of the twinned prismatic structure and co-ordination numbers, although Ru_4Al_{13} showed even better agreement with Os_4Al_{13}. It was also found that Al atoms were absent from some of the sites which were partially occupied by Al in Fe_4Al_{13} and Co_4Al_{13}. Ru_4Al_{13} was, therefore, considered to be the ideal structure of $RuAl_3$ [1960Obr]. Subsequently with X-ray powder methods, Edshammer reported the crystal structures for five more intermetallic phases: RuAl, Ru_2Al_3, $RuAl_2$, $RuAl_{\sim 2.5}$ and $RuAl_6$ [1966Eds, 1968Eds]. The phase $RuAl_{\sim 2.5}$ was observed only in arc-melted samples. There were some additional CsCl-like phases reported around the composition RuAl, but no further details were given. No evidence of the $RuAl_{12}$ phase was found, and there were other inconsistencies with Obrowski's phase diagram [1960Obr] concerning the Ru_2Al_3 and $RuAl_2$ phases.

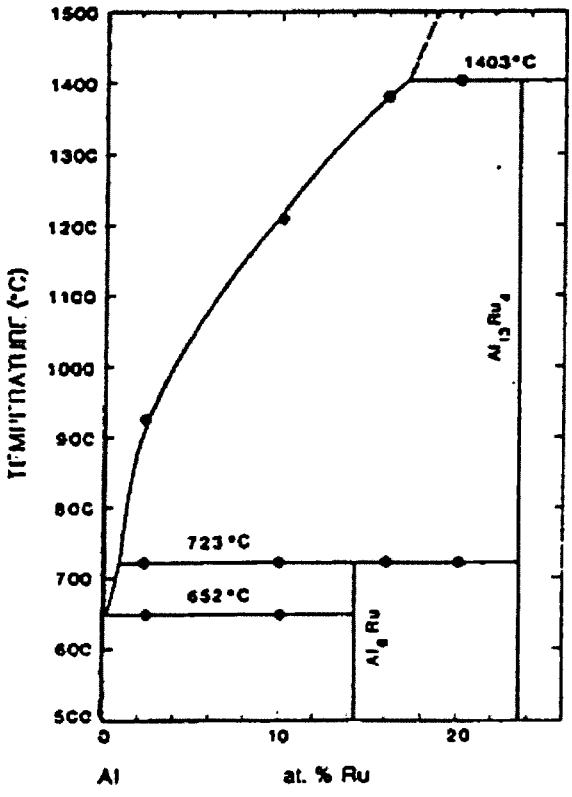

Figure 2.6. The phase diagram of Anlage *et al.* [1988Anl] for the high-Al corner in the Al-Ru system.

Anlage, Nash and Ramachandran [1988Anl] undertook experiments up to 26 at. % Ru using scanning electron microscopy, X-ray diffraction and thermal analysis (DSC) and proposed a revised phase diagram for the Al-rich portion of the Al-Ru phase diagram

(Figure 2.6). Confirmation of the $RuAl_{12}$ phase was not found. Edshammar's [1965Eds] notation for the Ru_4Al_{13} phase was used. It was also reported that both $RuAl_6$ and Ru_4Al_{13} melt by a peritectic reaction at 996 K and 1676 K respectively, and not congruently as suggested by Obrowski [1960Obr]. Some liquidus temperatures were provided. Problems with homogeneity of the alloys were reported, and also that the peritectic reaction forming $RuAl_6$, was sluggish. Under rapid solidification conditions, icosahedral phases were reported between 2.4 and 23.5 at. % Ru.

Boniface and Cornish [1996Bon1] confirmed Anlage's results for the high-Al end of the phase diagram. No evidence of the $L \leftrightarrow Ru_2Al_3 + RuAl_6$ eutectic reaction, reported by Obrowski [1960Obr], was found and the presence of $RuAl_2$ in as-cast samples over a specific range indicated stability at higher temperatures. The microstructures revealed that there was a peritectic cascade of reactions from the formation of Ru_2Al_3 to the formation of $RuAl_6$. A slight endothermic peak at 1733 K suggested the formation temperature for $RuAl_2$ [1996Bon2]. The Ru_2Al_3 phase was found to decompose at ~ 1223K.

Although Varich and Luykevich [1973Var] found a maximum solubility of Ru in (Al) of 3.23 at.% Ru by rapid solidification techniques, this solubility has not been reported for equilibrium conditions.

No assessment of the Al-Ru phase diagram, based on the CALPHAD method, had been published prior to this work.

2.3.2 Thermodynamic data

The only experimental thermodynamic value for the Al-Ru system was determined by Jung and Kleppa [1992Jun] by dropping a mixed 1:1 powder mixture (atomic percent) of the elements into the calorimeter, which showed that RuAl (B2) has a high heat of formation, $\Delta H_f = -124.1$ kJ.mol^{-1}.

Miedema's method was used to estimate values for the heats of formation for the intermetallic phases [1998Wol], as no other data were available.

Neumann, Chang and Lee [1976Neu], without using Obrowski's experimental data [1960Obr] used a theoretical method to predict that the RuAl phase has a very narrow phase width, probably not exceeding 1 at. % on either side of the stoichiometric composition. They suggested that RuAl is slightly off-stoichiometric and that the disorder parameter is less than 3.10^{-3}, indicating that RuAl is a highly ordered phase.

Several *ab initio* results have been reported for the enthalpy of formation of RuAl. However, the data are scattered, probably due to the different assumptions for defect formation in RuAl, which have been implied to be vacancies [1993Fle] or anti-structure defects [1976Neu]. Ngyen-Manh and Pettifor [1999Man] used the full-potential linear muffin-tin orbital (FP-LMTO) method within a local-density-function approximation

(LDA), while Gargano, Mosca, Bozolla and Noebe. [2002Gar] used the Bozzolo-Ferrante-Smith-based (BFS) Monte Carlo simulations. Hu *et al.* [1999Hu] applied an embedded atom model to calculate the enthalpies of formation for the phases, though most of their data differed vastly from the values estimated by Miedema's semi-empirical model. They have also misquoted data from the literature for the RuAl phase. However, their result for the Ru_4Al_{13} phase is in better agreement with the Miedema estimation.

The thermodynamic data are listed in Table 2.6.

2.3.3 Applications of Al-Ru intermetallics

The RuAl compound has an unusual combination of properties. Fleischer and co-workers [1991Fle] first reported the excellent room temperature toughness, compared to other intermetallic compounds, and recommended its potential for structural applications because of its high melting point and good oxidation resistance. The improved toughness is due to five independent slip systems in the crystal.

The excellent corrosion resistance of RuAl in hot, concentrated mineral acids was first reported by Wopersnow and Raub [1979Wop], and more recently, McEwan and Biggs [1996McE] demonstrated its capability as a coating in a range of aqueous media. They recognised that it has potential in corrosion-resistant coatings and electrochemical applications. The electrical conductivity of RuAl is high, almost metallic in value, and it exhibits good work function attributes [1995Smi]. This, and the good thermal conductivity [1998And] and a high wear resistance [1994Ste] also render the material suitable for lifelong spark-plug electrodes [1997Wol].

Although RuAl is difficult to manufacture by melting because of its high melting point, it can be manufactured by powder processing techniques, especially by reactive powder processing [1996Cor], or reactive hot isostatic processing (RHIP) [1996Wol].

Table 2.6 Enthalpies of formation for the phases in the Al-Ru system.

Phase	**ΔH_f** [kJ/mol of atom]	**Method**	**Reference**
$RuAl_6$	-17.930 ± 10%	Miedema semi-empirical method	[1998Wol]
Ru_4Al_{13}	-30.030 ± 10% -28.940	Miedema semi-empirical method Ab initio	[1998Wol] [1999Hu]
$RuAl_2$	-38.260 ± 10%	Miedema semi-empirical method	[1998Wol]
Ru_2Al_3	-44.040 ± 10%	Miedema semi-empirical method	[1998Wol]
RuAl	-47.320 ± 10% -62.050 ± 3000 -70.740 -58.150 -95.510	Miedema semi-empirical method Direct Solution Calorimetry *Ab initio* *Ab initio* *Ab initio* (BFS method)	[1998Wol] [1992Jun] [1992Lin] [1999Man] [2002Gar]

2.4 The Pt-Ru Binary System

The Pt-Ru phase diagram is rather simple in that there are no phases other than the two end-member solid solutions (Pt) and (Ru) and a two phase area comprising of (Pt) and (Ru). The phase diagram [1990Mas] is shown in Figure 2.7.

About 62% Ru dissolves in (Pt) at 1000 °C. A two-phase region of (Pt) and (Ru) exists between ~62 and ~80 at. % Pt. A ruthenium solid solution is observed above ~80 at. % Pt at 1000 °C. (Pt) forms by a peritectic reaction at ~2120 °C.

The Pt-Ru phase diagram has been calculated by Spencer using the CALPHAD method [1996Spe] and is shown in Figure 2.8. The calculated diagram is just an extrapolation of the elemental data. It is only in relative good agreement with the published ASM diagram [1990Mas], as it shows an eutectic reaction instead of the peritectic reaction, as in Figure 2.7. However, there are limited data available for the liquidus and solidus curves.

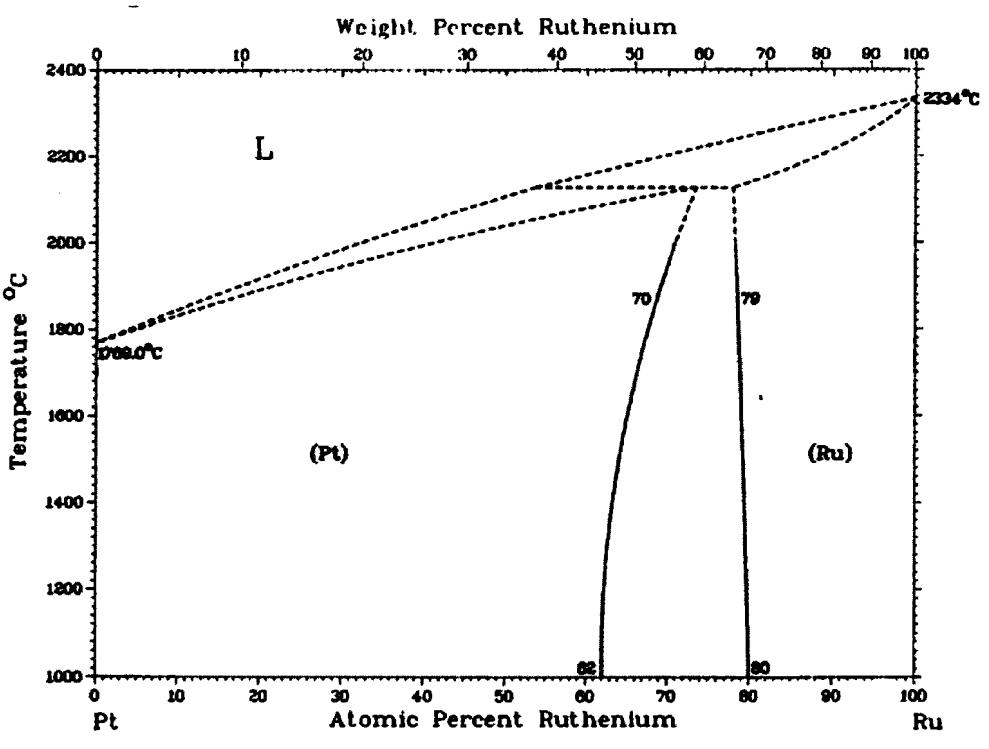

Figure 2.7. The Pt-Ru phase diagram [1990Mas].

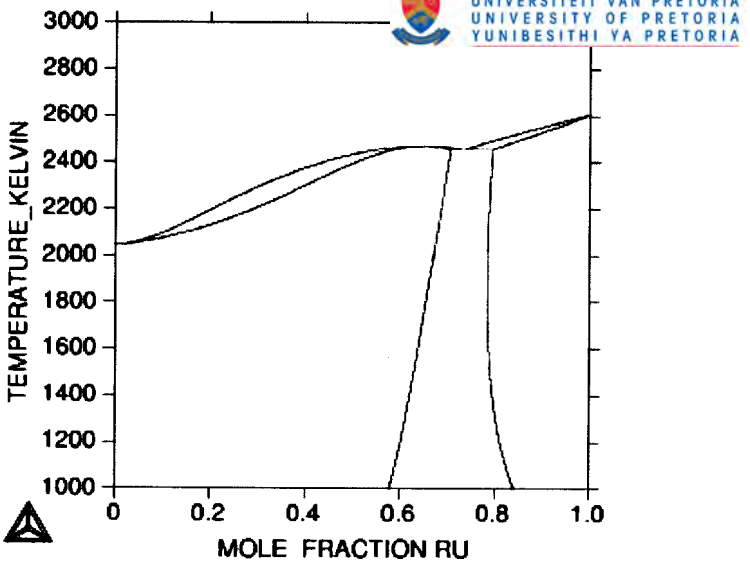

Figure 2.8. Calculated Pt-Ru phase diagram, from Spencer [1996Spe].

2.5 The Pt-Al-Ru Ternary System

The only published data is an isothermal section at 1350°C [2001Big1, 2001Big2, 2001Hil1]. No ternary reactions or ternary phases have been reported and very limited extension of the ~Pt_3Al phase into the ternary was observed. The isothermal section is shown in Figure 2.9.

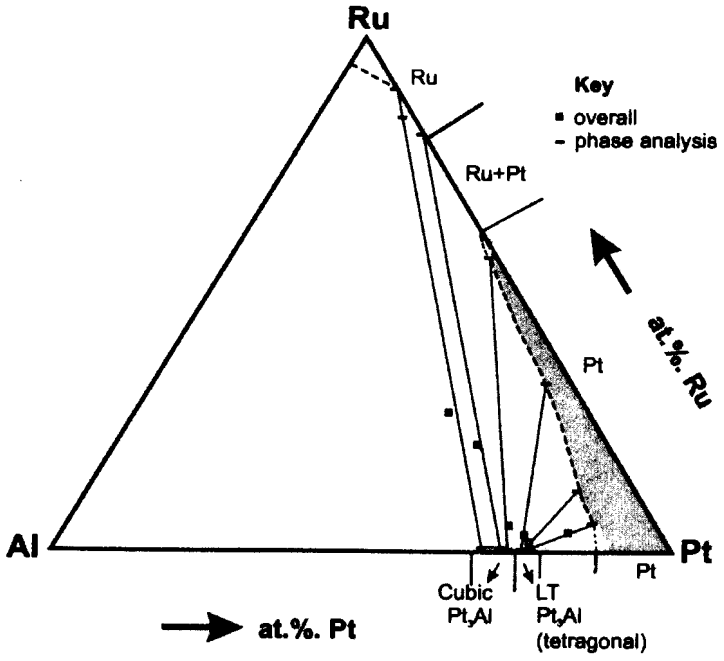

Figure 2.9. Isothermal section of the Al-Pt-Ru system at 1350°C [2001Big2].

Chapter 3
Experimental Procedure

This chapter describes the basic experimental procedures that were followed in this study. The methodology on how the solidification sequences and liquidus surface projection were determined is also presented.

3.1 Introduction

Sixteen samples were prepared in four stages. An initial set of six alloy compositions was selected after extrapolations from the binary phase diagrams to identify possible two-phase areas in the ternary. Two-phase samples were targeted because more information could be gleaned per sample. Samples were selected to have a lower Pt-content than the alloys investigated by Biggs [2001Big1] and Hill [2001Hil1], as their work covered the platinum-rich corner. The highest platinum composition sample was selected to be the same composition as the lowest platinum composition sample from Biggs [2001Big1] in order to benchmark this set of samples. Samples were also selected away from the ruthenium-rich corner since previous experimental work on the Al-Ru system indicated that there is only the eutectic reaction above 50 at. % Ru and such a sample would not give new information.

Six more alloy compositions were selected later to clarify uncertainties raised by the results of the first set of samples. Three more samples were subsequently prepared in order to complete the liquidus surface projection. A final sample was prepared to confirm a ternary phase found in the alloy system.

3.2 Sample Preparation

The as-cast samples were prepared at Mintek, according to their standard preparation method PMD-SOP-037. The samples were prepared by arc-melting on a water-cooled copper hearth, using elemental powders of at least 99.9 percent purity. Three grams of powder were mixed by hand. No binders were used. The powders were compressed before melting under a protective argon atmosphere. Samples were re-melted five times to ensure homogeneity. Samples were turned upside down between each re-melt. Six samples could be prepared per arc-melt.

The arc-melting electrode was equipped with a tungsten-metal tip. No mass-loss measurements were performed on the electrode tip, but no evidence of any detectable tungsten uptake by the samples was found in the composition analyses of any of the phases.

The mass losses of the samples were monitored. All the recorded weight losses were less than 5 %, which were considered acceptable since aluminium is almost always lost during arc-melting as it has a much lower melting point than platinum and ruthenium, and a very high partial pressure. Mass losses were only recorded for the first six samples.

The cooling rate of the arc-melted samples is not known, but it was not sufficiently fast enough to totally freeze in the as-solidified liquidus-solid structure, as some coring was observed in some samples, which indicated that there was time for some diffusion on cooling.

Additionally, the cooling rate was also not fast enough to freeze in the high temperature binary phases or a new high temperature ternary phase, which was found in this study, as solid-state decompositions were observed in the microstructures.

Arc-melted samples were cut into two pieces. The high aluminium content samples were brittle and cracked when they were fastened in the vice for cutting. The more ductile samples were cut with a diamond wheel in a Struers Accutome. One half was mounted in a conductive resin and prepared metallographically to a 0.25 μm finish.

3.3 Analyses

3.3.1 Scanning electron microscopy and Energy Dispersive X-ray Analysis (SEM/EDS)

All imaging was conducted in the backscattered electron (BSE) mode for phase contrast, on a LEO 1525 field-emission scanning electron microscope (FE-SEM). BSE mode is suitable for phase analysis, as the intensity of the backscattered electrons is a function of the atomic number of the phase, so different phases have a different amount of backscattered electrons associated with them and this shows as different shades of grey in the resulting micrograph. The higher the average atomic number of the phase, the more electrons are backscattered and the brighter the phase appears in the micrograph.

The overall and phase compositions of the samples were determined using an Oxford INCA energy dispersive X-ray (EDS) system attached to the abovementioned SEM. The resolution of the EDS detector was 132 eV. The accelerating voltage was optimised for the alloys using the Oxford Inca Spectrum Synthesiser, since all samples could only contain Al, Pt and Ru. The synthesiser program models the spectrum, taking into account the input variables for EDS, as well as the energy lines which will be used for analysis. The acquisition conditions can be optimised taking into account the elements present in the sample. This ensured that excessive over-voltages were not used in generating the X-rays for EDS, as this could influence the results significantly. All samples were analysed at 12 mm working distance (optimum for the SEM used) and 12 kV accelerating voltage. All the EDS analyses were done quantitatively against pure element standards.

The microstructures of the samples were visually inspected in the SEM prior to analysis to ensure they were homogenous. Some samples had a small fraction of unreacted Ru in them. In these cases, the areas adjacent to the Ru were avoided in the analysis. The presence of the Ru was not considered a problem as previous sample preparations involving Ru at Mintek has shown that Ru tends to agglomerate and form lumps, especially in the small samples which are mixed by hand. It is also possible that the Ru did not melt properly, as Ru has a very high melting point (2701 K).

Overall compositions were determined by scanning a sufficiently large area of the sample, 200 – 1000 times magnification, depending on how coarse the microstructure was. Five overall analyses were recorded per sample.

The composition of each phase was recorded in spot mode in the SEM. At least five spots were measured for each phase and for each phase the standard deviation was calculated. In some samples the phases were present on a very fine scale, which complicated results, since the spatial resolution of EDS analysis is not lower than 1 μm. X-ray information in EDS comes from an interaction volume from about 5 to 2 μm under the surface of the sample,

depending on the operating conditions and average atomic number of the phase, which means that for fine particles, there could be a big matrix contribution. In these cases, more analysis points were recorded, and were taken into account in the plotting of the results on a ternary projection, as the composition of the two phases must lie on the tie-line between the two phases. Due to this, phases could not always be assigned beyond doubt using EDS, thus X-ray diffraction (XRD) was used to confirm phases.

It should be noted that since all samples were analysed at the same conditions, the standard deviations reported in this study only reflect the composition deviations and are not true uncertainties associated with EDS analysis. EDS is only accurate to a minimum of ± 1 at. % due to counting statistics, detector resolution, beam-sample interactions and a number of other factors. However, these factors have been assumed constant in this study as all the samples contained the same elements and all the conditions were constant. Depending on operating conditions, EDS also has a minimum detection limit of 0.5 - 2 at. %, which means that low concentrations of one of the elements in a binary phase could not always be detected. Thus, the uncertainty for elements present in low atomic percentages was much higher. Again, all factors were assumed constant and low atomic concentrations have been reported in the same way as higher concentrations.

3.3.2 X-Ray Diffraction

The samples were broken out of the resin mounts and analysed in a Philips XRD, with monochromated Cu Kα radiation using a continuous scan from 4 to 90° 2θ with step size of 0.02° and dwell time of 0.5 s, to confirm the phases found in EDS.

XRD is a suitable technique for phase analyses incorporating lattice parameter and lattice-type determinations on crystalline materials. XRD can also be used to determine and evaluate the effect of a solute on the lattice parameter of a phase.

XRD is based on Bragg diffraction. When a crystalline material is irradiated by a monochromatic source of X-rays, reflections will occur from the various lattice planes in the crystal. Each reflecting plane will diffract a portion of the X-ray beam as governed by the relationship

$$n\lambda = 2d \sin\theta$$

where
λ = wavelength of the incident radiation
d = interplanar spacing
θ = incident angle of radiation with the plane
n = a small integer.

The reflections are characteristic for a specific crystal structure and give the d-values for a phase, from which the lattice parameter can be calculated through the relationship (for a cubic phase)

$$d^2 = \frac{a^2}{h^2 + k^2 + l^2}$$

where d is the interplanar spacing, a is the lattice parameter and h, k and l are the Miller indices, referring to the plane from which the reflection originates. The positions of the atoms in the unit cell are then determined by the space group.

Phases are identified in XRD by matching the phase under investigation to standard patterns, which are available in the International Crystallography Diffraction Database (ICDD) [2001ICD] and International Crystal Structure Database (ICSD) [2002ICS]. However, there are many phases not yet included in these databases, and the standard patterns are normally only for end-member phases, solid solutions are usually not included.

Many of the phases found in the Al-Pt and Al-Ru binaries are not included in the ICDD or ICSD. Most of the binary phases showed solubility for the third element in the system, which shifts the position of the reflections. Some of the diffraction patterns also had overlaps on the major peaks. These complicated the XRD identification significantly and a different approach to only matching recorded and standard patterns had to be followed to confirm the phases proposed by EDS analyses.

A method that is used at the CSIR-NML has been followed to identify the phases. This method uses a software program WinCell [2002Raj], a freeware program from the internet, to refine lattice parameters, based on the crystal structure, d-values and (*hkl*) values for a phase. From the crystal structure data reported in the literature for the pure binary phases, the lattice parameter and reflections present in the spectra were known.

The method comprised the following steps:

1. For the phases that were present in the ICDD or ICSD, the lattice parameters were calculated in WinCell from the standard pattern data in the database. For phases which were not in the databases, but for which prototypes have been suggested in the literature, the lattice parameters of the prototypes have been calculated. For some phases very limited data were available and in those cases related binary systems were searched to find suitable prototypes. Some phases have more than one prototype suggested in the literature, in these cases all the prototypes were evaluated, as there are some discrepancies in the binary phase diagrams. This provided a starting set of values for each phase.
2. Once a 'standard' has been set up in WinCell, the corresponding phase was evaluated. The corresponding 2θ values from the diffractogram were selected for input to WinCell and a lattice parameter was calculated and refined through a non-linear regression method. A standard deviation and an overall coefficient of determination, R^2, are also calculated for each phase.

In Appendix B the XRD spectrum, the ICDD data of the phases to be confirmed, the WinCell inputs and results are presented as an example.

Unfortunately, in WinCell it was not possible to assign different weights to the relative intensities of the reflections in the diffractogram, which sometimes complicated the calculations. But this method also ensured that all phases were, as far as possible, identified, as the number of lines in the difractogram that were not already assigned to a phase could be identified.

The advantage of this approach was that phases could be identified with a figure of merit, the R^2 value, and that the shifts due to the presence of a third element in the binary phase lattice were taken into account, making it possible to calculate the solid solubilities of the phases.

Two new ternary phases were also found in the study. The one phase is a high temperature phase and was found in only one sample. It was not quenched into the microstructure, and decomposed. This phase is referred to as phase T in this study. The other ternary phase, called phase X in this study, was stable to room temperature and present in a number of samples. Through a search and match procedure, a structure was found which matched the diffraction patterns of this phase. This was then used as a prototype for phase X.

3.4 Methodology to determine a solidification sequence for a ternary alloy

In order to determine a solidification sequence of an alloy and then propose a liquidus surface projection, also called the polythermal projection of the liquidus, fundamental thermodynamic principles as well as practical experimental observations have to be considered. This section attempts to describe the basic method which was used to propose the solidification sequences and liquidus surface projection.

3.4.1 Analyses of as-cast alloys

Overall compositions were determined for the samples. The phases in the microstructure were then analysed. EDS is a useful tool to determine the compositions of the phases as well as the overall composition of the alloy. The composition results from the EDS analyses were plotted on a ternary composition triangle. In this study all the overall compositions are indicated with a solid square on the diagrams and the phase compositions are indicated with solid triangles. These are shown in Figure 3.1. When there were only two phases present in a sample, the overall composition had to be on the line connecting the two-phase compositions. When there were three or four phases present, the overall composition had to fall within the area formed when the phase compositions are connected, as shown below for the triangular area.

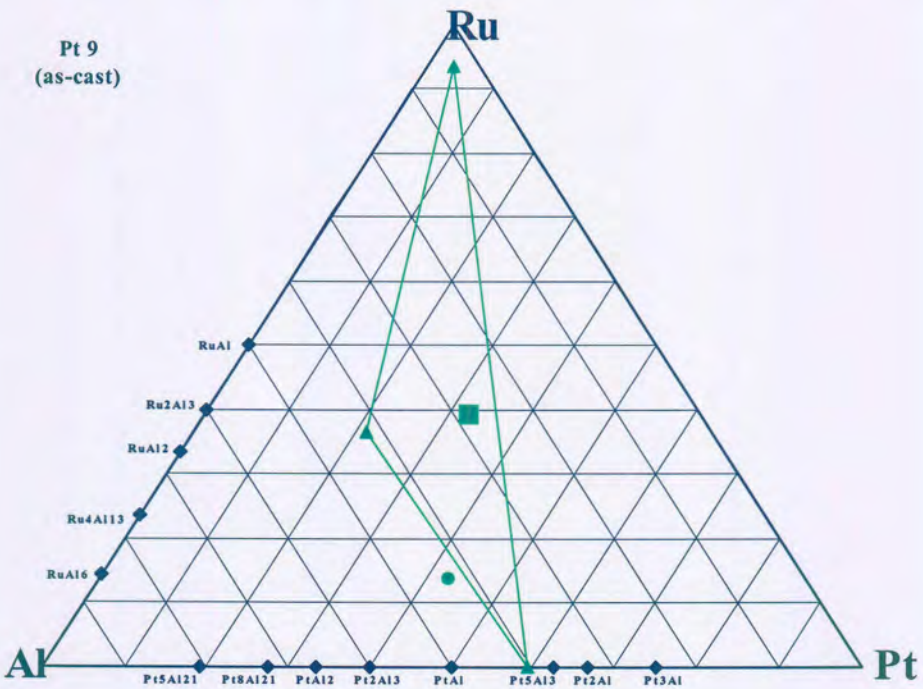

Figure 3.1. Ternary plot showing the EDS phase analyses. The square indicates the overall composition, the triangles the phase analysis and the solid circle indicates a two-phase area.

Since EDS only gives the compositions of the phases, and not the structures, XRD analyses had to be used to confirm the phases in the sample. The phases confirmed by XRD were assigned to the phase compositions on the ternary plot. This had to be in agreement with the binary phases on the axes of the ternary diagram, unless it was a ternary phase, for which there is no extrapolation to the binaries that make up the ternary diagram.

The shapes of the phases in the microstructures were also evaluated qualitatively. Did the phase form dendrites in a matrix? Were the dendrites coated with another phase? Was the area between the dendrites a mixture of two phases? Which phase was coating what? These are important considerations in determining the solidification sequence and in identifying what type of reaction (monotectic, eutectic or peritectic) occurred.

Phases solidify in a sequence. The order of the sequence is very important, because it gives the order of the reactions.

3.4.2 Fundamental and theoretical considerations

Once the experimental analysis data were consolidated, certain fundamental and theoretical factors were considered to propose a solidification reaction sequence and to plot a proposed liquidus surface projection for the Al-Pt-Ru system. These are outlined below. Although discrepancies can occur between the theory and experiment, these should not detract from the usefulness of the theoretical approach, since the theory can provide useful ideas on the phase growth and resulting experimental microstructures.

This discussion is only a rough guideline to the possible fundamental and theoretical considerations, as non-equilibrium solidification of multi-element liquids is complex and it is influenced by many factors. Predicting what will happen only theoretically is, today, still nearly impossible.

3.4.2.1 Phase Diagram Considerations

<u>The Phase Rule</u>
During equilibrium solidification, the phase rules must be obeyed. The phase rule is

$$F = C - P + 2$$

where F is the degrees of freedom, C is the number of components and P is the number of phases, and it describes the relation between the phases and system variables (temperature, pressure and composition). At constant pressure, the rule reduces to

$$F = C - P + 1.$$

Although the non-equilibrium freezing of the arc-melted samples is too fast for equilibrium solidification, and compositions constantly change during the non-equilibrium freezing, a local equilibrium at each interface can be assumed, and the basic principles of the phase rule should be considered in considering and evaluating the invariant reactions.

<u>Reactions in a ternary system</u>
In a ternary system, all the reactions from the binary systems are possible in the ternary system, as well as some ternary reactions. The most commonly observed ternary reactions are [1965Wes]:

(i) ternary eutectic reactions $L \rightarrow \alpha + \beta + \gamma$,
(ii) ternary quasi-peritectic reactions $L + \alpha \rightarrow \beta + \gamma$
(iii) true ternary peritectic reactions $L + \alpha + \beta \rightarrow \gamma$.

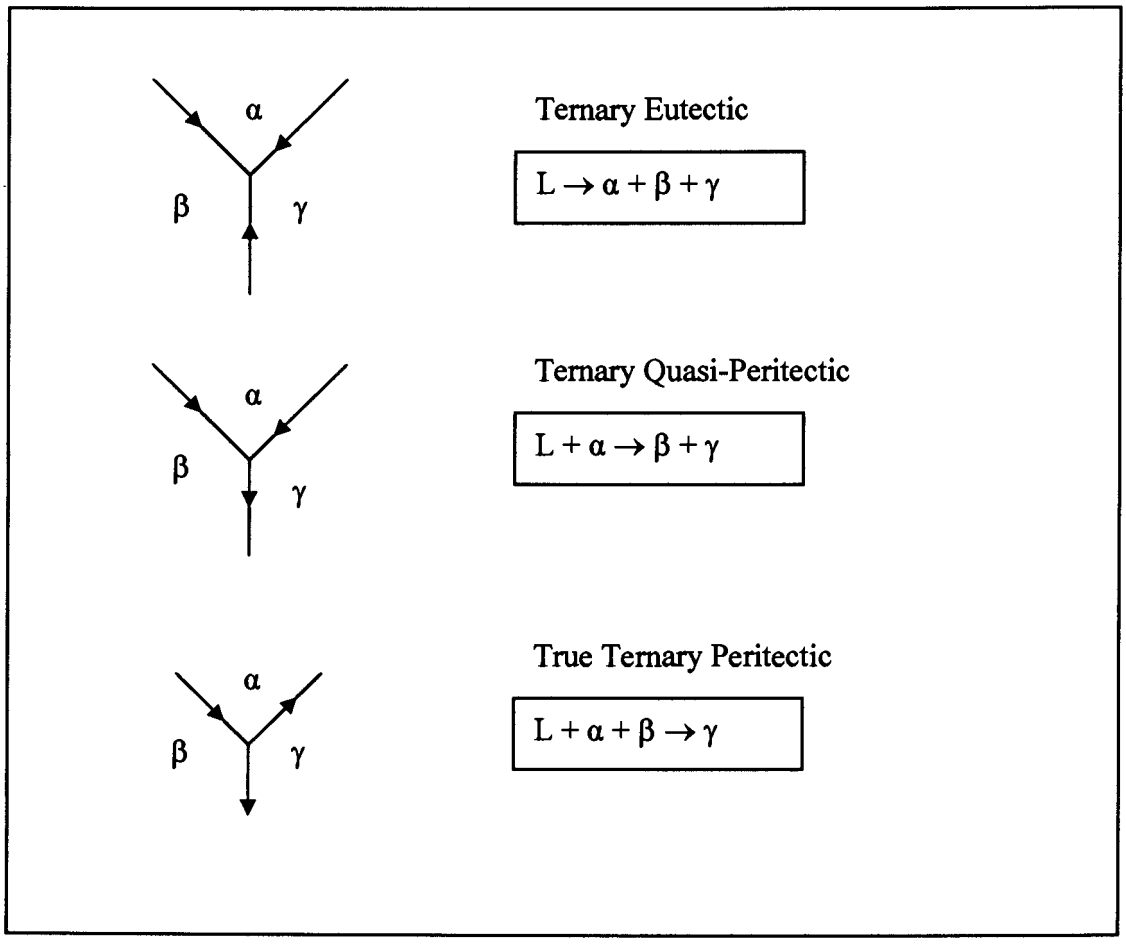

Figure 3.2 Ternary invariant reactions, after West [1965Wes].

These ternary reactions are illustrated in Figure 3.2, where the arrows on the liquid surface point in the direction of decreasing temperature. Reaction (ii) is also sometimes referred to as a 'weak' peritectic reaction.

It is important to note that a reaction which is an eutectic reaction in the binary, can appear as a peritectic reaction in the ternary. The presence of a third element in the ternary can change the compositions of the binary phases when the third element is dissolved in the binary phase in the ternary system. This can change the Gibbs energy of the phase so that the relative stabilities of the phases change. Thermodynamically, a eutectic reaction can become a peritectic reaction. In some cases, the eutectic reaction was observed before the conditions for the eutectic became unstable, in other cases the eutectic from the binary was not observed at all, only the peritectic reaction was observed. Also, if cooled too quickly, a stable eutectic reaction can become a metastable peritectic reaction.

3.4.2.2 Liquid-solid interactions and transformations

Some fundamentals on liquid-solid transformations were considered. Solidification of an alloy from the liquid consists of nucleation of the primary solidification phase in the liquid, and then the growth of the phase into the liquid, consuming the liquid, until all the liquid is solidified.

Nucleation
Nucleation is always associated with a change in crystal structure, a change in volume or a change in composition. Embryos form in the liquid, and once these reach a critical size and become thermodynamically stable, a stable nucleus is formed.

Solid-liquid interactions
The liquid-solid interface of the growing solid nucleus shows three characteristic features[1972Cha]:

(i) the interface is non-crystallographic and atomically rough;
(ii) the interface is planar, i.e. contains no projections;
(iii) the interface is isothermal and undercooled by an amount ΔT related to the growth rate.

Not all of above is necessarily observed.

The growth of the nuclei is then dependent on the interface energy, surface energy of the nuclei and amount of undercooling. Liquid metal must undercool by a few degrees before solidification begins. The type and direction of grain growth is controlled by the temperature gradients at the solid-liquid interface. It is also dependent on the alloy composition.

As solidification continues after nucleation, temperature gradients develop. The gradients develop during the transport of the latent heat of fusion from the interface, produced by the formation of the solid phase. If the liquid-solid interface grows into a supercooled liquid (negative temperature gradient), protrusions at the interface can grow into the liquid without being melted back, resulting in dendritic growth. If the temperature gradient ahead of the interface is positive, then grain growth occurs by the advancement of a more stable solid-liquid interface. The liquid can also be supercooled by both thermal and constitutional effects, then seed crystals can appear, which can grow into equiaxed, dendritic or columnar crystals.

It is often that the bulk sample solidifies with a dendritic morphology. Dendrites grow in quite specific crystallographic directions. Dendrites can have a cellular appearance, or branches can develop to produce a tree-like appearance, depending on the composition and temperature gradients. However, the morphology of the primary phase also depends on the surface energy of the primary phase, and when growth in a specific crystal direction in the liquid is not thermodynamically favoured, discrete particles can form in the liquid. The discrete particles grow without direction preference or they can form facetted crystals.

The growth of the primary phase continues until the remaining liquid composition is too saturated with elements rejected from the solid and the phase cannot grow anymore. This is assuming that most of the partitioning of the elements occurs in the liquid and not in the solid. Then three types of liquid-solid interactions are possible. Eutectic, peritectic and monotectic reactions occur most often in a ternary system. For eutectic and peritectic reactions, the liquid phase is in equilibrium with two solid phases. These are recognised by their different morphologies [1972Cha]. The peritectic reaction can continue only whilst the phase being

coated is still in contact with the liquid. For a monotectic type reaction, a miscibility gap must exist in the liquid.

The further sequence of solidification is then determined taking into account the shape of the microstructure.

Eutectic reactions are the simultaneous solidification of two phases and the two phases are always finely dispersed. The morphology could include globular, rod-like, lamellar and more irregular shapes (see Chadwick [1972Cha] for detail on eutectic morphologies). In peritectic reactions, the phase which formed peritectically formed directly on the phase which reacted with the liquid, in other words, the phase which formed peritectically 'coated' the primary phase. Since the liquid reacted with the primary phase, the latter could have an uneven appearance.

Solid-state eutectoid reactions occur where a phase had been formed during solidification and it is not stable at lower temperatures. A solid-state decomposition is characterized by a very fine structure if a high nucleation rate was attained. In the time during rapid solidification, the structure remains fine, as the diffusion rates are much less in the solid, and at a lower temperature than solidification from the liquid.

Coring is also possible in as-cast samples. Coring means that individual dendrites do not have the same composition from the center to the outer edge of the dendrite. This is due to the fact that the composition of the solidifying liquid, as well as the temperature of the liquid, is changing as the dendrite grows from the liquid. The composition of the liquid is either enriched or depleted of a solute, thus the solute concentration in the dendrite differs from the surrounding liquid, and the phase solidifies in a continuous layered structure until the liquid concentration has changed and the phase cannot precipitate anymore (Figure 3.3).

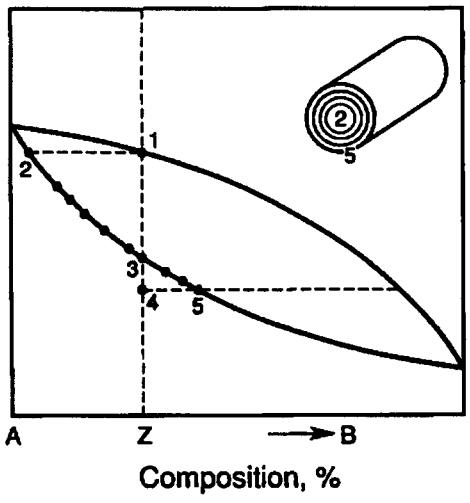

Figure 3.3. Phase diagram of two components showing the influence of solute diffusion on solidification, a phenomenon called coring [1990Tom].

3.4.2.3 Deriving the solidification sequence and liquidus surface projection

The proposed solidification sequence and liquidus surface projection were derived from the experimental microstructures. Drawing a liquidus surface projection is a bit like building a jigsaw puzzle, as a number of factors need to be considered.

For each alloy a solidification sequence was deduced. The primary phase was identified, and the solidification reactions were proposed as eutectic or peritectic, following the shape of the microstructure. These deduced solidification sequences for the alloys were used to derive the liquidus surface projection.

The overall composition of an alloy falls on the liquid surface of the primary phase. Furthermore, the surfaces of phases in a particular solidification reaction had to be in contact on the liquidus surface projection. The solidification reactions also had to agree with the liquid reactions found in the binaries, although, as described above, the reaction types could have changed based on the relative thermodynamic stabilities of the phases when third elements are dissolved in the binary crystal structures.

The proposed solidification sequence had to be consistent with the microstructure. The order of the phases in the microstructure, from the primary phase to the final phase solidified, had to be such that there were no extra phases in the microstructure between two consecutive phases in the solidification sequence. The cooling of the as-cast alloys was too fast to allow phases to form through diffusion alone, although it was not fast enough to prevent coring and solid state decomposition. Although quite unusual in as-cast alloys, it is possible that in some cases a phase is not observed, since in some peritectic reactions all the previously formed phase can be consumed during the reaction. In such cases, only a small part of the liquid surface of the consumed phase could fall on the solidification path on the liquidus surface projection. The solidification reactions had to agree with the liquid reactions found in the binaries, although, as described above, the reaction types can change based on the relative thermodynamic stabilities of the phases when third elements are dissolved in the binary crystal structures.

Since three binary systems were involved, and ternary phases could be present, the solidification microstructures were used as input to the solidification sequence. Usually the same order of formation for the phases from the liquid had to occur in the ternary system. It was also considered that the presence of a third element in a binary structure could change the composition range and formation temperature of the phase. The formation temperatures of the phases from the liquid in the binary systems were also used to give an indication of the solidification sequence.

The proposed liquidus surface projection was evaluated against the solidification sequences to ensure consistency between them. This is best explained with an example. If one considers the alloy composition 14 (overall and the phase compositions) plotted on a liquidus surface projection (Figure 3.4), the primary crystallisation product will be RuA_2, since the overall composition lies on the $RuAl_2$ liquidus surface. $RuAl_2$ is not a stoichiometric line compound in the binary system; it shows a small solubility range, which extends more to the Al-side than the Ru-side (Figures 2.4 and 2.5 in Chapter 2). The crystallisation path of the liquid will be along a line roughly towards the overall composition and the phase composition of $RuAl_2$. If $RuAl_2$ had been a line compound, the crystallisation path of the liquid would have been on the straight line between the overall composition and the $RuAl_2$ composition on the Al-Ru side of the ternary plot. The solidification of $RuAl_2$ continues until the liquid attains a composition on

the univariant valley, the boundary between the $RuAl_2$ and X liquidus surfaces. The direction of continued solidifications is determined by the direction of the liquidus slope (valley or 'kink'), as well as the steepness of the slopes of the adjoining liquidus surfaces. The solidification can continue down the valley in a eutectic, or go over the adjoining liquidus surface if the slope permits it in a peritectic. In the example, the solidification continues in a peritectic way over the liquidus surface of phase X, until the liquid compositions reach the univariant boundary between X and $PtAl_2$. The solidification continues down the valley, until there is no more liquid to consume.

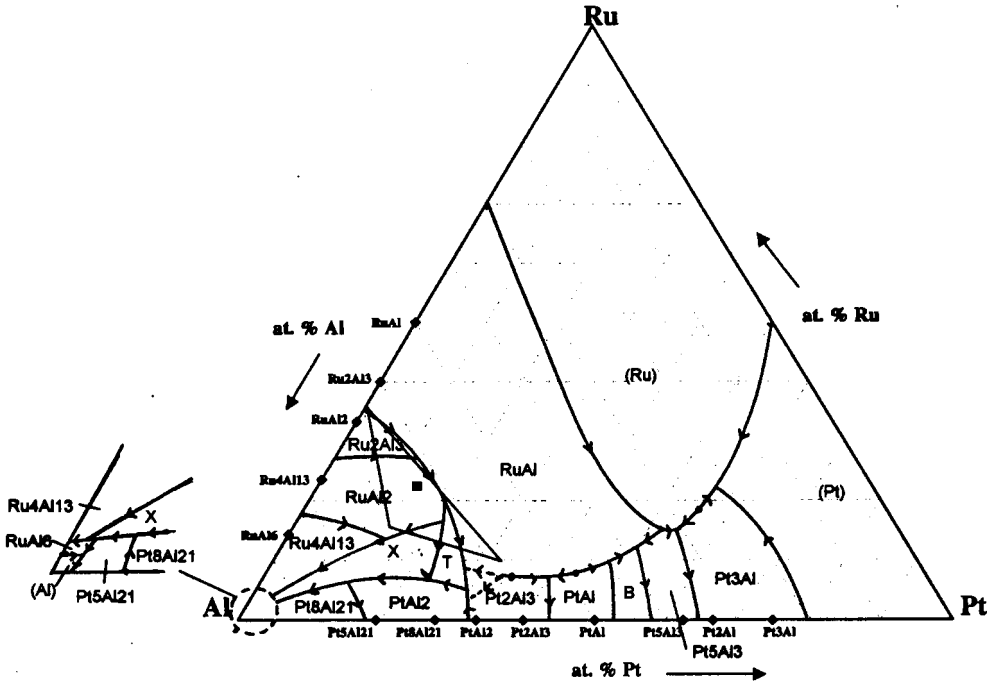

Figure 3.4. Sample 14 on the liquidus surface.

Pelton [1995Pel] presented the solidification of a ternary alloy in more detail. However, only stoichiometric line compounds were considered in the discussion.

It is possible that, in some cases, the path of solidification crossed a liquidus surface of a phase which is not observed. In such a case, the phase probably was consumed during a peritectic reaction and it was not observed in the solidification microstructure, especially for a small liquidus surface. In cases where the two adjacent liquidus slopes are both very steep, the solidification path might have 'jumped' to the other surface before the univariant boundary between the two phases was reached.

Although the solidification occurred under non-equilibrium conditions, the Gibbs phase rule should be obeyed in the liquidus surface projection. For a ternary system at constant pressure, the phase rule becomes $F = 4 - P$, where F is the degrees of freedom and P is the number of phases. When the liquid and one solid phase are in equilibrium, $P = 2$, thus $F = 2$ and the system is bivariant. A ternary liquidus is thus a two-dimensional surface. At a ternary eutectic point, $F = 0$ as the temperature and the composition for all four phases (liquid, α, β and γ) in equilibrium are fixed. Thus, in a ternary system, only three phases can be in equilibrium at any stage, so no more than three lines could meet in an invariant point on the liquidus surface.

3.5 Syntax and terminology

Solidification reaction sequences are sometimes written in "short hand", without indicating the remaining liquid on the right hand side of the equation. Thus, in this work, solidification reactions were written as

$L \rightarrow \sim RuAl$

$L + \sim RuAl \rightarrow \sim PtAl_2$

$L + PtAl_2 \rightarrow X$

with the above actually implying more explicitly, the following

$L_1 \rightarrow L_2 + \sim RuAl$

$L_2 + \sim RuAl \rightarrow L_3 + \sim PtAl_2$

$L_3 + \sim PtAl_2 \rightarrow X$

In some instances, a '~' sign is put in front of a binary phase. This indicates that the binary phase shows some solubility for the third element in the system, and that the phase is slightly changed from the pure binary phase. The '~' sign is also sometimes used to represent a non-stoichiometric binary phase.

The end members of the ternary phase diagram (the corners) are the solid solutions of aluminium, platinum and ruthenium, dissolving varying amounts of the other two elements in the system. These solid solutions are indicated in parentheses: (Al), (Pt) and (Ru).

A line compound describes a phase with no solubility range. A phase is stoichiometric when it appears at its stoichiometric composition in the phase diagram.

Chapter 4
Results and Discussion of the Experimental Investigation.

This chapter presents and discusses the results of the experimental work.

The first part of the chapter deals with the analyses of the alloy samples, evaluating the microstructures and proposing a solidification sequence. The XRD results and observations are discussed. An overall solidification sequence for the Al-Pt-Ru system is presented and a liquidus surface projection is proposed. Some conclusions are made from the experimental results.

4.1 Introduction

Sixteen samples were analysed in the as-cast condition. The alloy compositions of the alloys studied are shown in Figure 4.1. The targeted and analysed compositions are listed in Table 4.1. The microstructures were investigated in the SEM, the overall compositions determined and the phase compositions were analysed with EDS, and confirmed by XRD where possible.

Six samples (1-6) were initially selected. A further six (7-12) was prepared to shed more light and clarify discrepancies from the first six samples. A further three samples (13-15) were prepared to glean more information in unclear areas of the system. As new ternary phase was suspected, a final sample (16) was prepared, the composition of this sampled was specifically targeted in the are of this sample. Samples were not prepared for the high platinum side, since that have been covered in two previous studies [2001Big, 2001Hil]

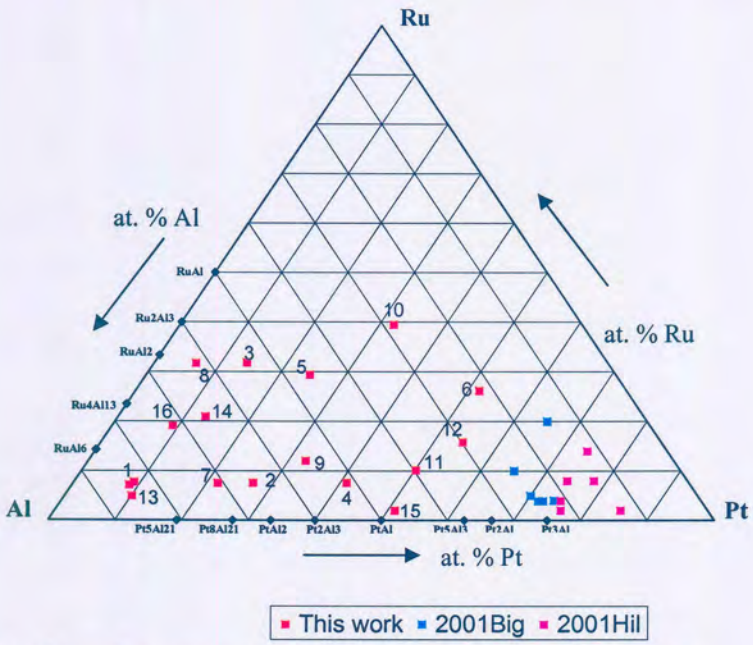

Figure 4.1. Overall compositions of the Al-Pt-Ru alloys studied.

Table 4.1. Targeted and analysed compositions for the experimental alloy samples.

Sample	Targeted Composition (at. %)			Analysed Composition (at. %)		
	Al	Pt	Ru	Al	Pt	Ru
PAR 1	86	7	7	84	8.5	7.5
PAR 2	66	26	6	65	26.9	7.6
PAR 3	57	12	31	54.4	13.8	31.8
PAR 4	54	38	8	51.6	40.9	7.6
PAR 5	50	25	25	43.6	26.5	29.9
PAR 6	25	55	20	21.4	51.7	26.2
PAR 7	73	22	5	70.8	21.6	7.6
PAR 8	71	7	22	62.0	6.2	31.8
PAR 9	59	33	8	55.4	32.5	12.1
PAR 10	34	40	26	28	32.6	39.5
PAR 11	42	52	6	39.7	50.1	10.2
PAR 12	33	59	8	29.9	54.3	15.8
PAR 13	85	10	5	87.6	8.5	4
PAR 14	66	13	21	64.0	13.6	22.4
PAR 15	47	51	2	42.0	55.7	2.3
PAR 16	74	8	18	71.9	8.9	19.2

From Table 4.1 it can be seen that in most cases the analysed Al composition was lower than the targeted composition, while the Ru composition was higher. This was expected, as Al has a much lower melting point than both Pt and Ru. Since some unreacted Ru was observed in some samples, the lower Al content observation was not consistent throughout all the samples, e.g. PAR13, which showed a higher Al content in the analysed results than what was targeted.

Porosity was observed in a number of samples. This was probably due to the fast cooling rates and the presence of Al, which has a much lower solidification temperature and higher partial pressure than Pt and Ru, leading to vaporisation. It could also have been due to traces of water vapour, despite precautions, in the samples prior to the arc-melting.

4.2 Microstructures and proposed solidification sequences

Each alloy sample was analysed, the phases determined and a solidification sequence was proposed for each alloy. These are discussed here, the XRD results will be discussed separately in paragraph 4.3.

4.2.1 PAR 1 - Al_{86}:Pt_7:Ru_7 alloy

The as-cast button was extremely brittle and crumbled into small pieces while clamping it in a vice to cut in half.

The PAR 1 alloy exhibited two distinctly different regions in the microstructure (Figure 4.2a and b). The composition of the two areas, however, was not significantly different. The origin of the two different structures is difficult to explain due to a lack of data, but,

since the coarser phase was observed mostly on the outside of the sample, it could be that columnar liquid dendrites with a very slight difference in composition formed and that it was enough to follow different solidification paths. The 'coarser' microstructure (Figure 4.2 d) shows light dendrites in a dark matrix, with some precipitation in the matrix. The 'finer' microstructure (Figure 4.2 c) shows a light phase coated by a darker phase in a dark matrix, also with some precipitation in the dark matrix.

The phase compositions are given in Table 4.2 and are plotted on a ternary projection in Figure 4.3.

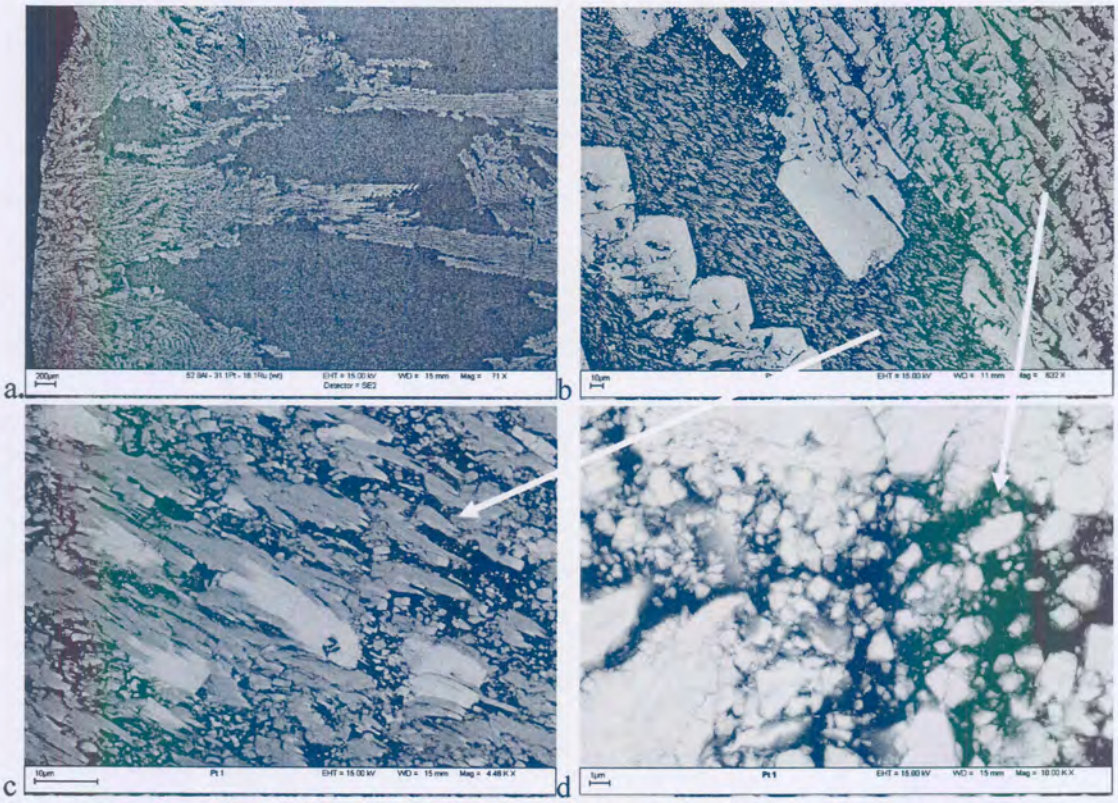

Figure 4.2. (a) and (b) show the two distinct different microstructure areas observed in the PAR1 alloy. (c) shows the detail of the finer (darker) microstructure and (d) shows the detail of the lighter, coarser microstructure area.

Table 4.2. Summary of phase and composition analysis for the PAR1 alloy.

Sample	Condition	Phase Description	Composition			Proposed phase(s)	No of analyses
			Al	Pt	Ru		
PAR 1	Arc-melted	Overall	84.0 ± 0.6	8.5 ± 0.5	7.5 ± 0.6		5
		Fine microstructure	84.3 ± 0.6	8.5 ± 0.6	7.2 ± 0.6		5
		Black	100			(Al)	3
		Grey	76.1 ± 1	10.5 ± 0.7	13.4 ± 0.6	X	10
		Light	75.1 ± 0.2	20.8 ± 0.5	4.1 ± 0.5	~Pt_5Al_{21}	9
		Coarse microstructure	83.3 ± 0.6	8.9 ± 0.6	7.8 ± 0.6		5
		Black	100			(Al)	3
		Very light	75.1 ± 0.3	14.1 ± 1.3	10.8 ± 1.1	X	6
		Grayish	72.8 ± 0.2	13.9 ± 0.7	13.3 ± 0.7	~$RuAl_6$	5

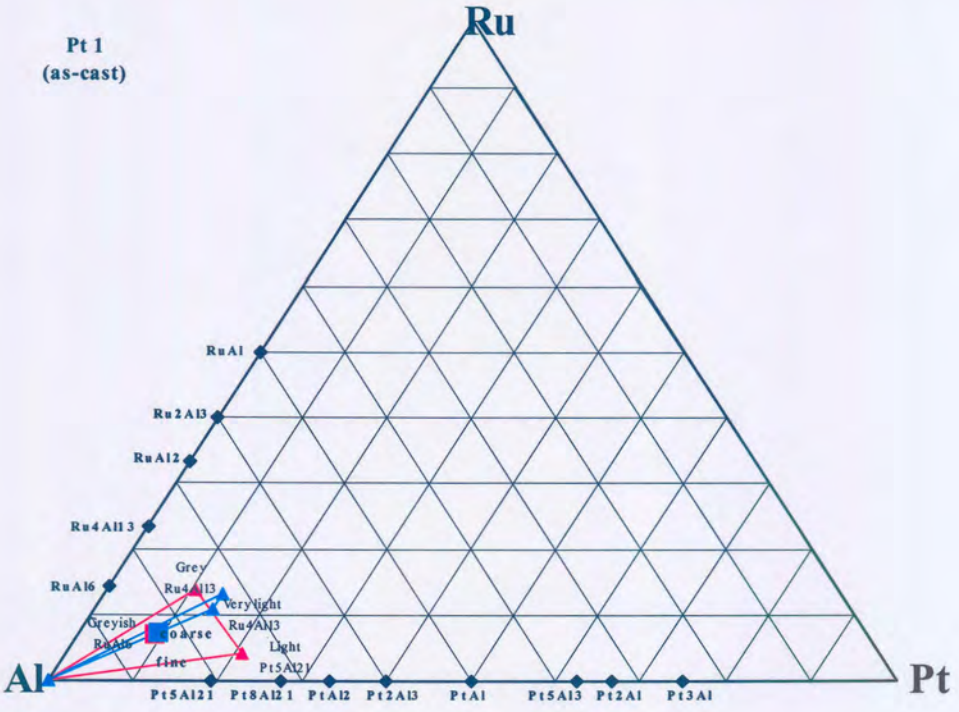

Figure 4.3. A ternary plot of the overall and phase compositions in the PAR 1 alloy.

In the 'coarse' microstructure, the ternary phase X solidified first in the liquid as dendrites. ~$RuAl_6$ then formed peritectically, coating the X-phase dendrites. The final liquid solidified eutectically, forming ~$RuAl_6$ and (Al).

In the 'fine' microstructure alloy, the primary phase is different to the primary phase in the coarse microstructure. ~Pt_5Al_{21} solidified from the liquid. The X phase coated the primary phase, indicating that it solidified peritectically. On the outside of the X, a phase is seen as small light specs, it is probably ~$RuAl_6$ that has formed peritectically. The final liquid solidified eutectically, forming (Al) and a small amount of ~$RuAl_6$.

From the phase and composition analyses of this alloy, the following solidification sequence is proposed

Coarse area

$L \rightarrow X$

$L + X \rightarrow \sim RuAl_6$

$L \rightarrow \sim RuAl_6 + (Al)$

Fine area

$L \rightarrow \sim Pt_5Al_{21}$

$L + \sim Pt_5Al_{21} \rightarrow X$

$L + X \rightarrow \sim RuAl_6$

$L \rightarrow \sim RuAl_6 + (Al)$

Not all the proposed reactions were observed in the solidification microstructure, as the phases were too fine to identify all of them accurately.

Since the last part of the proposed solidification sequences for the two microstructures are the same, that one part of the liquid was slightly enriched in Ru and depleted in Pt relative to the other part, if columnar type solidification is assumed, leading to different primary solidification. The composition difference might have been big enough for such a phenomenon and the EDS technique may not have been sensitive enough to pick up the real composition difference.

The phases were very finely dispersed and it was difficult to analyse the phases accurately with EDS. Unfortunately, in this sample, most of the proposed phases did not have prototypes suggested in the literature, which made confirmation by XRD difficult/impossible. The solidification for this alloy thus has some uncertainty associated with it.

4.2.2 PAR 2 - Al_{66}:Pt_{26}:Ru_6 alloy

The PAR 2 alloy was extremely brittle and broke into pieces while fastening in a vice to cut the button-melt sample in half. The sample was also very porous.

The BSE images in Figure 4.4 show a light dendritic phase in a dark matrix. In the light phase, another dendritic structure can be observed. This is not a continuous dendrite, as can be seen in Figure 4.4(b).

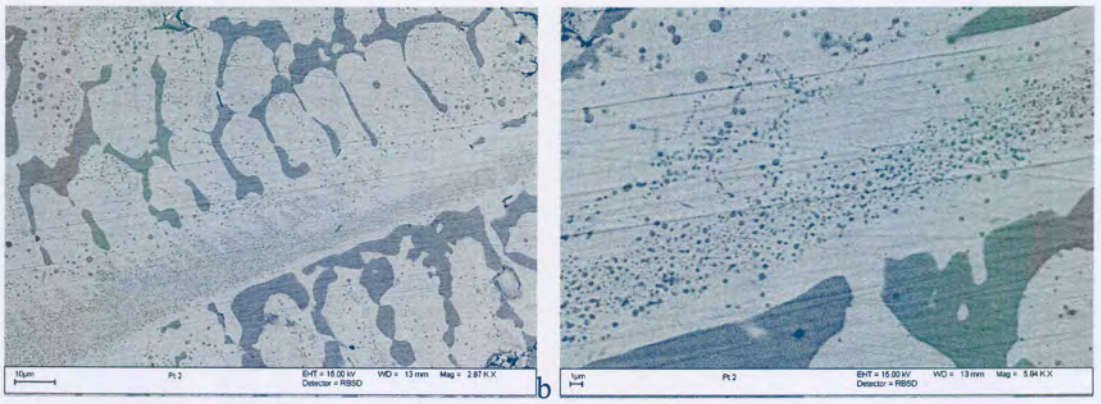

Figure 4.4. (a) shows the dendrite structure of PAR 2 and (b) shows the remnants of primary T in the light $PtAl_2$ dendrites.

Table 4.3 Summary of the phase and composition analyses for the PAR 2 alloy.

Sample	Condition	Phase Description	Composition			Proposed phase(s)	No of analyses
			Al	Pt	Ru		
PAR 2	Arc-melted	Overall	65.5 ± 0.5	26.9 ± 0.4	7.6 ± 0.4		5
		Light	61.5 ± 0.3	32.6 ± 0.3	5.9 ± 0.5	~$PtAl_2$	5
		Dark	70.5 ± 0.4	16.6 ± 0.2	12.9 ± 0.4	X	5
		Two phase (in light phase)	64.0 ± 0.3	28.2 ± 0.2	38.8 ± 0.3	T+~$PtAl_2$	5

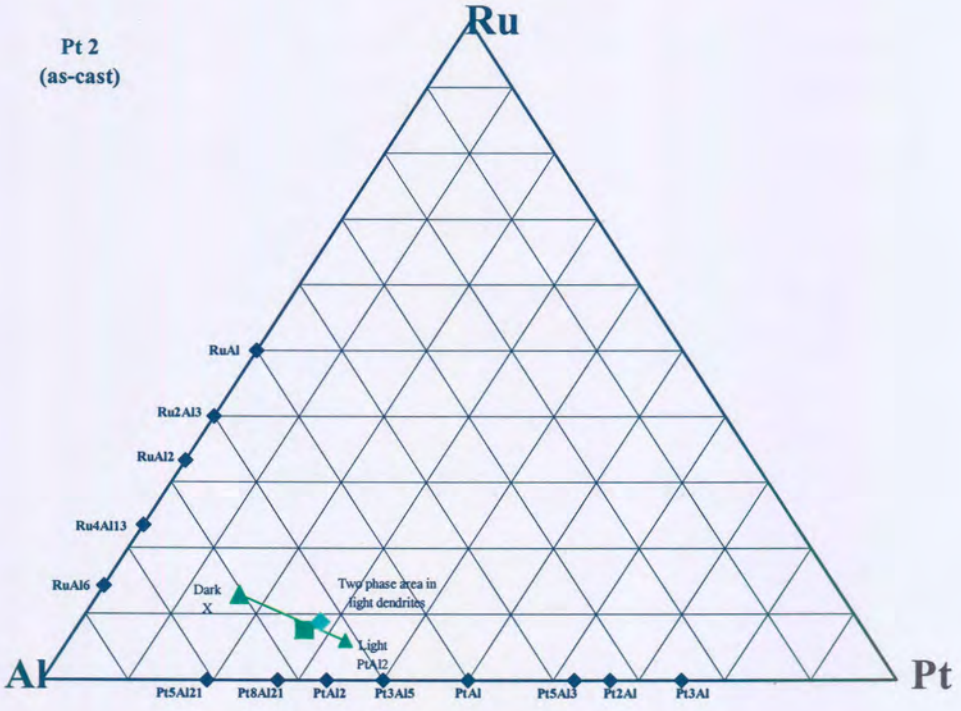

Figure 4.5. A ternary plot of the overall and phase compositions in the PAR 2 alloy.

The phase compositions determined by EDS analyses are listed in Table 4.3 and have been plotted on a ternary projection in Figure 4.5.

The PAR 2 alloy first solidified from the liquid by forming phase T dendrites. Phase T is a proposed new ternary phase of composition $Ru_{18}Pt_{28}Al_{64}$. The liquid then reacted peritectically with phase T to form $PtAl_2$. Most of the T was consumed in the peritectic reaction, leaving traces of phase T dendrites in the $PtAl_2$ dendrites. This is confirmed by EDS analysis, which found the composition of the two-phase area to be between the phase T composition and $PtAl_2$ composition (Figure 4.5 d). The last liquid transformed eutectically to $PtAl_2$ and phase X, a ternary phase stable at low temperatures.

The proposed solidification sequence can be summarised as follows:

$$L \rightarrow T$$
$$L + T \rightarrow \sim PtAl_2$$
$$L \rightarrow \sim PtAl_2 + X$$

Any remaining T decomposed

$$T \rightarrow X + \sim PtAl_2$$

4.2.3 PAR 3 - Al_{57}:Pt_{12}:Ru_{31} alloy

The PAR 3 alloy showed limited brittleness and little porosity.

The BSE images in Figure 4.6 show a dark grey dendritic phase in a light matrix. The dark grey dendrites are coated by a black phase. Between the dark grey dendrites and black phase, a fine two-phase area formed. On the outside of the black phase, another fine grey phase formed. A two-phase area also exists between the black and fine grey phase. Some of the grey phase is in the light matrix phase.

The phase compositions determined by EDS analyses are listed in Table 4.4 and have been plotted on a ternary projection in Figure 4.7.

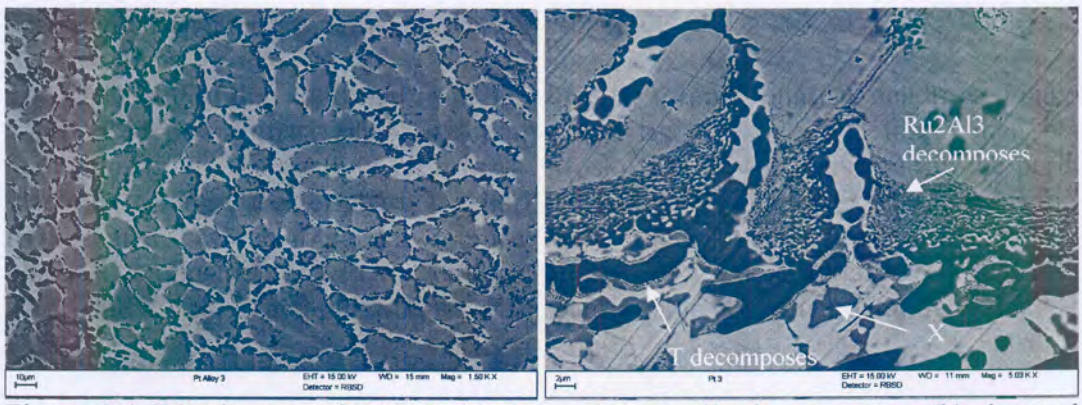

Figure 4.6. BSE images of PAR 3. (a) shows the overall microstructure. (b) shows the X phase as well as the two areas where Ru_2Al_3 and T decomposed.

Table 4.4. Summary of phase and composition analysis for the PAR 3 alloy.

Sample	Condition	Phase Description	Composition			Proposed phase(s)	No of analyses
			Al	Pt	Ru		
PAR 3	Arc-melted	Overall	65.5 ± 0.8	26.9 ± 0.9	7.6 ± 0.9		5
		Grey dendrites	49.4 ± 3	12.3 ± 1	38.3 ± 3.2	~RuAl	5
		Dark	63.2 ± 1.1	1.3 ± 0.5	36.6 ± 1.8	~$RuAl_2$	5
		Light	57.3 ± 1.3	31.1 ± 1	11.6 ± 1.9	~$PtAl_2$	5
		Darker Grey	69.6 ± 1.1	14.0 ± 1.4	16.4 ± 1.9	X	8

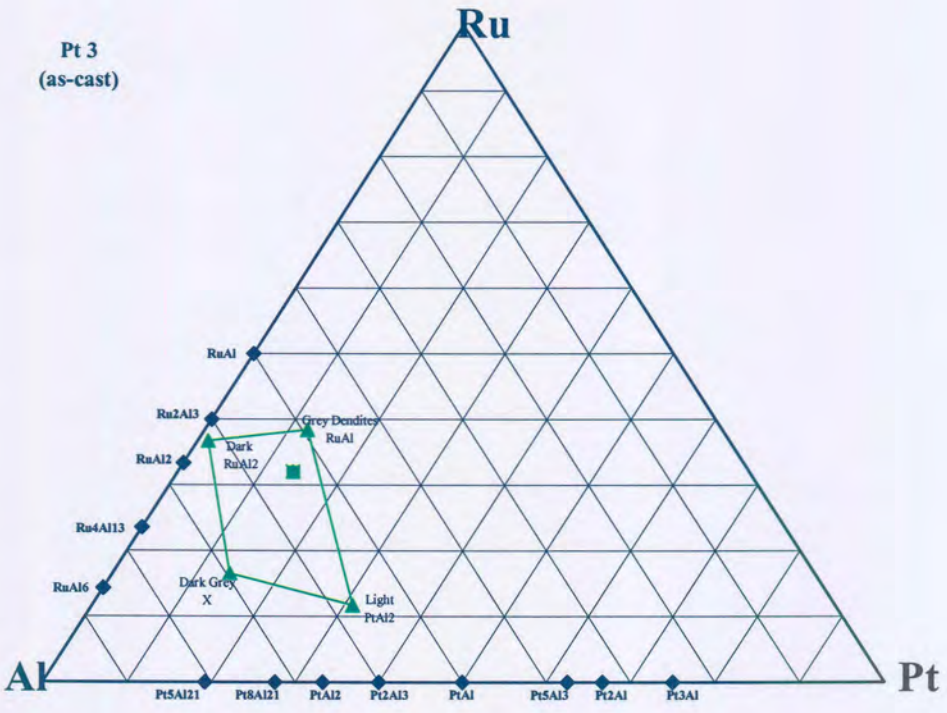

Figure 4.7 A ternary plot of the overall and phase compositions in the PAR 3 alloy.

The liquid first solidified as ~RuAl, the grey primary dendrite phase. Through a peritectic reaction, Ru_2Al_3 formed, coating the ~RuAl dendrites. The Ru_2Al_3 reacted with the liquid to form ~$RuAl_2$, the black phase. The solidification then proceeded in one of two ways: either the ~$RuAl_2$ reacted with the liquid to form X, which was consumed in a subsequent peritectic reaction between the liquid and X, or the ~$RuAl_2$ reacted with the liquid to form a ternary phase T, which coated the ~RuAl phase before it formed X, a ternary phase, through a peritectic reaction. Ru_2Al_3 decomposed through a solid-state reaction to ~RuAl and ~$RuAl_2$, thus explaining the dark 'messy' two-phase structure that coated the primary ~RuAl dendrites. The ternary phase T also decomposed at lower temperatures, which explained the fine structures between ~$RuAl_2$ and the ternary phase X.

The proposed solidification sequence can be summarised as follow:

$L \rightarrow \sim RuAl$
$L + \sim RuAl \rightarrow Ru_2Al_3$
$L + Ru_2Al_3 \rightarrow \sim RuAl_2$

The solidification probably progressed in one of two ways

$L + \sim RuAl_2 \rightarrow T$	OR	$L + \sim RuAl_2 \rightarrow X$
$L \rightarrow T + X$		$L + X \rightarrow \sim PtAl_2$

Ru_2Al_3 decomposed in the solid state:
$Ru_2Al_3 \rightarrow \sim RuAl + \sim RuAl_2$

4.2.4 PAR4 - Al_{54}:Pt_{38}:Ru_8 alloy

The PAR4 alloy showed some brittleness and the sample broke into four equal pieces when fastened in a vice for cutting.

The BSE images in Figure 4.8 show dark cored dendrites coated by a light phase in a medium matrix. The light coating phase is not continuous; a fine structure is present in it.

The phase compositions determined by EDS analyses are listed in Table 4.5 and have been plotted on a ternary projection in Figure 4.9.

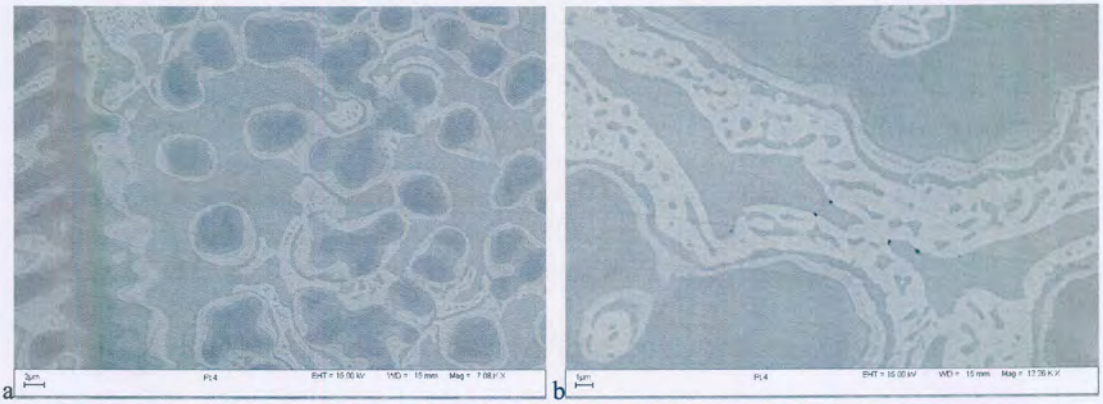

Figure 4.8. BSE images of PAR 4. (a) shows dark primary ~RuAl dendrites, coated by a PtAl layer (the light phase) in a Pt_2Al_3 matrix. (b) shows the detail of the PtAl coating layer.

Table 4.5. Summary of phase and composition analysis for the PAR4 alloy.

Sample	Condition	Phase Description	Composition			Proposed phase(s)	No of analyses
			Al	Pt	Ru		
PAR4	Arc-melted	Overall	51.6 ± 0.5	40.9 ± 3	7.6 ± 3.2		5
		Dark	45.3 ± 1.2	27.3 ± 1.4	27.4 ± 1.6	~RuAl	7
		Medium	55.2 ± 0.6	44.8 ± 0.6	0	Pt_2Al_3	6
		Light	47.4 ± 2	52.6 ± 2	0	PtAl	6

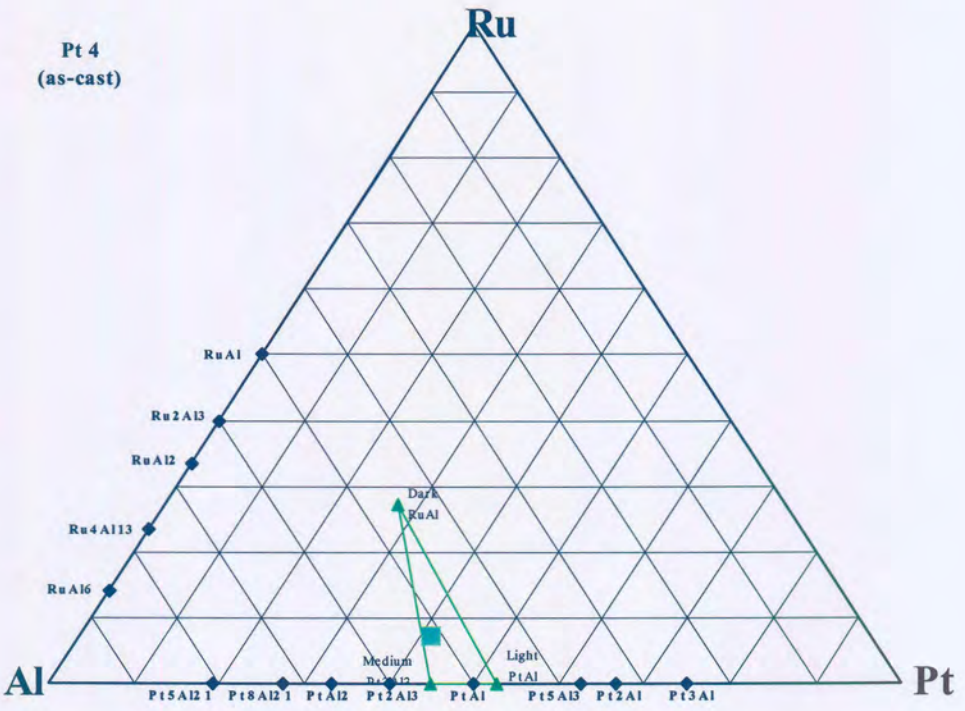

Figure 4.9. A ternary plot of the overall and phase compositions in the PAR 4 alloy.

The RuAl phase solidified as primary dendrites in the liquid. ~RuAl then reacted peritectically with the liquid to form PtAl, which coated the RuAl dendrites. PtAl reacted peritectically with the liquid to form Pt_2Al_3. The peritectic reaction changed to solidify the final liquid eutectically. The change in the reaction was probably due to a change in the relative stabilities of the phases with respect to each other. Since the final liquid was possibly depleted of Ru, the eutectic solidification of liquid proceeded according to the Al-Pt binary, where an eutectic reaction exists between PtAl and Pt_2Al_3.

The proposed solidification sequence is as follows:

$L \rightarrow \sim RuAl$
$L + \sim RuAl \rightarrow PtAl$
$L + PtAl \rightarrow \sim Pt_2Al_3$
which changed to
$L \rightarrow PtAl + \sim Pt_2Al_3$

(The peritectic reaction $L + \sim RuAl \rightarrow PtAl$ was found to be actually the eutectic reaction $L \rightarrow \sim RuAl + PtAl$ after studying a 600°C (4 weeks) heat-treated sample.)

The overall analysis of this sample is on the RuAl liquid surface, which indicates that RuAl phase stretches to ~10 at. % from the Al-Pt binary.

4.2.5 PAR5 - Al_{50}:Pt_{25}:Ru_{25} alloy

The PAR5 alloy was extremely brittle and it disintegrated into small pieces without a strong external force.

The BSE microstructure images in Figure 4.10 show a dark dendritic phase in a light matrix. The light matrix consists of two very fine light phases (Figure 4.10 b).

The phase compositions determined by EDS analyses are listed in Table 4.6 and have been plotted on a ternary projection in Figure 4.11.

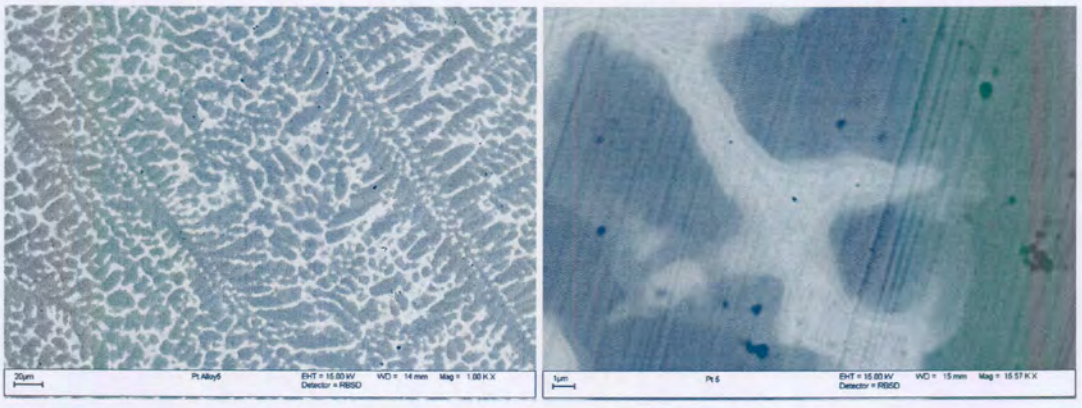

Figure 4.10. BSE image on the right showing dark ~RuAl dendrites in a light two-phase matrix. The light matrix consists of PtAl and Pt_5Al_3, which is the very light phase.

Table 4.6. Summary of phase and composition analysis for the PAR 5 alloy.

Sample	Condition	Phase Description	Composition			Proposed phase(s)	No of analyses
			Al	Pt	Ru		
PAR5	Arc-melted	Overall	43.6 ± 0.9	26.5 ± 0.8	29.9 ± 1.3		5
		Dark	45.0 ± 0.9	16.9 ± 0.4	38.1 ± 0.9	~RuAl	7
		Light	46.8 ± 0.9	51.6 ± 2.4	1.6 ± 2.3	PtAl + Pt_5Al_3	7
		Very Light	43.3±0.5	49.3±0.4	7.4±0.2		

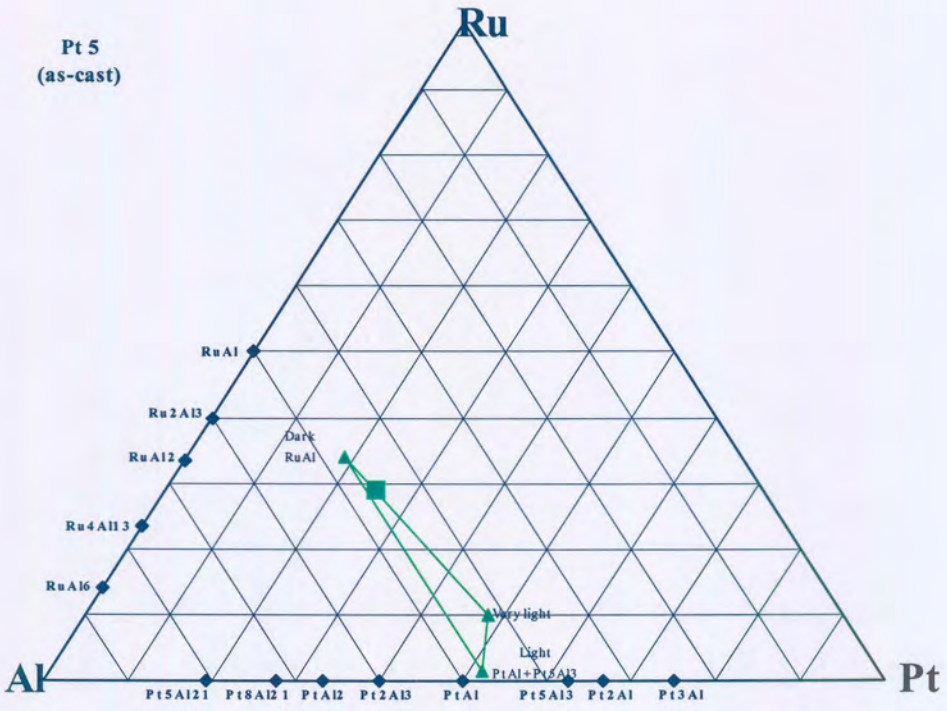

Figure 4.11. A ternary plot of the overall and phase compositions in the PAR 5 alloy.

The liquid solidified as primary ~RuAl dendrites, and showed some coring on the edges. The remainder of the liquid probably solidified as β phase, which decomposed in the solid state (below 1533 K) to two phases – PtAl and Pt_5Al_3. These two phases were too fine to analyse accurately individually.

The solidification can be summarised as follow:

$L \rightarrow \sim RuAl$

$L + \sim RuAl \rightarrow \beta$

β decomposed in the solid-state:

$\beta \rightarrow \sim PtAl + Pt_5Al_3$

4.2.6 PAR6 - Al_{25}:Pt_{55}:Ru_{20} alloy

The PAR6 alloy was the benchmarking alloy of this study, as it has the same composition as the lowest Pt-content sample of a series of Pt-Al-Ru alloys studied by Biggs [2001Big1]. The results are in good agreement. Unlike most of the other alloys, this alloy was ductile.

The BSE microstructure (Figure 4.12) shows big long dark needles in a light matrix, with some finer dark needles and irregular-shaped 'blobs' in the areas between the big long needles. The big long needles appear in a fan-like structure, and dissect through each other.

The phase compositions determined by EDS analyses are listed in Table 4.7 and have been plotted on a ternary projection in Figure 4.13.

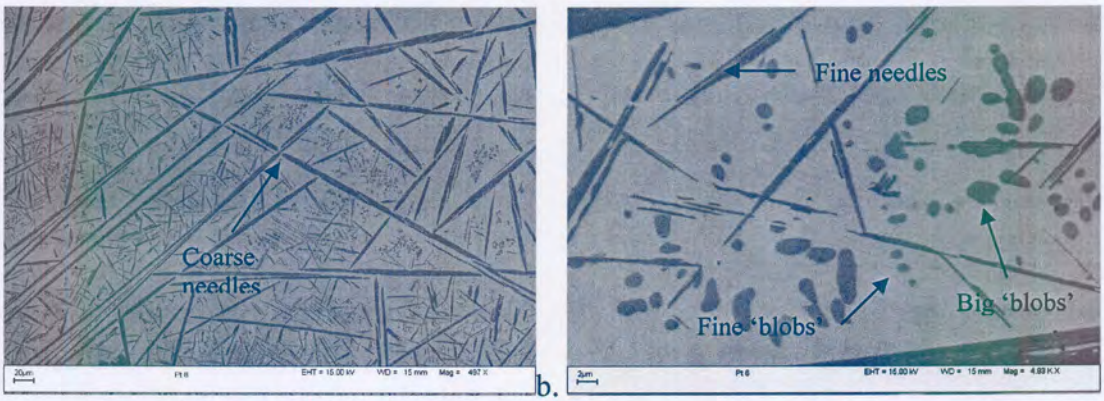

Figure 4.12. (a) The BSE image of PAR 6. (a) shows the long dark (Ru) needles in the light ~Pt_3Al matrix, with a finer dark phase present between the long needles. (b) shows that the fine (Pt) blob-like phase, and the finer (Ru) needles which formed in the ternary eutectic.

Table 4.7. Summary of phase and composition analysis for the PAR 6 alloy.

Sample	Condition	Phase Description	Composition			Proposed phase	No of analysis
			Al	Pt	Ru		
PAR6	Arc-melted	Overall	21.4 ± 0.7	51.7 ± 0.5	26.2 ±		5
		Light Matrix	28.6 ± 0.8	69.5 ± 0.8	1.9 ± 0.5	~Pt_3Al	7
		Dark needles (big and fine) and big blobs	1.8 ± 0.6	17.8 ± 1.1	80.4 ± 1.6	(Ru)	7
		Dark fine blobs	29.0 ± 1.2	68.7 ± 1.7	2.3 ± 1.1	(Pt)	7

Figure 4.13. A ternary plot of the overall and phase compositions in the PAR 6 alloy.

The PAR 6 alloy solidified by primary (Ru) needles growing in the liquid. The needles probably only thickened after their formation, since it appears as if they are pinched where they have grown through each other. This was probably followed by a eutectic reaction from the liquid, forming (Ru) and ~Pt_3Al, the light matrix. The binary eutectic was followed by a ternary eutectic, forming (Ru), ~Pt_3A and (Pt).

Coarser and finer needles appear in the microstructure. Both needles have a similar morphology. The big needles are primary (Ru), while the fine needles are (Ru) formed from the ternary eutectic reaction. The cross-section of the needles is irregular and appears 'blob'-like, with the larger 'blobs' corresponding to (Ru). The finer 'blobs' are (Pt) which formed in the ternary eutectic reaction. These are indicated in Figure 4.12 b.

The ternary eutectic has not been reported by Biggs [2001Big1].

The proposed solidification sequence can be summarised as:

$L \rightarrow (Ru)$

$L \rightarrow (Ru) + \sim Pt_3Al$

$L \rightarrow (Ru) + \sim Pt_3Al + (Pt)$

4.2.7 PAR7 - $Al_{73}:Pt_{22}:Ru_5$ alloy

The as-cast alloy was extremely brittle and broke into pieces even during repeated arc-melting to homogenise the sample. It could, therefore, only be partially melted together. The as-cast alloy was very porous, which made it difficult to prepare a smooth surface metallographically.

The BSE microstructure (Figure 4.14 a) shows light dendrites in a darker matrix. The dendrites are not homogeneous (Figure 4.14 b), another phase can be observed in the light dendrites.

The phase compositions determined by EDS analyses are listed in Table 4.8 and have been plotted on a ternary projection in Figure 4.15.

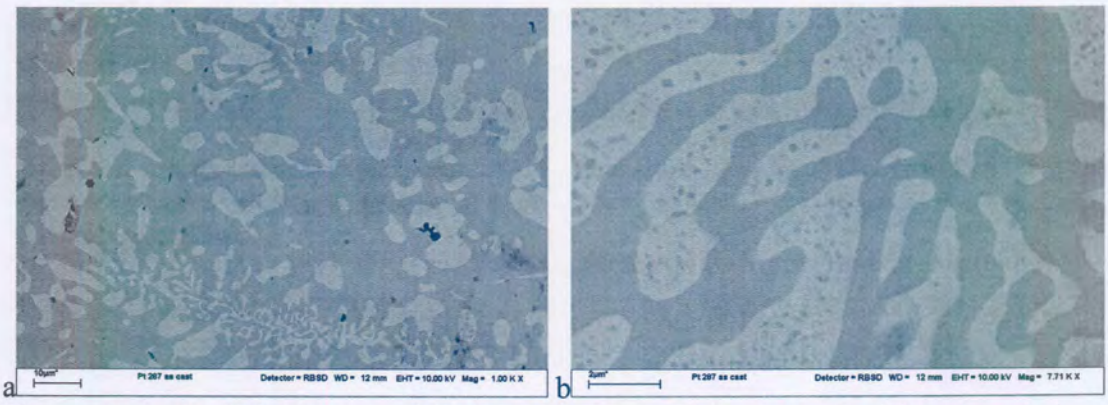

Figure 4.14. The BSE images of PAR 7. (a) shows white $PtAl_2$ dendrites in a darker X matrix. (b) shows precipitates of X in the $PtAl_2$ dendrites.

Table 4.8. Summary of phase and composition analysis for the PAR 7 alloy.

Sample	Condition	Phase Description	Composition			Proposed phase(s)	No of analyses
			Al	Pt	Ru		
PAR 7	Arc-melted	Overall	70.8 ± 0.4	21.6 ± 0.4	7.6 ± 0.6		5
		Light	67.9 ± 1	32.1 ± 1	0	$PtAl_2$	5
		Dark	72.1 ± 1.2	18.4 ± 1.2	9.5 ± 2.2	X	8

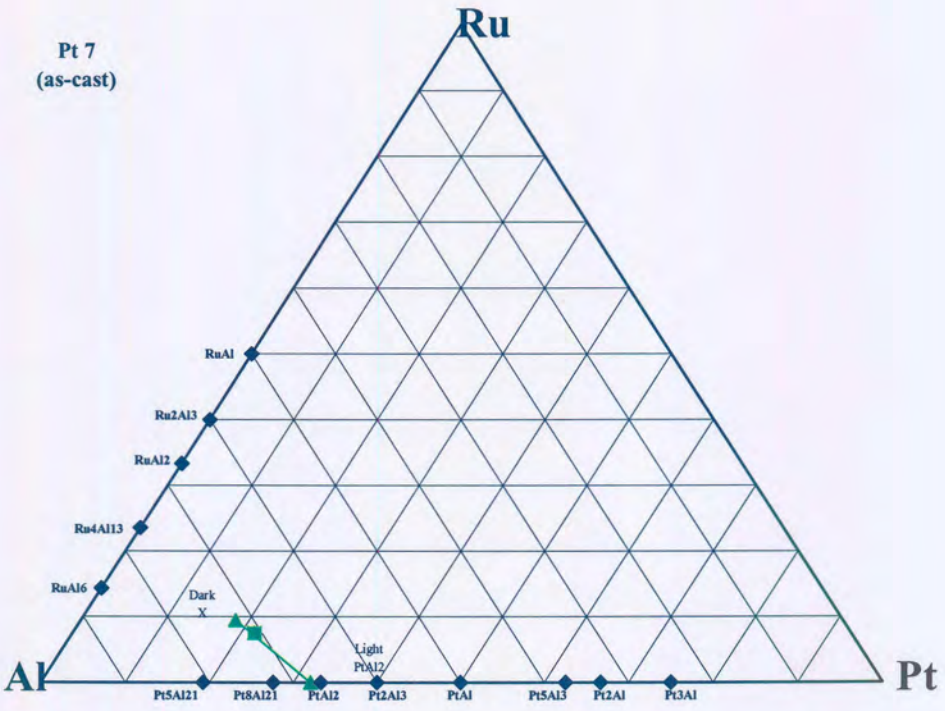

Figure 4.15. A ternary plot of the overall and phase compositions in the PAR 7 alloy.

The PAR 7 alloy solidified forming primary $PtAl_2$ dendrites in the liquid. The final volume of the liquid solidified eutectically, forming $PtAl_2$ and X. The fine phase present in the primary $PtAl_2$ dendrites are the X phase. This can either be due to the precipitation of the X phase because of a sloping solvus, or because the dendrites were probably wetted by the liquid, and small liquid 'pockets' remained in the dendrites, which then solidified as X phase.

The proposed solidification sequence is as follows:

$$L \rightarrow PtAl_2$$
$$L \rightarrow PtAl_2 + X$$

4.2.8 PAR 8 - Al_{71}:Pt_7:Ru_{22} alloy

The PAR 8 alloy was brittle and porous.

The BSE image (Figure 4.16 a) shows dark dendrites in a medium matrix. An irregular very light phase is present in the matrix(Figure 4.16 b).

The phase compositions determined by EDS analyses are listed in Table 4.9 and have been plotted on a ternary projection in Figure 4.17.

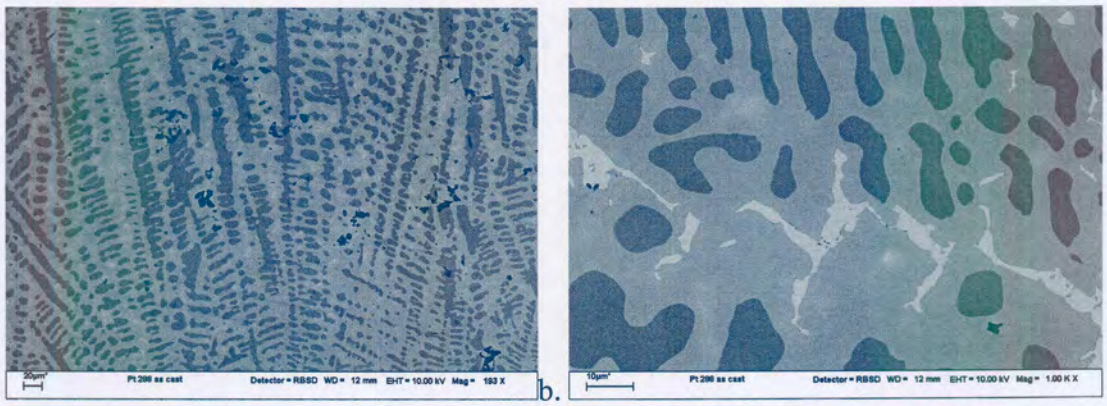

Figure 4.16. BSE images of PAR 8. (a) shows dark ~RuAl dendrites in a medium grey X phase. A very light phase ~$PtAl_2$ is present in the medium grey phase. (b) shows the microstructure in more detail.

Table 4.9. Summary of phase and composition analysis for the PAR 8 alloy.

Sample	Condition	Phase Description	Composition			Proposed phase(s)	No of analyses
			Al	Pt	Ru		
PAR 8	Arc-melted	Overall	62.0 ± 0.5	6.2 ± 0.4	31.8 ± 0.7		5
		Medium	67.0 ± 0.6	10.4 ± 0.3	22.6 ± 0.7	X	7
		Dark	56.2 ± 0.8	0	41.2 ± 0.8	~RuAl	7
		Very light	61.7 ± 1	30.4 ± 1.2	7.9 ± 1.1	~$PtAl_2$	7

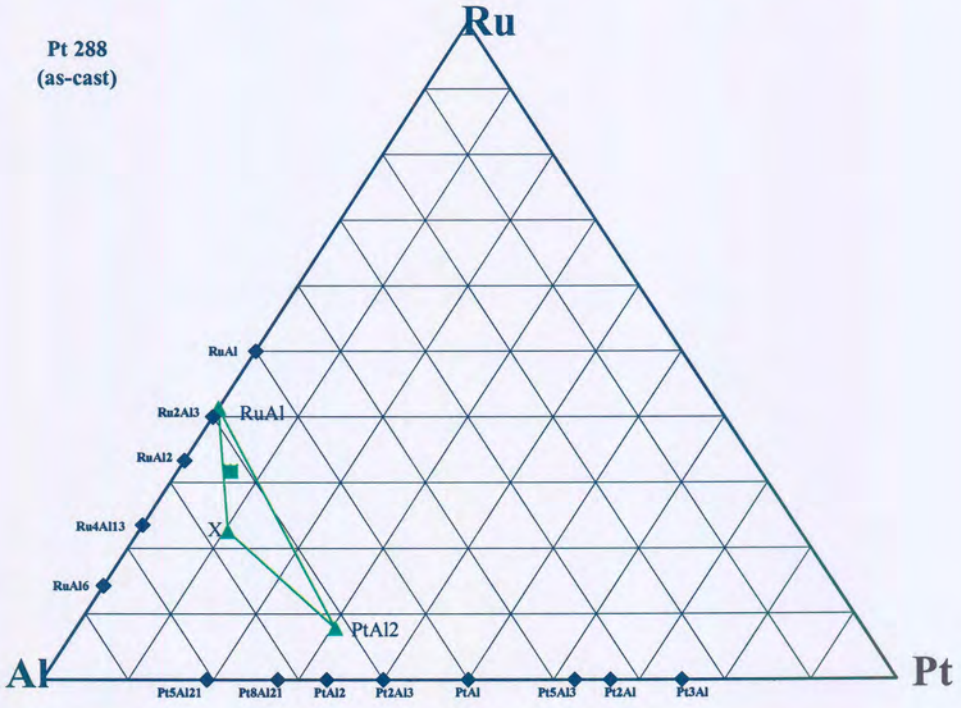

Figure 4.17. A ternary plot of the overall and phase compositions in the PAR 8 alloy.

Primary ~RuAl dendrites solidified from the liquid. The ~RuAl reacted peritectically with the liquid to form ~$RuAl_2$, which subsequently reacted with the liquid to form X, a ternary phase. The final liquid reacted with X to form ~$PtAl_2$, the white phase.

From the EDS analysis it seemed that the final peritectic reaction consumed all the ~$RuAl_2$ phase, as it was not detected.

The proposed solidification sequence is as follows:

$L \rightarrow$ ~RuAl
$L +$ ~RuAl $\rightarrow$ ~$RuAl_2$
$L +$ ~$RuAl_2 \rightarrow X$
$L + X \rightarrow$ ~$PtAl_2$

However, when comparing the proposed solidification sequence with the proposed liquidus surface projection, Ru_2Al_3 should have formed. It was thus assumed that a small amount Ru_2Al_3 did form, but that it was consumed in the subsequent peritectic reaction. The solidification sequence probably was as follows:

$L \rightarrow$ ~RuAl
$L +$ ~RuAl $\rightarrow Ru_2Al_3$
$L + Ru_2Al_3 \rightarrow$ ~$RuAl_2$
$L +$ ~$RuAl_2 \rightarrow X$
$L + X \rightarrow$ ~$PtAl_2$

4.2.9 PAR 9 - Al_{59}:Pt_{33}:Ru_8 alloy

The PAR 9 alloy was brittle.

Only two phases were observed in the BSE microstructure (Figure 4.18). The primary dendrite phase shows coring.

The phase compositions determined by EDS analyses are listed in Table 4.10 and have been plotted on a ternary projection in Figure 4.19.

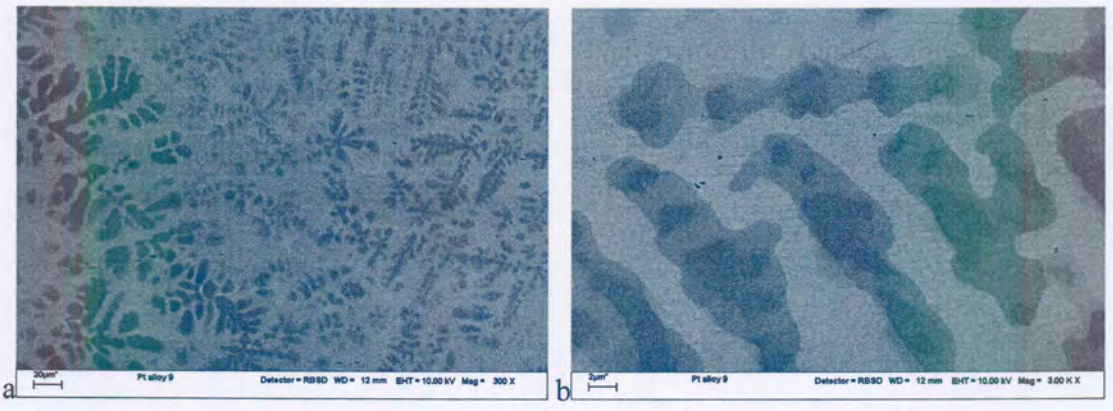

Figure 4.18. BSE microstructure of PAR 9. (a) shows the dendritic structure. (b) shows the coring of the dark grey ~RuAl phase.

Table 4.10. Summary of phase and composition analysis for the PAR 9 alloy.

Sample	Condition	Phase Description	Composition			Proposed phase(s)	No of analyses
			Al	Pt	Ru		
PAR9	Arc-melted	Overall	55.4 ± 1.2	32.5 ± 0.6	12.1 ± 1		5
		Light	60.4 ± 0.2	39.6 ± 0.2	0	Pt_2Al_3	6
		Dark	47.6 ± 0.7	20.6 ± 0.4	31.8 ± 0.9	~RuAl	5

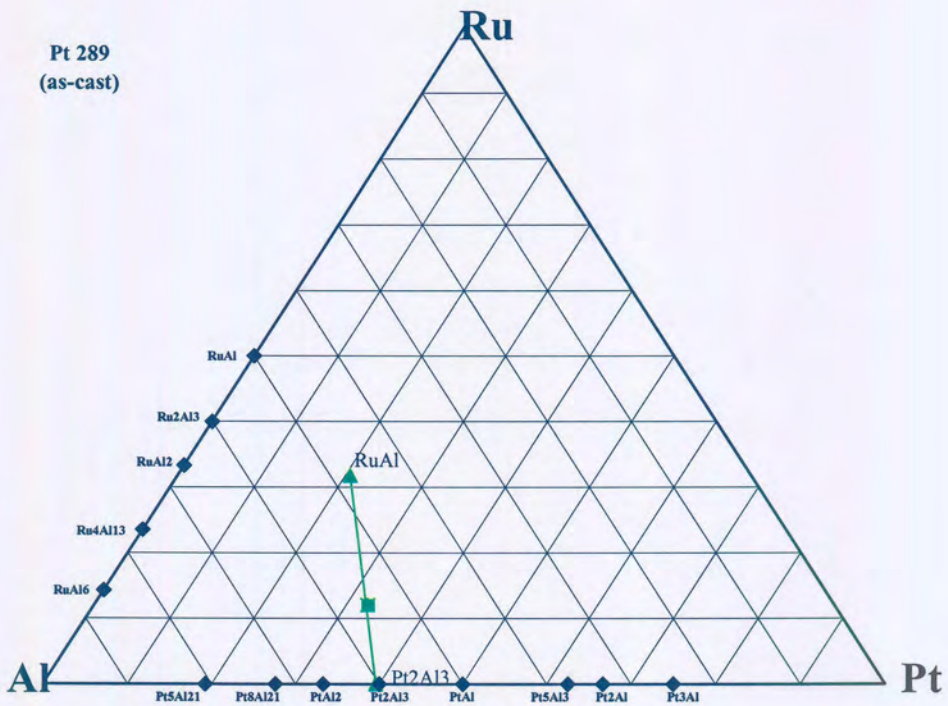

Figure 4.19. A ternary plot of the overall and phase compositions in the PAR 9 alloy.

The liquid solidified forming primary ~RuAl dendrites. The dendrites showed coring. The final liquid reacted peritectically with the liquid to form Pt_2Al_3.

The proposed solidification sequence is as follows:

$L \rightarrow$ ~RuAl

$L +$ ~RuAl $\rightarrow Pt_2Al_3$

4.2.10 PAR10 - Al_{34}:Pt_{40}:Ru_{26} alloy

The PAR 10 alloy was ductile.

The low magnification BSE image of the as-cast microstructure (Figure 4.20 a) shows long, directional dark 'feather-like' dendrites in a light matrix. In some areas it looked as if there were 'blotches' clouding the clear dendrite image. In these blotchy areas the dark dendrites were coated with a lighter phase as can be seen in Figure 4.20 (b). In the areas between the dendrites a fine 'eutectic' structure was observed.

The phase compositions determined by EDS analyses are listed in Table 4.11 and have been plotted on a ternary projection in Figure 4.21.

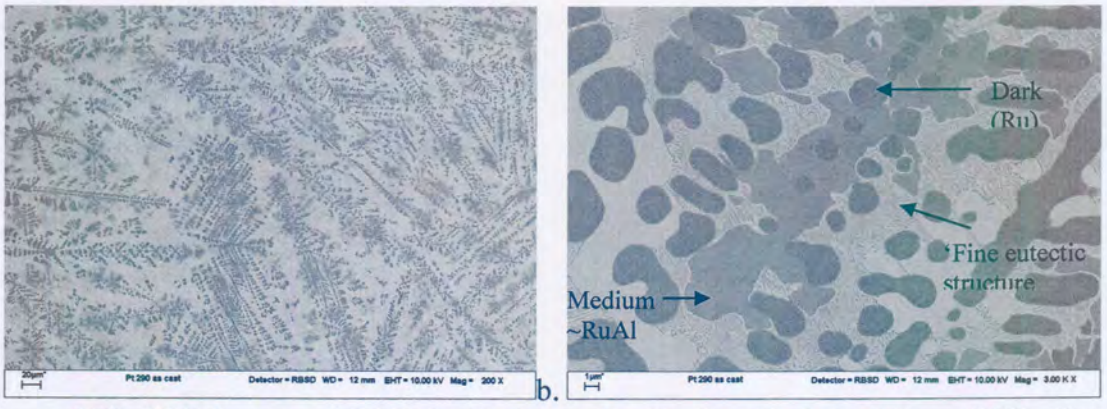

Figure 4.20. BSE images of PAR10. (a) shows the 'feather-like' dendrite solidification structure, with some areas which appear 'cloudy'. In the close up, (b), the dark (Ru) needles, coated by a medium phase, ~RuAl in a light (Pt_5Al_3 + PtAl) matrix. Between the dendrites, a fine eutectic structure is visible.

Table 4.11. Summary of phase and composition analysis for the PAR 10 alloy.

Sample	Condition	Phase Description	Composition			Proposed phase(s)	No of analyses
			Al	Pt	Ru		
PAR 10	Arc-melted	Overall	28.0 ± 0.6	32.6 ± 0.5	39.5 ± 1		5
		Light matrix	40.5 ± 3.6	59.5 ± 3.6	0	(PtAl + Pt_5Al_3)	3
		Dark	3.4 ± 0.3	3.4 ± 0.3	93.3 ± 0.6	(Ru)	11
		Medium	42.3 ± 0.7	21.3 ± 0.6	36.4 ± 0.8	~RuAl	5

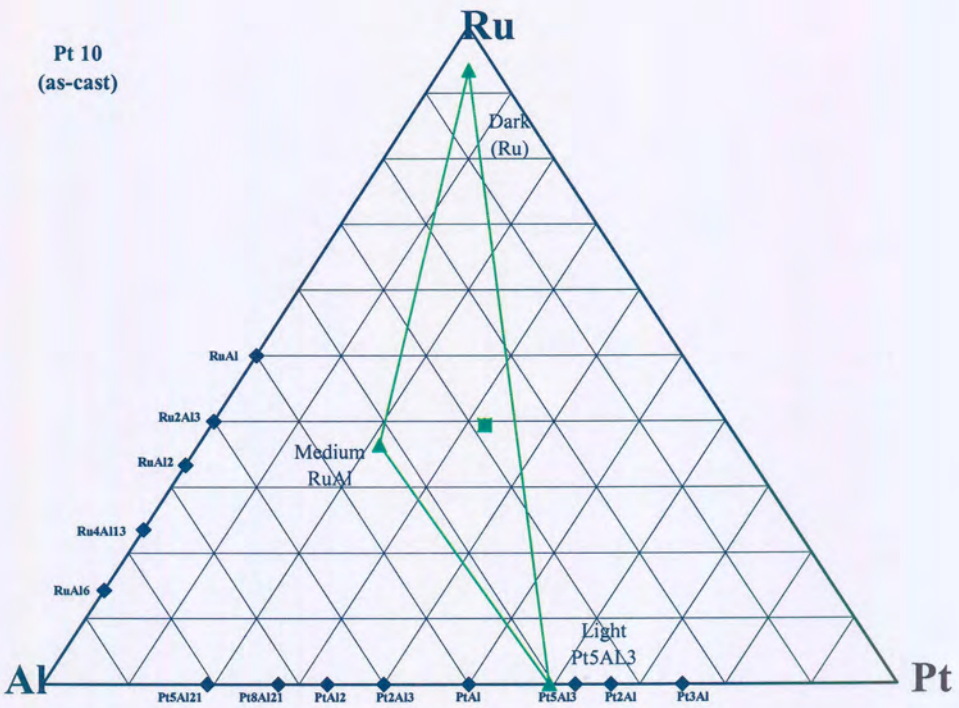

Figure 4.21 A ternary plot of the overall and phase compositions in the PAR 10 alloy.

(Ru) solidified as the primary phase with needles growing in the liquid, before it reacted with the liquid to form ~RuAl. The ~RuAl reacted with the remaining liquid to form β. The reaction transformed to a eutectic reaction due to more favourable thermodynamic conditions. β decomposed in the solid state to Pt_5Al_3 and PtAl, as it is unstable below 1533 K. More Pt_5Al_3 than PtAl was observed, as the composition was far to the platinum side of the β phase.

The proposed solidification sequence is as follows:

$L \rightarrow (Ru)$

$L + (Ru) \rightarrow \sim RuAl$

$L + RuAl \rightarrow \beta$

which changed to $L \rightarrow RuAl + \beta$

β decomposed by solid state reaction:

$\beta \rightarrow Pt_5Al_3 + PtAl$

4.2.11 PAR 11 - Al_{42}:Pt_{52}:Ru_6 alloy

PAR11 did not show any brittleness.

The BSE microstructure (Figure 4.22) shows a dark dendrite, coated by a lighter phase, in a light matrix. At a higher magnification (Figure 4.22 b), both the dark and medium phases show the presence of another phase, very finely dispersed, in it.

The phase compositions determined by EDS analyses are listed in Table 4.12 and have been plotted on a ternary projection in Figure 4.23.

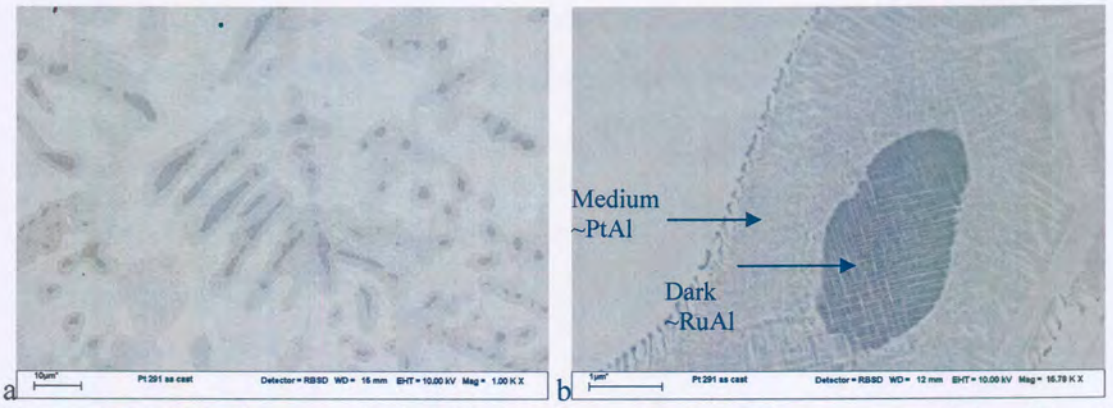

a b

Figure 4.22. BSE images of PAR 11. (a) shows the dendritic structure of the alloy. (b) clearly shows the presence of a fine phase in the dark dendrite phase as well as the area surrounding the dark dendrite.

Table 4.12. Summary of phase and composition analysis for the PAR 11 alloy.

Sample	Condition	Phase Description	Composition			Proposed phase(s)	No of analyses
			Al	Pt	Ru		
PAR 11	Arc-melted	Overall	39.7 ± 0.8	50.1 ± 0.9	10.2 ± 1.1		9
		Light matrix	37.6 ± 0.4	62.4 ± 0.4	0	Pt_5Al_3	4
		Dark *	42.4 ± 0.7	23.5 ± 0.8	34.1 ± 0.9	~RuAl	7
		Medium *	49.9 ± 0.9	44.4 ± 3.3	12.6 ± 2.8	~PtAl	7

* bulk phase composition, as a finely dispersed second phase is present in the bulk phase, the fine phase was too fine to analyse with EDS.

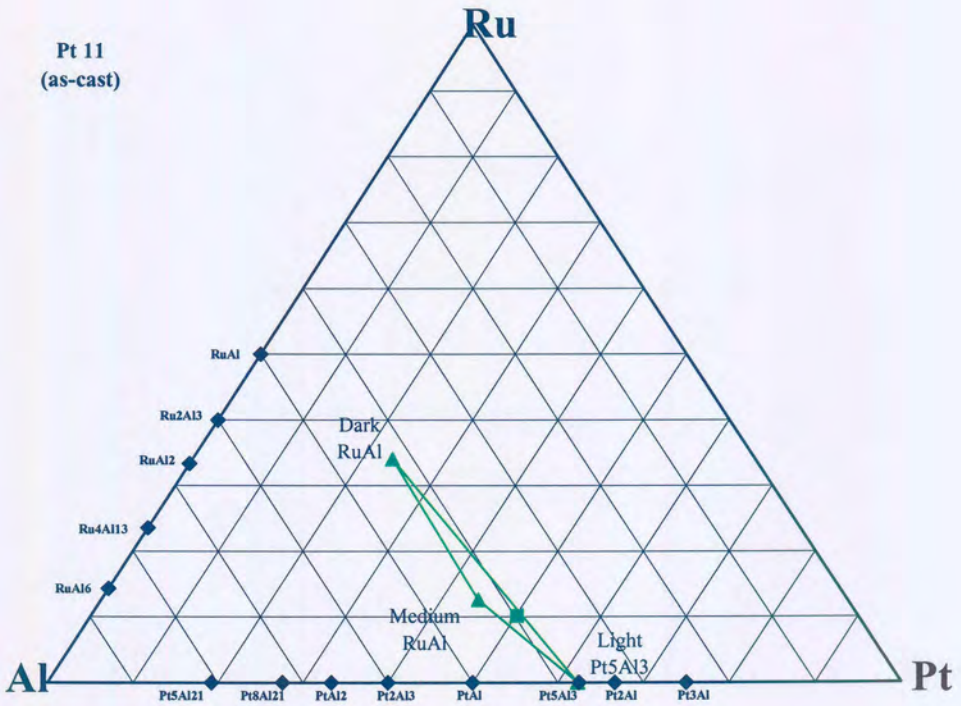

Figure 4.23. A ternary plot of the overall and phase compositions in the PAR 11 alloy.

The liquid solidified as primary ~RuAl dendrites (these dark dendrites were very fine and their size on the limit of the spatial resolution of EDS). The dendrites were coated with β phase when the liquid reacted peritectically with the ~RuAl to form β. The final of the liquid then solidified as Pt_5Al_3 through a peritectic reaction between the liquid and β. The β-phase decomposed at lower temperatures to Pt_5Al_3 and PtAl.

There is also a fine phase present in the dark ~RuAl dendrites. Although it was too fine to analyse accurately with EDS, it is proposed that it is Pt_5Al_3. It probably appeared in the ~RuAl phase due to a solid-state precipitation of Pt_5Al_3 because of a sloping solvus.

The proposed solidification sequence is:

$L \rightarrow$ ~RuAl

$L +$ ~RuAl $\rightarrow \beta$

$L + \beta \rightarrow Pt_5Al_3$

A solid-state transformation is observed after the solidification:

$\beta \rightarrow Pt_5Al_3 + PtAl$

4.2.12 PAR 12 - Al_{33}:Pt_{59}:Ru_8 alloy

PAR 12 was a small and dense button-melt sample. It was ductile, but showed some porosity in the microstructure.

The BSE images (Figure 4.24) show fine dark primary needles formed in a light matrix. The microstructure appeared similar to the PAR 6, but the needles in PAR 12 were finer and also did not show the distinct fan-like structure of PAR 6. Where the sample preparation has cut through a needle, it showed that these were thin flat needles (Figure 4.24 b), and not round and blob-like as the needles in PAR 6.

The phase compositions determined by EDS analyses are listed in Table 4.13 and have been plotted on a ternary projection in Figure 4.25.

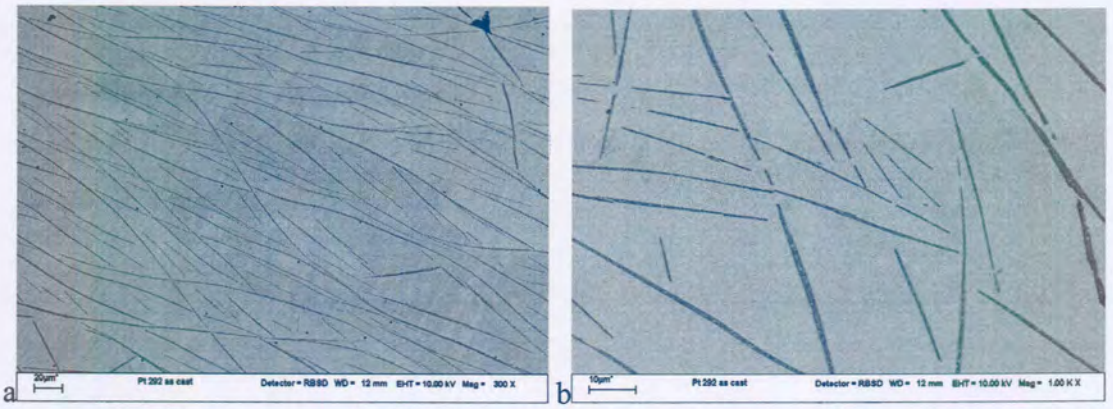

Figure 4.24. BSE images of PAR 12. (a) shows long thin and small fine (Ru) needles in a light Pt_3Al matrix. (b) shows the microstructure at a higher magnification.

Table 4.13. Summary of phase and composition analysis for the PAR 12 alloy.

Sample	Condition	Phase Description	Composition			Proposed phase(s)	No of analyses
			Al	Pt	Ru		
PAR12	Arc-melted	Overall	29.9 ± 0.6	54.3 ± 0.7	15.8 ± 0.6		5
		Light matrix	34.9 ± 0.4	65.1 ± 0.4	0	Pt_3Al	9
		Dark needles	0	10.2 ± 2.3	89.8 ± 2.3	(Ru)	7

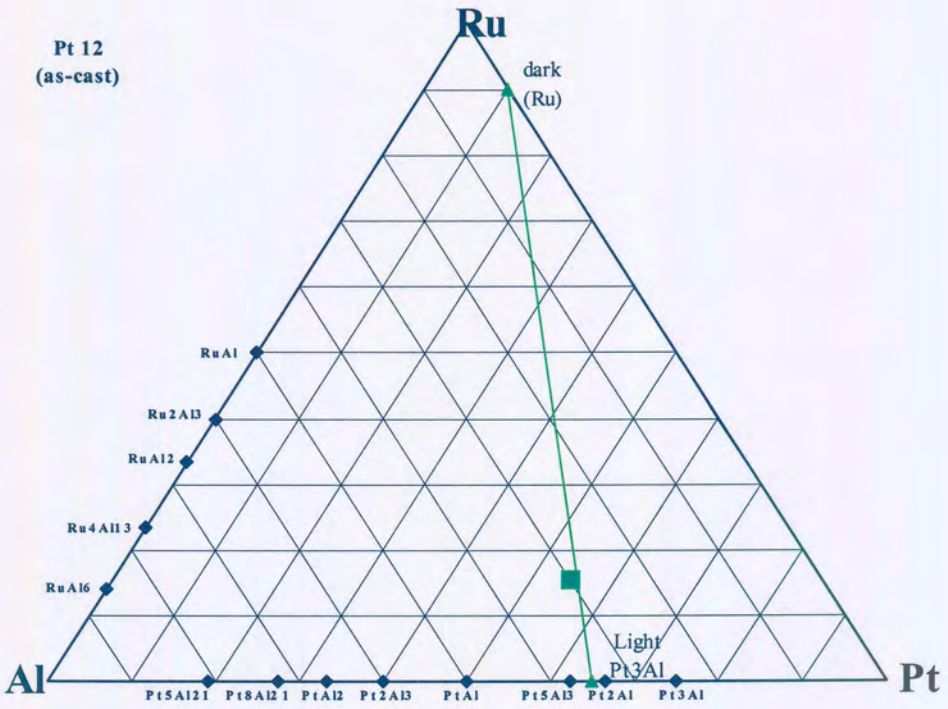

Figure 4.25. A ternary plot of the overall and phase compositions in the PAR 12 alloy.

Fine dark primary (Ru) needles formed from the liquid, before reacting with the liquid to form Pt_3Al by a peritectic reaction. The needles were finer than the ones observed in the as-cast PAR6 alloy, and also did not show the distinct fan-like structure of the PAR6 needles.

The proposed solidification sequence is as follows:

$L \rightarrow (Ru)$

$L + (Ru) \rightarrow Pt_3Al$

4.2.13 The PAR 13- Al_{85}:Pt_{10}:Ru_5 alloy

The alloy was brittle and cracked easily.

The BSE microstructure (Figure 4.26 a and b) shows light primary dendrites in a dark matrix. On the edge of the dendrites a fine lighter phase is observed (Figure 4.24 c), which formed peritectically. Between the dendrites, an eutectic structure formed (Figure 4.24 d).

The phase compositions determined by EDS analyses are listed in Table 4.14 and have been plotted on a ternary projection in Figure 4.25.

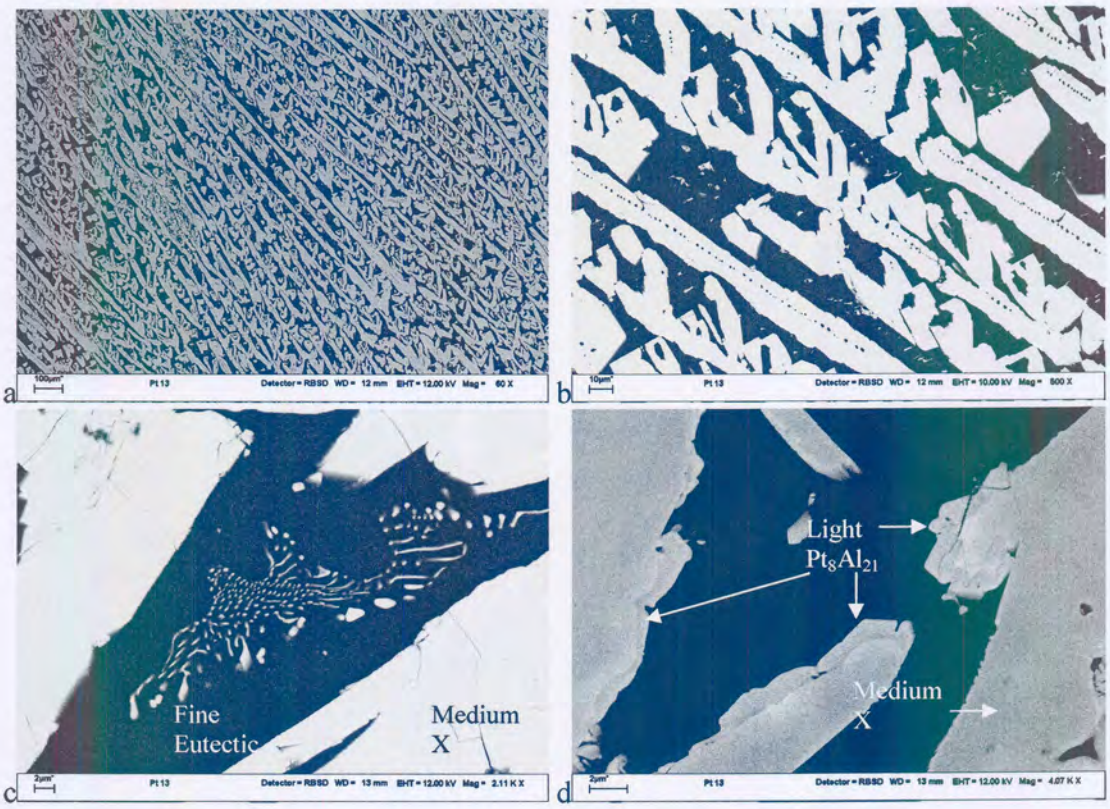

Figure 4.26. BSE images of PAR 13. (a) and (b) show the general microstructure. In (c) the ternary eutectic structure between the primary X dendrites can be seen. (d) shows the presence of another phase (lighter than dendrites) on the edges of the X dendrites.

Table 4.14. Summary of phase and composition analysis for the PAR 13 alloy.

Sample	Condition	Phase Description	Composition			Proposed phase(s)	No of analyses
			Al	Pt	Ru		
PAR13	Arc-melted	Overall	87.6 ± 0.4	8.5 ± 0.4	4.0 ± 0.4		5
		Medium	73.4 ±0.4	17.1 ± 0.8	9.5 ± 0.7	X	5
		Light	76.8 ± 0.7	24.2 ± 0.8	0	Pt_8Al_{21}	5
		Dark	100	0	0	(Al)	5

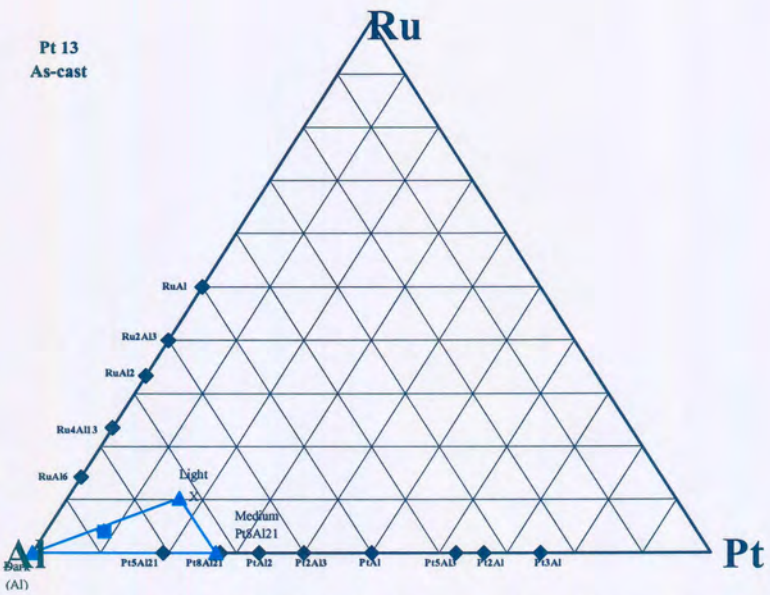

Figure 4.27 A ternary plot of the overall and phase compositions in the PAR 13 alloy.

The microstructure shows light primary X facetted crystals in a dark (Al) matrix. On the edge of the crystals, Pt_8Al_{21}, formed peritectically. The final liquid solidified eutectically, forming Pt_5Al_{21} and (Al).

The proposed solidification sequence is:

$$L \rightarrow X$$
$$L + X \rightarrow Pt_8Al_{21}$$
$$L \rightarrow Pt_5Al_{21} + (Al)$$

Another reaction probably occurred between the last two reactions, as there should be continuity of the phases between the different steps of the proposed solidification sequence. However, it has not been observed.

4.2.14 The PAR14- Al_{66}:Pt_{13}:Ru_{21} alloy

The sample was brittle and fractured easily.

The BSE microstructure reveals three distinct phases (Figure 4.28). Dark dendrites are coated by a medium phase in a light matrix.

The phase compositions determined by EDS analyses are listed in Table 4.15 and have been plotted on a ternary projection in Figure 4.29.

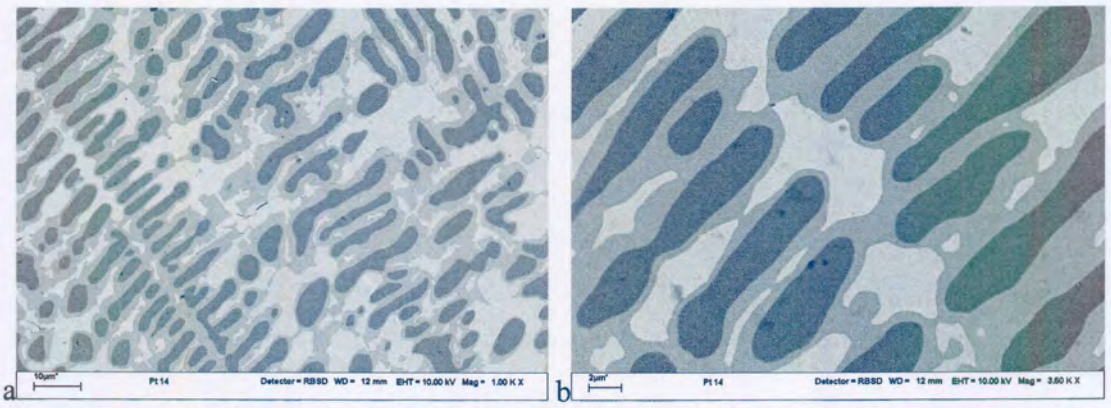

Figure 4.28. BSE images of PAR 14. (a) shows the dark $RuAl_2$ dendrites surrounded by a medium X phase in a light ~$PtAl_2$ matrix. (b) shows a higher magnification of the microstructure.

Table 4.15. Summary of phase and composition analysis for the PAR 14 alloy.

Sample	Condition	Phase Description	Composition			Proposed phase(s)	No of analyses
			Al	Pt	Ru		
PAR14	Arc-melted	Overall	64.0 ± 0.4	13.6 ± 0.4	22.4 ± 0.2		5
		Light	57.8 ± 0.6	32.4 ± 1.1	9.8 ± 0.9	~$PtAl_2$	7
		Medium	69.7 ± 0.5	13.9 ± 0.7	16.4 ± 1.0	X	7
		Dark	63.9 ± 0.5	0	36.1 ± 0.5	$RuAl_2$	7

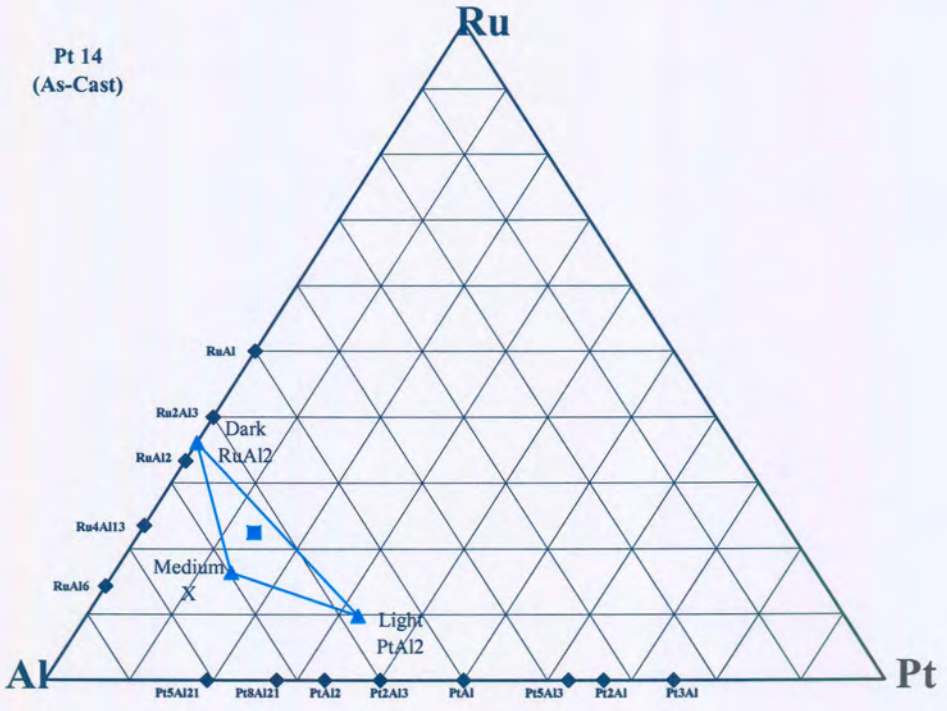

Figure 4.29. A ternary plot of the overall and phase compositions in the PAR 14 alloy.

The primary dendrites of $RuAl_2$ formed in the liquid. The liquid then reacted with the $RuAl_2$ peritectically and formed X, which coated the primary dendrites. This was followed by another peritectic reaction where ~$PtAl_2$ formed from the liquid and X

.

The proposed solidification sequence is:

$$L \rightarrow RuAl_2$$
$$L + RuAl_2 \rightarrow X$$
$$L + X \rightarrow \sim PtAl_2$$

4.2.15 The PAR 15- Al_{47}:Pt_{51}:Ru_2 alloy

The PAR 15 alloy did not show any brittleness.

The BSE images show 'island', with a two-phase structure in them, in a matrix that also shows a finer structure (Figures 4.30 a and b). The two fine phases differ in appearance (Figures 4.30 c and d).

The phase compositions determined by EDS analyses are listed in Table 4.16 and have been plotted on a ternary projection in Figure 4.31.

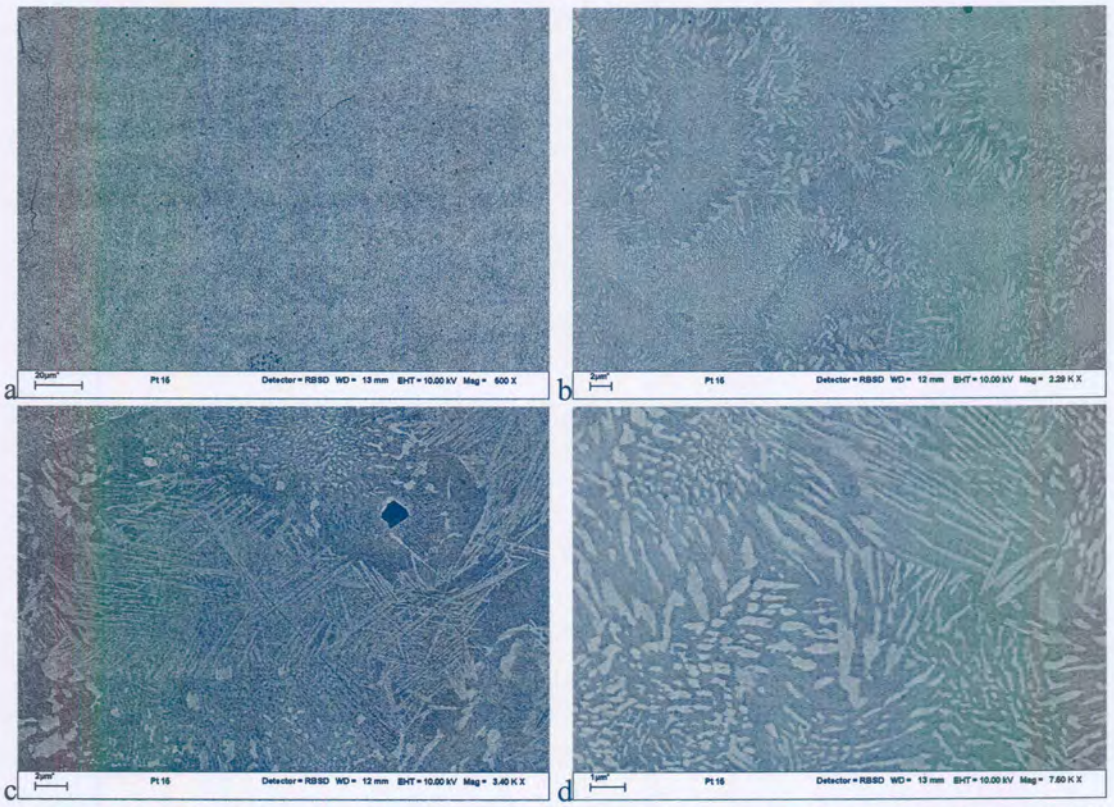

Figure 4.30. (a) shows the overall microstructure of PAR 15. (b) shows the 'grain'-like structure. (c) shows the solid state decomposition of a primary β grain while (d) shows the difference in decomposition microstructures.

Table 4.16. Summary of phase and composition analysis for the PAR 15 alloy.

Sample	Condition	Phase Description	Composition			Proposed phase(s)	No of analyses
			Al	Pt	Ru		
PAR15	Arc-melted	Overall	42.0 ± 0.3	55.7 ± 0.8	2.3 ± 0.7		5
		Light	35.0 ± 0.4	61.9 ± 0.6	3.1 ± 0.5	~Pt_5Al_3	5
		Dark	45.2 ± 0.2	52.1 ± 0.7	2.7 ± 0.6	~PtAl	5

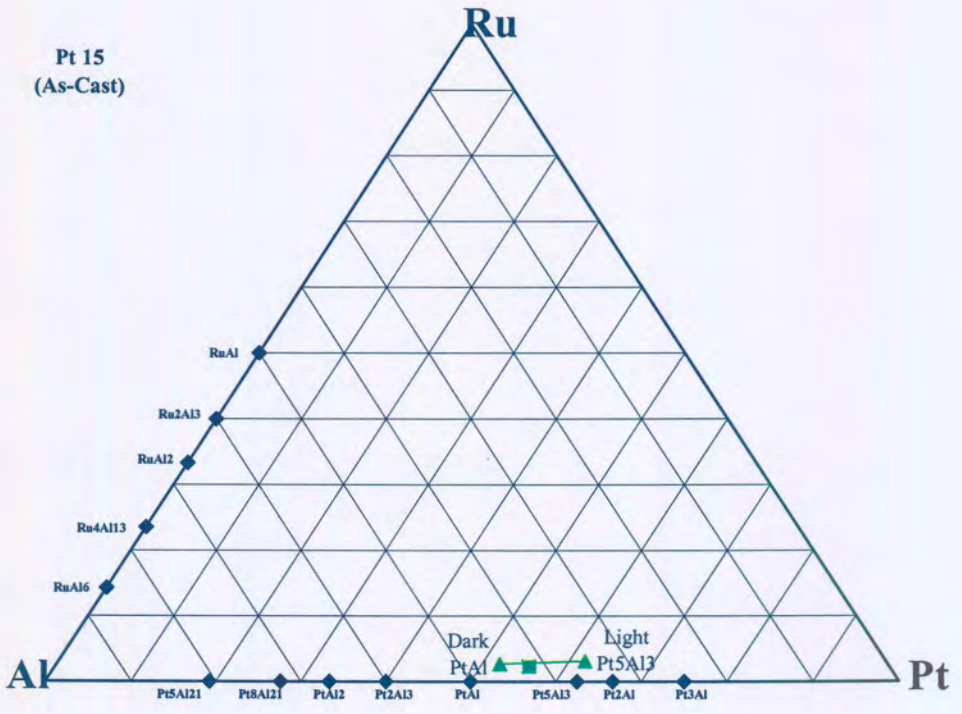

Figure 4.31. A ternary plot of the overall and phase compositions in the PAR 15 alloy.

Primary discrete β phase 'islands' formed in the liquid. The reaction then changed to a eutectic reaction where β and ~Pt_5Al_3 formed from the liquid. The β phase decomposed below 1533 K to ~PtAl and ~Pt_5Al_3. Inside the 'islands' it was only β phase decomposing; in the matrix as ~Pt_5Al_3 was already present before the β decomposed, resulting in two different microstructures of ~PtAl and ~Pt_5Al_3 in the primary 'islands' and in the eutectic mixture. This is illustrated schematically in Figure 4.32.

The proposed solidification sequence is:

$L \rightarrow \beta'$

$L \rightarrow \beta'' + \sim Pt_5Al_3$

(β' is the primary β phase which formed form the liquid, β'' is the eutectically formed β phase)

The β phase then decomposes

$$\beta \rightarrow \sim PtAl + \sim Pt_5Al_3$$

The development of the solidification microstructure is illustrated in Figure 4.32. Primary β particles forms from the liquid (showed as β'). The remainder of the liquid solidifies eutectically, leaving the β' in a β'' and $\sim Pt_5Al_3$ matrix. The β phase then decomposes to ~PtAl and $\sim Pt_5Al_3$, as described above.

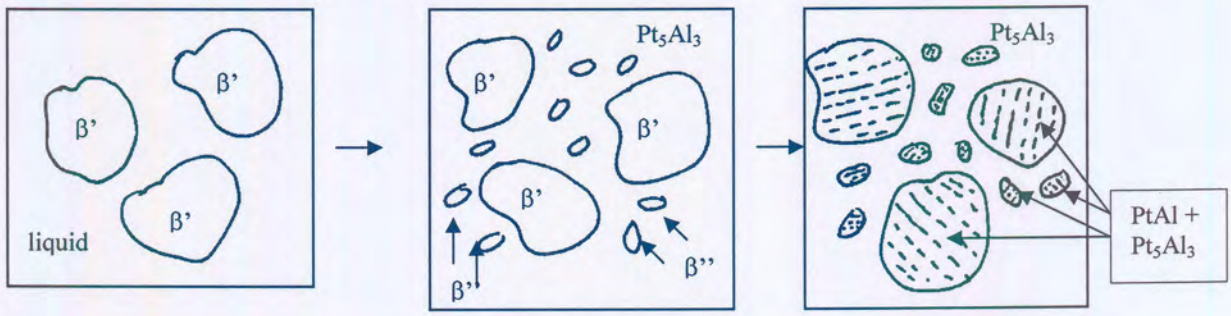

Figure 4.32. Schematic development of the solidification microstructure of the PAR15 alloy.

4.2.16 The PAR 16- $Al_{74}:Pt_8:Ru_{18}$ alloy

The PAR 16 alloy was very brittle. Some porosity was visible.

The BSE microstructures (Figures 4.33) show a medium grey dendrite phase that is coated by a black phase. The coated dendrites are surrounded by a light grey phase, which shows some coring. Finally there are small particles of a very light phase present in a light cored area.

a.

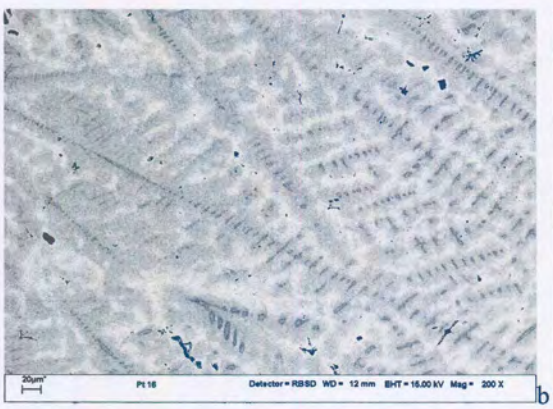

b

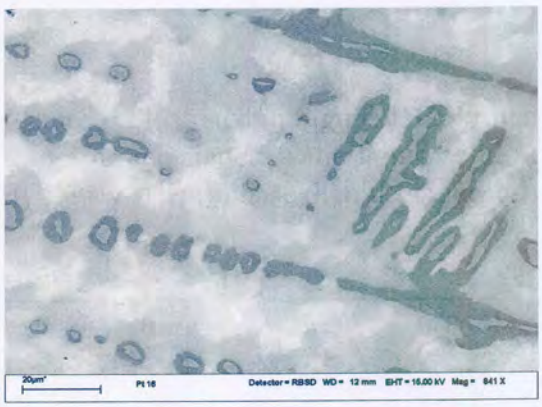

Figure 4.33. (a) shows the overall microstructure of PAR 16. (b) shows the medium primary $RuAl_2$ dendrites coated by the black Ru_4Al_{13} phase. Small, very light areas of $PtAl_2$ can be seen in the cored X phase.

The phase compositions determined by EDS analyses are listed in Table 4.17 and have been plotted on a ternary projection in Figure 4.34.

Table 4.17. Summary of phase and composition analysis for the PAR 16 alloy.

Sample	Condition	Phase Description	Composition			Proposed phase(s)	No of analyses
			Al	Pt	Ru		
PAR16	Arc-melted	Overall	71.9 ± 0.4	8.9 ± 0.3	19.2 ± 0.3		5
		Medium Grey (dendrite core)	63.9 ± 0.3	0.5 ± 0.2	35.6 ± 0.3	$RuAl_2$	5
		Dark	75.3 ± 0.2	0.5 ± 0.2	25.2 ± 0.2	Ru_4Al_{13}	5
		Cored phase	71.5 ± 1.6	15.2 ± 1.3	13.3 ± 2.5	X	5
		Very light	65.4 ± 0.9	34.6 ± 0.9	0	$PtAl_2$	5

Figure 4.34. A ternary plot of the overall and phase compositions in the PAR 16 alloy.

Primary $RuAl_2$ dendrites formed in the liquid. Through a cascade of peritectic reactions, the primary dendrites were coated by Ru_4Al_{13}, then by a very cored X phase and finally by $PtAl_2$.

The proposed solidification sequence is:

$L \rightarrow RuAl_2$
$L + RuAl_2 \rightarrow Ru_4Al_{13}$
$L + Ru_4Al_{13} \rightarrow X$
$L + X \rightarrow PtAl_2$

4.3 XRD results

The initial attempt to identify and confirm the phases suggested by the EDS analyses proved to be no simple task. This was due to the fact that only some of the binary phases are included in the ICDD [2002ICD] and ICSD [2002ICS], which contain the standard diffraction data for phases. The diffraction data are normally only for the pure phases and solid solution phases are not considered. Furthermore, when there is third element solid solubility of an element in a binary phase, the diffraction patterns shifts.

These complications lead to a separate, but related XRD project on the binary phases of this study, thus the work presented in this section is still ongoing at the CSIR-NML. In most cases, the pure binary phases would have to be evaluated before the effect of the third element can be considered. It has also been found that the analyses of the corresponding heat-treated samples were easier to interpret than the as-cast samples, as the heat-treated phases are closer to equilibrium conditions. Unfortunately, only the 600°C heat treated samples of the first six alloys were available at the time of this study.

Two new ternary phases were suggested in the EDS analyses. It is considered that the one phase is a high temperature phase that decomposed. The other phase was present in a number of samples. The high temperature phase is preliminary called phase T with a suggested composition of $Ru_{18}Pt_{28}Al_{64}$. Since the phase decomposed, it was not detected by XRD and no prototype could be suggested. The second ternary phase, called phase X here, was matched through a search-and-match procedure to be similar to $IrAl_{2.75}$ and/or $RhAl_{2.63}$. It is proposed that the composition is $Ru_{12}Pt_{15}Al_{73}$, that the phase has a primitive cubic structure and that the lattice parameter is 0.7712 nm.

In some cases the peak overlaps made the phase identification complicated. In sample PAR4, RuAl and $PtAl_2$ were found in the EDS analysis. However, the main reflections in the diffraction patterns for the two phases overlap almost completely, as both phases are cubic, with the $PtAl_2$ lattice parameter about twice the size of the RuAl lattice parameter. By looking at the (311) reflection, which is the second strongest reflection in the $PtAl_2$ pattern and absent in the RuAl pattern, it could be determined with XRD that it was in fact RuAl and not $PtAl_2$ in the sample, thus confirming the EDS results. Similarly, in sample PAR3, the RuAl and $RuAl_2$ patters also overlap. Although the former is cubic and the latter orthorhombic, the identification of the $RuAl_2$ was difficult: it was a minor phase and its major reflections were overlapping with the RuAl phase. Again, the presence of the (311) reflection in the $RuAl_2$ and absence in the RuAl phase was used as a signature in identification. In sample PAR8, the RuAl phase have not been identified in the XRD spectrum, as it is not the major phase and the main reflections overlap with the$RuAl_2$ reflections.

Three crystal structures have been reported for the Pt_3Al phase. The cubic $L1_2$ structure is not included in the ICDD or ICSD, and was also not found in any sample in this study. Sample PAR6 only contained the low temperature DOc structure. Pt_3AL was also found in sample PAR12, where it preferred orientation. It could not be determined which Pt_3Al structure formed in PAR12, as both structures gave a very good R^2 value through the grain refinement procedure. It could also be that both forms are present.

The PtAl phase is not included in the ICDD. The PdAl phase was used as a prototype. However, the PdAl phase has a high temperature and low temperature polymorph. The high temperature polymorph agrees with the β phase that has been suggested in the Al-Pt binary system, and the lattice parameter calculated through the refinement program was in good agreement with the experimental lattice parameter. The presence of the β phase in the samples indicated that the decomposition was not complete, probably the cooling rate was too slow to quench the phase in, but too fast to allow complete decomposition as initially suspected in the EDS analysis.

In some cases where there are many phases in the alloy, all the phases (especially when they were minor or trace phases) could not be identified by XRD. For example, in sample PAR3, the X phase could not be detected in the XRD spectrum. However, from the EDS analysis it is known that there was only a minor amount of X phase in the sample. The X phase was also only found in some regions and not throughout the sample's microstructure.

No phases have yet been confirmed satisfactorily in sample PAR11. The difficulty is probably due to the high percentage of third element in the binary structures.

The lattice parameters are influenced by the presence of the third element in the binary. Since the samples were not at equilibrium, no attempt could be make to calculate the relationship between the lattice parameter and the solid solutions of the third element.

The XRD results are listed in Table 4.18. For each alloy, the phases suggested by EDS analyses are listed. The crystal detail for each phase, as reported in the literature, was compared with the XRD results. The ICDD numbers have been listed only where a phase had been identified by XRD. Only where the lattice parameters have been calculated with the refinement program, have values been listed. Details on specific phases are provided in the footnotes. The XRD analysis of sample PAR 4 is attached in Appendix B.

Although not all the phases could be identified by XRD at this stage and while some minor discrepancies still remain, it was found that EDS and XRD are complementary to each other in this work. Where XRD data existed in the ICDD, the techniques were in good agreement. XRD proves to be a powerful technique to identify the phases in a metal alloy sample. Furthermore, where EDS could only pick up the composition of the phase, and not distinguish between phases with similar compositions, XRD revealed the presence of different prototypes on some phases. In some cases where the high temperature binary phase was thought to have decomposed completely, evidence of the high temperature phases was still found.

Table 4.18. Summary and comparison of the XRD results to EDS results.

Sample PAR	EDS proposed phase	Space Group	Prototype	Reported lattice parameter [nm]			Reference	Prototype used	Prototype ICDD number	Calculated lattice parameter [nm]			R^2	n	Notes
				a	b	c				a	b	c			
1	X							$IrAl_{2.75}$	50-1335	0.7663			0.9991	11	1
	Pt_5Al_{21}	(cI416)		1.923			1964Huc								2
	$RuAl_6$	Cmcm	$MnAl_6$	0.74886	0.6556	0.8961	1965Eds	$RuAl_6$	30-0036						3
	(Al)	Fm-3m		0.4049				(Al)	04-0787	0.4050			0.9998	8	
															4
2	T														
	$PtAl_2$	Fm3m	CaF_2	0.5926			1937Zin	$PtAl_2$	03-1006	0.5929			0.9996	13	1
	X							$IrAl_{2.75}$	50-1335	0.7710			0.9993	15	
3	RuAl	Pm-3m	CsCl	0.295			1966Eds	RuAl	29-1404	0.2998			0.9995	8	
	Ru_2Al_3	I4/mmm	Al_2O_3	0.3079		1.443	1966Eds								5
	T														4
	X														1
	$PtAl_2$	Fm3m	CaF_2	0.5926			1937Zin	$PtAl_2$	03-1006	0.5937			0.9992	8	
	$RuAl_2$	Fddd	Si_2Ti	0.8015	0.4715	0.878	1963Sch	$RuAl_2$	18-0057	0.8028	0.4713	0.8800	0.9993	12	
4	RuAl	Pm-3m	CsCl	0.295			1966Eds	RuAl	29-1404	0.2979			0.9994	7	
	PtAl	P213	FeSi	0.4866			1963Fer	PdAl	34-0564	0.4866			0.9996	20	6
	Pt_2Al_3	P3m1	Ni_2Al_3	0.4208		0.5172	1963Fer	Pd_2Al_3	06-0654	0.4211		0.5167	0.9994	10	7
5	RuAl	Pm-3m	CsCl	0.295			1966Eds	RuAl	29-1404	0.3018			0.9995	4	
	β	Pm-3m	CsCl	0.3125			1978Bah	PdAl	06-0626	0.3057			0.9996	5	8
	PtAl	P213	FeSi	0.4866			1963Fer	PdAl	34-0564	0.4868			0.9995	8	6
	Pt_5Al_3	Pbam	Rh_5Ge_3	0.514	1.07	0.395	1964Huc								9
6	(Ru)	$P6_3/mmc$	Mg	0.27059		0.42819		(Ru)	06-0663	0.2752		0.4340	0.9980	3	
	Pt_3Al							Pt_3Al	48-1815	0.5446		0.7808	0.9995	15	10
	(Pt)	Fm-3m	Cu	0.39231				(Pt)	04-0802						
7	$PtAl_2$	Fm3m	CaF_2	0.5926			1937Zin		03-1006	0.5920			0.9996	9	
	X							$IrAl_{2.75}$	50-1335						1
8	RuAl	Pm-3m	CsCl	0.295			1966Eds								
	$RuAl_2$	Fddd	Si_2Ti	0.8015	0.4715	0.878	1963Sch	$RuAl_2$	18-0057	0.7997	0.4718	0.8786	0.9990	19	
	X							$IrAl_{2.75}$	50-1335	0.7731			0.9993	24	
	$PtAl_2$	Fm3m	CaF_2	0.5926			1937Zin								

Sample PAR	EDS proposed phase	Space Group	Proto-type	Reported lattice parameter [nm]			Reference	Prototype used	Prototype ICDD number	Calculated lattice parameter [nm]			R^2	n	Notes
				a	b	c				a	b	c			
9	RuAl	Pm-3m	CsCl	0.295			1966Eds								
	Pt_2Al_3	P3m1	Ni_2Al_3	0.4208		0.5172	1963Fer	Pd_2Al_3	06-0654	0.4229		0.5153		11	
	$PtAl_2$	Fm3m	CaF_2	0.5926			1937Zin	$PtAl_2$	03-1006	0.5942				8	11
10	(Ru)	$P6_3/mmc$	Mg	0.27059		0.42819		(Ru)	06-0663	0.2711		0.4305	0.9995	7	
	RuAl	Pm-3m	CsCl	0.295			1966Eds								
	β	Pm-3m	CsCl	0.3125			1978Bah								8
	PtAl	P213	FeSi	0.4866			1963Fer								6
	Pt_5Al_3	Pbam	Rh_5Ge_3	0.514	1.07	0.395	1964Huc								
11	RuAl	Pm-3m	CsCl	0.295			1966Eds								
	β	Pm-3m	CsCl	0.3125			1978Bah								8
	PtAl	P213	FeSi	0.4866			1963Fer								6
	Pt_5Al_3	Pbam	Rh_5Ge_3	0.514	1.07	0.395	1964Huc								9
12	(Ru)	$P6_3/mmc$	Mg	0.27059		0.42819		(Ru)	06-0663	0.2689		0.4335	0.9994	5	
	Pt_3Al	P4/mbm I4/mcm	GaPt3(LT)	0.5448 0.3830		0.7814 0.3890		Pt_3Al	48-1815 29-0070						10
13	X							Ir $Al_{2.75}$	50-1335						
	Pt_8Al_{21}	I41/a	1.29595			1.06731	1966Eds								
	Pt_5Al_{21}	(cI416)		1.923			1964Huc								
	(Al)	Fm-3m		0.4049				(Al)	04-0787	0.4045			0.9995	4	
14	$RuAl_2$	Fddd	Si_2Ti	0.8015	0.4715	0.878	1963Sch	$RuAl_2$	18-0057	0.7999	0.4714	0.8784	0.9993		
	X							Ir $Al_{2.75}$	50-1335	0.7712			0.9990		1
	$PtAl_2$	Fm3m	CaF_2	0.5926			1937Zin	$PtAl_2$	03-1006	0.5914			0.9990		
15	β	Pm-3m	CsCl	0.3125			1978Bah								8
	PtAl	P213	FeSi	0.4866			1963Fer	PdAl	34-0564	0.4860			0.9993		6
	Pt_5Al_3	Pbam	Rh_5Ge_3	0.514	1.07	0.395	1964Huc								9
16	$RuAl_2$	Fddd	Si_2Ti	0.8015	0.4715	0.878	1963Sch	$RuAl_2$	18-0057						
	Ru_4Al_{13}	C2/m		1.5862	0.8188	1.1736	1965Eds								12
	X							$IrAl_{2.75}$	50-1335	0.7732			0.9990		
	$PtAl_2$	Fm3m	CaF_2	0.5926			1937Zin	$PtAl_2$	03-1006						

Notes

R^2 – Coefficient of determination (confidence level)

N – number of peaks in diffraction pattern assigned used to identify the phase.

1. Proposed new ternary phase X with composition ~$Ru_{12}Pt_{15}Al_{73}$ with primitive cubic structure and a = 0.7712 nm. Similar to $IrAl_{2.75}$ and $RhAl_{2.63}$. Trace amounts only in PAR3, which was not detected by XRD.
2. Only Pearson symbol reported in the literature.
3. > 10 at. % Pt in $RuAl_6$, structure too distorted in the non-equilibrium condition.
4. High temperature ternary phase T, decomposed at lower temperatures. Estimated composition ~$Ru_{18}Pt_{28}Al_{64}$.
5. Ru_2Al_3 proposed in solidification reactions, decomposed and not observed in EDS or XRD.
6. PtAl not in ICDD. Found that PdAl-μ from Al-Pd system is very similar. PdAl in ICDD: 34-0564 and a=0.4867nm.
7. Pt_2Al_3 not in ICDD. Pd_2Al_3 is very similar. Pd_2Al_3 in ICDD: 06-0654 and a=0.4221 nm and c=0.5155 nm.
8. β not in ICDD, only reported by [1978Bah]. Found that β in Al-Pd system is very similar, also stable at high temperatures only. PdAl-β in ICDD: 06-0626 and a=0.3049 nm.
9. Pt_5Al_3 not in ICDD, could not match up with prototype or any other similar phase and could not identify the pattern. Structure is orthorhombic, so presence of the third element shifts peaks in different directions. Need equilibrium pure binary sample.
10. Different prototypes of Pt_3Al exist. $L1_2$ (cubic, a = 0.3876nm) is high temperature, DOc' (tetragonal, a = 0.3830 nm and c = 0.3890 nm) is stable ~600 –1200 K, DOc (tetragonal, a = 0.5448 nm and c = 0.7814 nm) stable below 600 K. $L1_2$ not in ICDD, DOc' in ICDD 29-0070 and DOc in ICDD 48-1815. In PAR 6, only DOc was found, in PAR12 DOc' and/or DOc were found, could not distinguish as both gave good R^2. No trace of $L1_2$ in the as-cast samples.
11. Not observed in EDS analysis
12. Ru_4Al_{13} in ICDD, but pattern only recorded up to 40° 2 theta. Could not identify.

4.4 Solidification projection.

The phase analyses of the sixteen alloys are summarised in Figure 4.35.

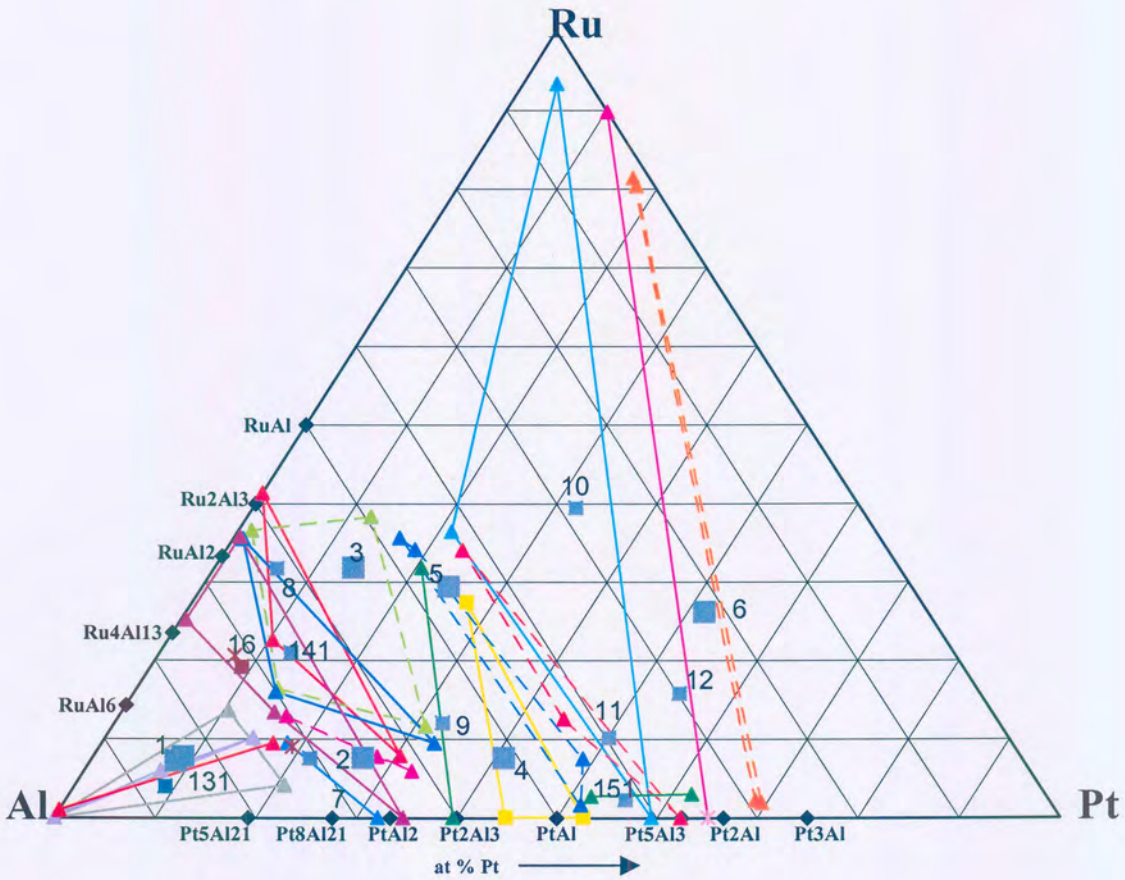

Figure 4.35. Summary of results for ternary Al-Pt-Ru alloys (square = overall composition, triangle = phase composition).

From the analyses of alloys, the following results were obtained:

- The liquidus surface is dominated by RuAl; it occurred to within 10 at. % of the Al-Pt binary.
- (Ru) also has a large liquidus surface. This is an important factor to consider when making alloys that are just outside of the region of the alloys targeted for commercialisation.

- RuAl was found to contain at least 20 at. % platinum

- $PtAl_2$ exhibited up to 11 at. % solubility for ruthenium.

- $RuAl_2$ exhibited up to 10 at. % solubility for platinum.

- Ru_4Al_{13} and $RuAl_6$ were difficult to analyse, since they were found together on a fine scale.

- $RuAl_6$ showed solubility of at least 10 at. % platinum.

- Most of the other phases showed limited solubilities for the ternary element, less than 2 at. %: Ru_4Al_{13}, Pt_2Al_3, Pt_5Al_3, $Pt_5Al_{21}$and PtAl.

- A ternary phase X, with a composition ~$Ru_{12}Pt_{15}Al_{73}$, was found to be present. Initial XRD analysis showed that the X phase probably has a primitive cubic structure and is similar to ~$RhAl_{2.63}$ and ~$IrAl_{2.75}$ .The lattice parameter is 0.7712 nm.

- A high-temperature ternary phase T, with composition of ~$Ru_{18}Pt_{28}Al_{64}$, exists.

- Ru_2Al_3, T and β decomposed through solid-state reactions:
  $Ru_2Al_3 \rightarrow$ ~RuAl + ~$RuAl_2$
  T $\rightarrow$ X + ~$PtAl_2$
  β $\rightarrow$ ~PtAl + Pt_5Al_3

- ~RuAl was involved in a number of subsequent reactions in different alloys:
  peritectic formation of ~PtAl,
  peritectic formation of ~$PtAl_2$
  peritectic formation of β phase of the Al-Pt binary.

- There was good agreement between the experimental EDS and XRD results, despite the lack of phases present in the ICDD. In many cases, the structures of prototypes could be used through a grain refinement process to identify the binary phases.

4.4.1 Liquidus surface projection

The proposed liquidus surface projection is presented in Figure 4.36. The overall compositions of the alloys have been superimposed on the liquidus surface projection in Figure 4.37. The solidification reaction sequence for the Al-Pt-Ru systems, starting at the platinum corner, is summarised in Table 4.16.

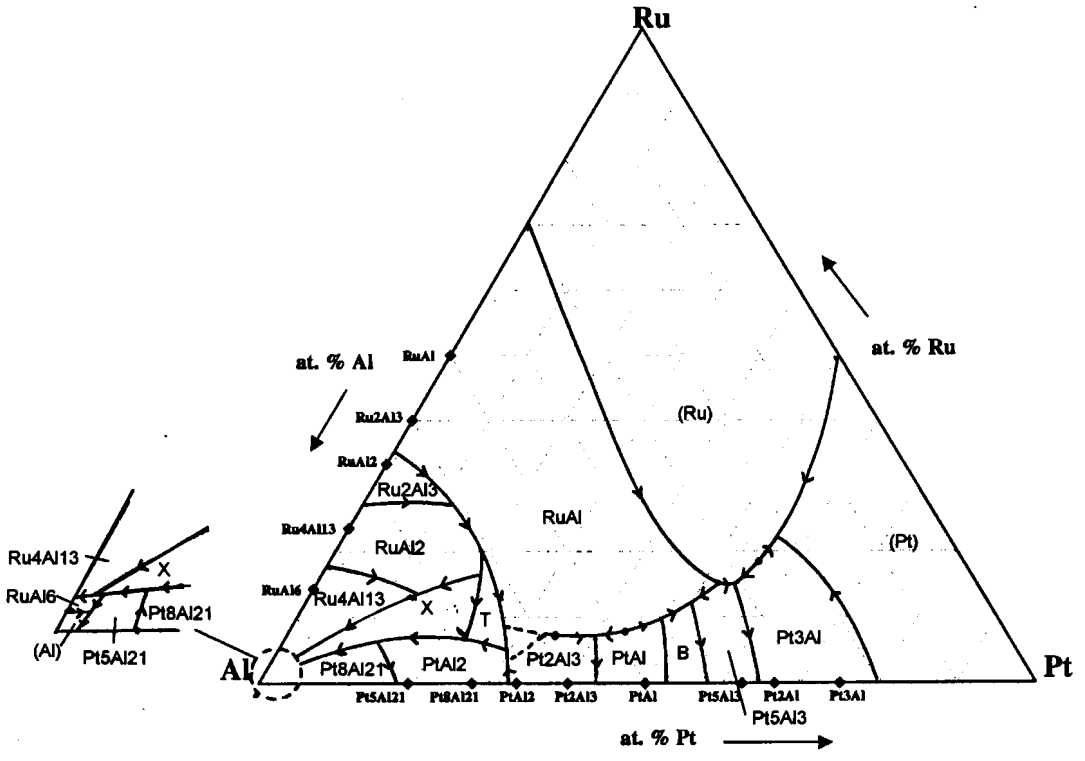

Figure 4.36. Proposed experimental liquidus surface projection.

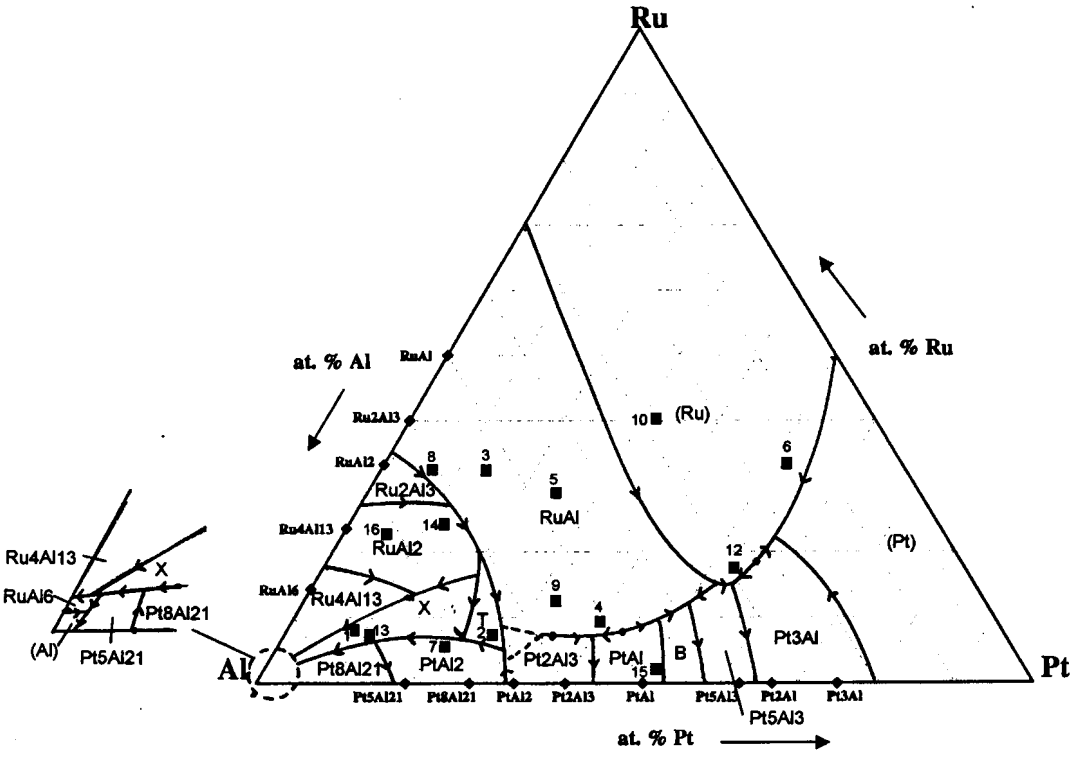

Figure 4.37. Overall alloy compositions on the liquidus surface projection.

The primary phase of each of the alloys indicated on which liquidus surface it lay. The solidification sequence was then used to determine the rest of the liquidus surface. Where there was a reaction between more than one phase and the liquid, it means that the liquidus surfaces of the phases must be adjacent. The liquidus surface projection is consistent with the solidification sequence of the alloys.

Two ternary phases appear on the liquidus surface projection. The ternary phase T is only stable at higher temperatures, as it decomposed on cooling. The ternary phase X is stable to lower temperatures.

4.4.2 Solidification reaction sequence

The solidification reactions are shown in Figure 4.37, and are listed in Table 4.19.

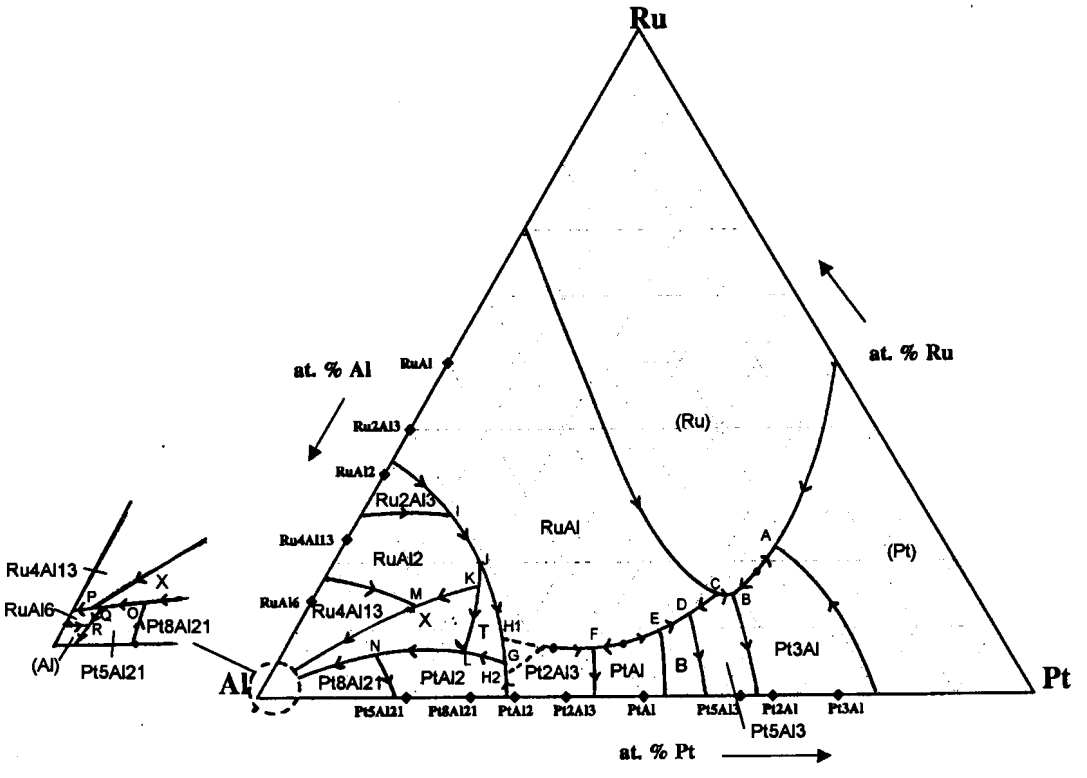

Figure 4.38. Experimental liquidus surface projection for the Al-Pt-Ru system, showing the solidification reactions.

Table 4.19. Solidification reactions for Al-Pt-Ru.

Equation number	Reaction
A	$L \rightarrow (Ru) + (Pt) + \sim Pt_3Al$
B	$L + (Ru) \rightarrow Pt_5Al_3 + \sim Pt_3Al$
C	$L + (Ru) + \sim RuAl \rightarrow \sim Pt_5Al_3$
D	$L + \sim RuAl \rightarrow \beta + \sim Pt_5Al_3$
E *	($\uparrow$) $L + \sim PtAl \rightarrow \sim RuAl + \beta$ ($\downarrow$) $L + \sim PtAl + \sim RuAl \rightarrow \beta$
F	$L + \sim RuAl \rightarrow \sim PtAl + Pt_2Al_3$
G * H1 *	$L + Pt_2Al_3 \rightarrow \sim PtAl_2 + \sim Ru_{18}Pt_{28}Al_{64}$ $L + \sim RuAl \rightarrow \sim Ru_{18}Pt_{28}Al_{64} + Pt_2Al_3$
G * H2 *	$L + \sim RuAl \rightarrow \sim PtAl_2 + \sim Ru_{18}Pt_{28}Al_{64}$ $L + Pt_2Al_3 \rightarrow \sim RuAl + \sim PtAl_2$
I	$L + Ru_2Al_3 \rightarrow \sim RuAl + \sim RuAl_2$
J	$L + \sim RuAl + \sim RuAl_2 \rightarrow \sim Ru_{18}Pt_{28}Al_{64}$
K	$L + \sim Ru_{18}Pt_{28}Al_{64} + \sim RuAl_2 \rightarrow \sim Ru_{12}Pt_{15}Al_{73}$
L	$L + \sim Ru_{18}Pt_{28}Al_{64} \rightarrow \sim Ru_{12}Pt_{15}Al_{73} + \sim PtAl_2$
M	$L + \sim RuAl_2 \rightarrow \sim Ru_{12}Pt_{15}Al_{73} + \sim Ru_4Al_{13}$
N	$L + \sim PtAl_2 + \sim Ru_{12}Pt_{15}Al_{73} \rightarrow \sim Pt_8Al_{21}$
O	$L + \sim Pt_8Al_{21} \rightarrow \sim Ru_{12}Pt_{15}Al_{73} + \sim Pt_5Al_{21}$
Q	$L + \sim Ru_{12}Pt_{15}Al_{73} + \sim Pt_5Al_{21} \rightarrow \sim RuAl_6$
P £	$L + \sim Ru_{12}Pt_{15}Al_{73} \rightarrow \sim Ru_4Al_{13} + \sim RuAl_6$
R	$L + \sim RuAl_6 \rightarrow \sim Pt_5Al_{21} + (Al)$

* Not enough experimental data available to conclude in which direction this reaction proceeds.
£ Exit reaction must be peritectic to be consistent with the Al-Ru binary.
* not enough experimental data are available to determine conclusively which direction this reaction goes.

4.5 Conclusions

Sixteen alloy samples were studied with SEM/EDS and XRD. The results from the two techniques were in good agreement. The solidification sequences and a liquidus surface projection have been proposed.